REACTION MECHANISM DEPENDENCE OF THE POPULATION AND DECAY OF ^{10}HE

By

Han Liu

A DISSERTATION

Submitted to
Michigan State University
in partial fulfillment of the requirements
for the degree of

Physics - Doctor of Philosophy

2019

ABSTRACT

REACTION MECHANISM DEPENDENCE OF THE POPULATION AND DECAY OF ^{10}HE

By

Han Liu

The two-neutron unbound nucleus ^{10}He was studied with a 44 MeV/u ^{11}Li beam and a 47 MeV/u ^{13}B beam. Neutrons were measured in coincidence with ^{8}He fragments, and the two-body and three-body decay energies were reconstructed using invariant mass spectroscopy. Due to low statistics and large decay contributions from the population of ^{9}He, energies of resonant states in ^{10}He could not be extracted from the ^{13}B beam. The ^{11}Li beam data could be described with a correlated background model, implying that the measured spectra are strongly influenced by the initial halo configuration of ^{11}Li. In addition, from comparisons with previous data a target dependence of the data is suggested.

TABLE OF CONTENTS

LIST OF TABLES

LIST OF FIGURES

Chapter 1

Introduction

Nuclear structure and nuclear reactions are two important subfields of modern nuclear physics. While nuclear reactions study the process that changes nuclei from one kind to another, the investigation of nuclear structure is focused on understanding properties of a given nuclear species. One tremendous success in nuclear structure is the Shell Model. Different from its atomic counterpart in which electrons are attracted by the central charge, the nucleonic shell model assumes nucleons feel a mean field caused by all constituent nucleons of a nucleus. With a phenomenological Wood-Saxon potential including spin-orbit terms, the Shell Model predicts states of a large range of isotopes with satisfactory accuracy. Notably, the magic numbers, where atomic nuclei with those numbers of neutrons and protons are more tightly bound than others, are reproduced by Shell Model predictions. Those numbers are 2, 8, 20, 28 and 50 for the light nuclei.

However, as modern rare isotope facilities push nuclear structure studies to the nucleon driplines, challenges have appeared. For example, the breakdown of shell closures [1, 2], the emergence of the islands of inversion [3, 4] and the existence of halo nuclei as weakly-bound systems [5] were observed near the neutron dripline. An island of inversion is a region in the chart of nuclei where the ordering of energy levels of nuclei are different from the Shell Model prediction, and a halo nucleus is an atomic nucleus with extended wave-functions of valence neutrons or protons surrounding the core. These phenomena are enhanced as we move closer

to the dripline. Most extreme cases are expected beyond the neutron dripline, where nuclei are unbound and exist as resonances. These resonances decay by emitting neutrons in an extremely short time, on the order of 10^{-22} s. These nuclides are not only shorter-lived than unstable bound nuclei which have lifetimes usually more than 1 ms, but also significantly shorter-lived than excited bound states, since the lifetime of electromagnetic decays is usually on the order of 10^{-15} s. 10^{-22} s is comparable to the timescale of nucleon motion within a nucleus. With such short lifetimes, questions arise. Can we investigate those unbound nuclei independently from reaction mechanisms? Do these nuclei have sufficient time to "forget" how they were produced? And can we even call those unbound systems nuclei?

As studies of nuclear structure move further away from the driplines, more nuclei with large widths and short lifetimes are expected to be encountered. One such example is ^{10}He, which has an expected lifetime that is so short that it is possible to probe the assumption that the extracted nuclear structure is independent of the nuclear reaction. ^{10}He is two-neutron unbound and decays to the last bound helium isotope, ^{8}He, plus two neutrons. It is nominally a doubly magic nucleus since it consisted of 8 neutrons and 2 protons. The resonance energy of ^{10}He is controversial. However, the measured widths are on the magnitude of MeV, corresponding to a half-life on the order of 10^{-22} s, making ^{10}He an ideal test case for investigating the interplay between nuclear structure and nuclear reactions.

Chapter 2

Background and Motivation

2.1 Previous Measurements

Since ^{10}He is nominally doubly-magic, earlier experimental searches for ^{10}He attempted to find bound ^{10}He fragments [6, 7, 8, 9, 10, 11, 12]. It was not until 1988 that the particle-instability of ^{10}He was widely accepted through the result of a projectile fragmentation experiment with a 30 MeV/u ^{18}O beam [13]. Later on, ^{10}He resonances were reported from eight experiments. In the following subsections, those experiments are discussed in detail, grouped by production method.

2.1.1 ^{11}Li(−p)

Three out of the eight ^{10}He measurements were conducted using one-proton knockout (sudden removal of one proton) reactions, with different beam energies and targets.

The first ^{11}Li(−p) experiment, which was the first observation of a ^{10}He resonance, was performed at RIKEN (Rikagaku Kenkyujo, Wako, Japan) and published in 1994 [14], and the measured spectrum can be seen in Fig. 2.1. In this experiment, a 61 MeV/u (MeV per nucleon kinetic energy) ^{11}Li secondary beam produced from a ^{18}O primary beam impinged on a 390 mg/cm^2 CD_2 target and a 280 mg/cm^2 C target. The four-momenta of neutrons and ^{8}He fragments were measured, and the ^{8}He + n + n invariant mass spectrum was

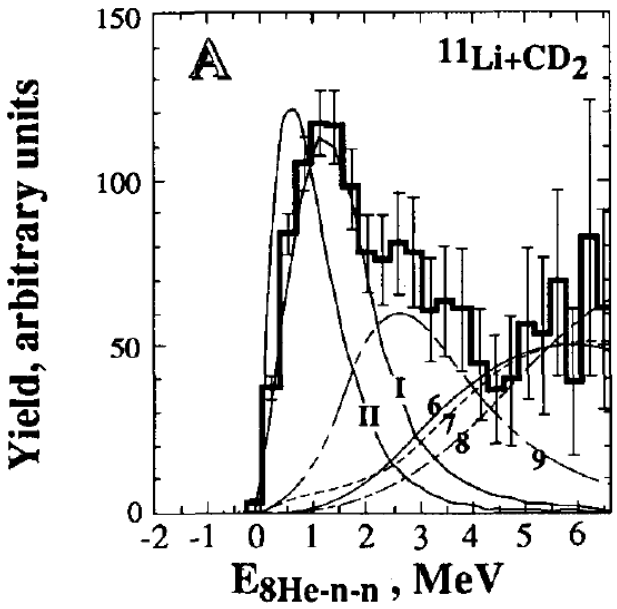

Figure 2.1: First observation of a ^{10}He resonance from Ref. [14]. Line I indicates the best fit. All other lines are other contributions considered which did not explain the data.

reconstructed. Background subtraction was achieved by subtracting scaled data obtained with the C target from the data obtained from the CD_2 target. The corresponding spectrum is shown in Fig. 2.1 which exhibits a strong 1.2 MeV peak. The authors considered line shapes calculated from multi-particle phase space and the ^{11}Li fragmentation process, with or without final state interactions (FSIs). None of these calculations could explain their spectra. Therefore, they concluded that the observed 1.2 MeV peak could be a resonance in ^{10}He. They performed Monte Carlo simulations, and extracted a decay energy for the ^{10}He ground state resonance, a 1.2 ± 0.3 MeV state above the 2n threshold with a width less than 1.2 MeV.

Another ^{11}Li($-$p) experiment was also performed at RIKEN in 1997 [15]. In this experiment, a 83 MeV/u ^{11}Li secondary beam was produced from a ^{15}N primary beam, and a 200 mg/cm^2 CH_2 target was used to populate ^{10}He via the ^{11}Li(p,2p) reaction. The recoil proton and the knocked out proton were detected in coincidence and the separation energy

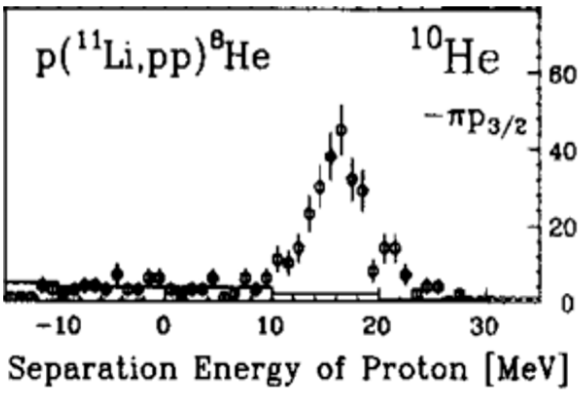

Figure 2.2: Separation energy for p(^{11}Li,2p)^{10}He reactions from Ref. [15]. Solid lines indicate background from C in the CH_2 target.

spectrum of the removed proton was reconstructed from the four-momenta of the incident, the scattered and the knocked-out proton in inverse kinematics (the projectile is heavier than the target nucleus), as shown in Fig. 2.2. The authors deduced a decay energy of ^{10}He of 1.7 $\pm$ 0.3 (stat.) $\pm$ 0.3 (syst.) MeV from the measured separation energy spectrum and the ^{11}Li one-neutron separation energy. The authors indicated that the absolute value of the decay energy is preliminary, and the width was not reported. The authors observed no peak structures in the separation energy spectra in coincidence with ^{6}He or ^{4}He, suggesting that the ^{10}He resonance they observed does not have decay modes to ^{6}He + n + n or ^{4}He + n + n.

The third ^{11}Li(−p) experiment was carried out at GSI (Gesellschaft fur Schwerionenforschung, Darmstadt, Germany). A 280 MeV/u secondary ^{11}Li beam produced from a ^{18}O primary beam was used. The target in this experiment was a liquid hydrogen target with a thickness of 350 mg/cm^2. Neutrons and ^{8}He fragments were measured, and the decay energies of ^{10}He were reconstructed using invariant mass spectroscopy. The results of this experiment were reported in two papers [16, 17]. Instead of fitting the data with simulations, the authors converted the observed decay energy spectra to the absolute decay energy

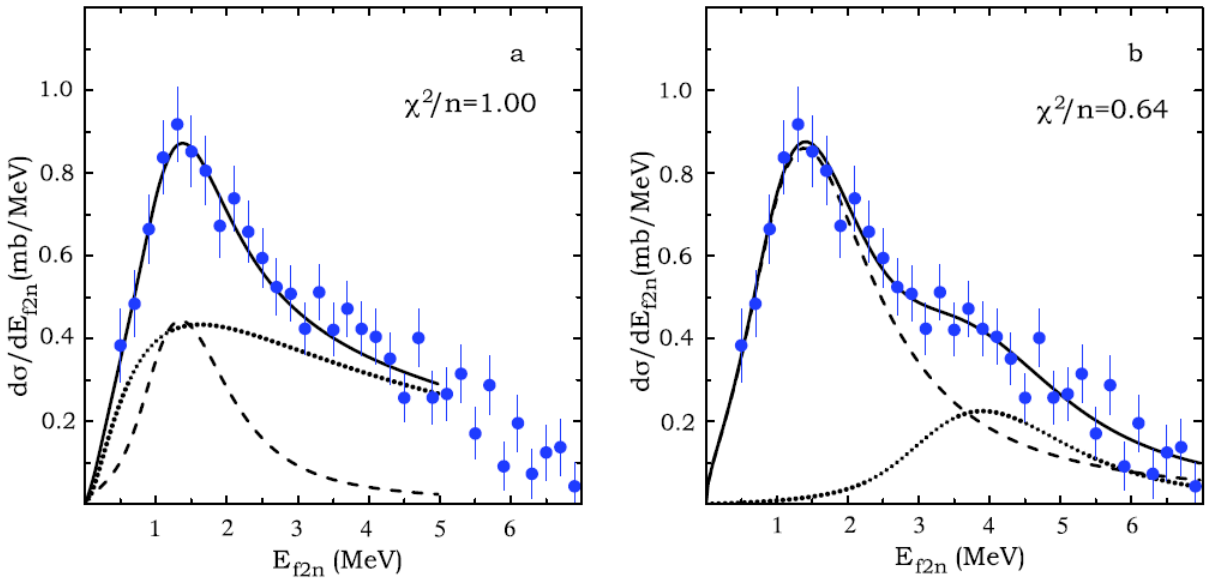

Figure 2.3: Two invariant mass spectra for ^{10}He from Ref. [16]. The left panel shows the 1.42 MeV g.s. plus a correlated background. The right panel shows a 1.54 MeV g.s. plus a 3.99 MeV excited state.

differential cross section and then fit the differential cross section with theoretical distributions. In the first paper [16], they explained the measurement with two possibilities without preferences. Their spectrum could be fit by a 1.42(10) MeV ground state resonance on top of a correlated background [18], which originated from the neutron halo wave-function of the ^{11}Li beam, or with a 1.54(11) MeV ground state plus a 3.99(26) MeV excited state, as shown in Fig. 2.3. In the later paper [17], however, Jacobi coordinates were analyzed in addition to decay energy spectra. The authors concluded that since the correlated background did not fit Jacobi coordinates, only the interpretation involving the a 1.54(11) MeV ground state plus a 3.99(26) MeV excited state was plausible.

2.1.2 ^{10}Be(^{14}C,^{14}O)^{10}He

Shortly after the first ^{10}He observation, the analysis of a double charge-exchange reaction ^{10}Be(^{14}C,^{14}O)^{10}He was reported [19]. This experiment was performed at HMI (Hahn-

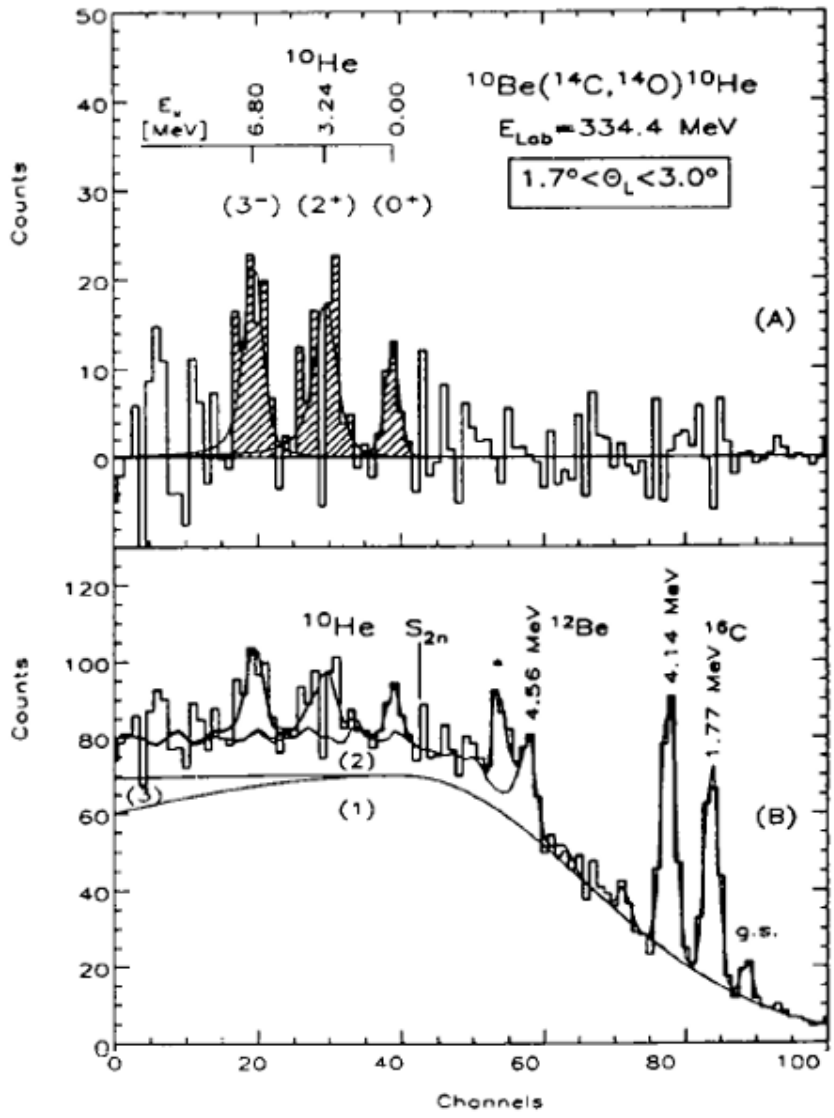

Figure 2.4: ^{10}Be(^{14}C,^{14}O)^{10}He spectra from Ref. [19]. The lower panel shows the spectrum before background subtraction. The scale of the decay energy is shown in the upper-left corner of the upper panel.

Meitner Institut, Berlin, Germany) with a ^{14}C beam with energy of E_{lab} = 334.4 MeV. The target consisted of a 4.9 mg/cm^2 Pt-backing, a 600 μg/cm^2 BeO layer (230 μg/cm^2 Be, with 94% enrichment ^{10}Be) and a 400 μg/cm^2 Au cover. A 600 μg/cm^2 V_2O_5 target and a 500 μg/cm carbon target were also used for background estimation. The spectra before and after background subtraction are shown in Fig. 2.4. A peak at 1.07(7) MeV was identified as a ground state in the missing mass spectrum with 28 counts, with a 80% confidence level. The width of the ground state was reported to be 0.3 MeV. In addition to the ground state, 3.23(20) MeV and 6.80(7) MeV excited states were also reported. A mass excess M.E. = 48.81(7) MeV was deduced from the measured Q-value.

2.1.3 ^{3}H(^{8}He,^{1}H)^{10}He

Two subsequent ^{3}H(^{8}He,^{1}H)^{10}He experiments were performed at JINR (Joint Institute for Nuclear Research, Dubna, Russia) [20, 21] and the missing mass spectra of the two experiments are shown in Fig. 2.5a and Fig. 2.5b, respectively. Gaseous tritium targets were used for transferring two neutrons to the ^{8}He beam, and empty target chambers were used for background estimation. In both experiments, the momenta of the recoil protons were measured in order to derive the missing mass spectra.

In the first experiment [20], a 34 MeV/u ^{11}B primary beam produced a 27.4 MeV/u ^{8}He secondary beam. The gaseous tritium target was operated at a temperature of 28 K. The statistics of this experiment were limited. No events with decay energy lower than 2.5 MeV were observed. 10 events were distributed between 2.5 MeV to 5.5 MeV, and the authors of this experiment identified those events as a resonant state at $\sim$ 3 MeV. They made cross section estimations and claimed that if a ground state below 2.5 MeV exists, they expect 8 counts, and the probability of a non-observation is less than e^{-8}. The authors suggested the

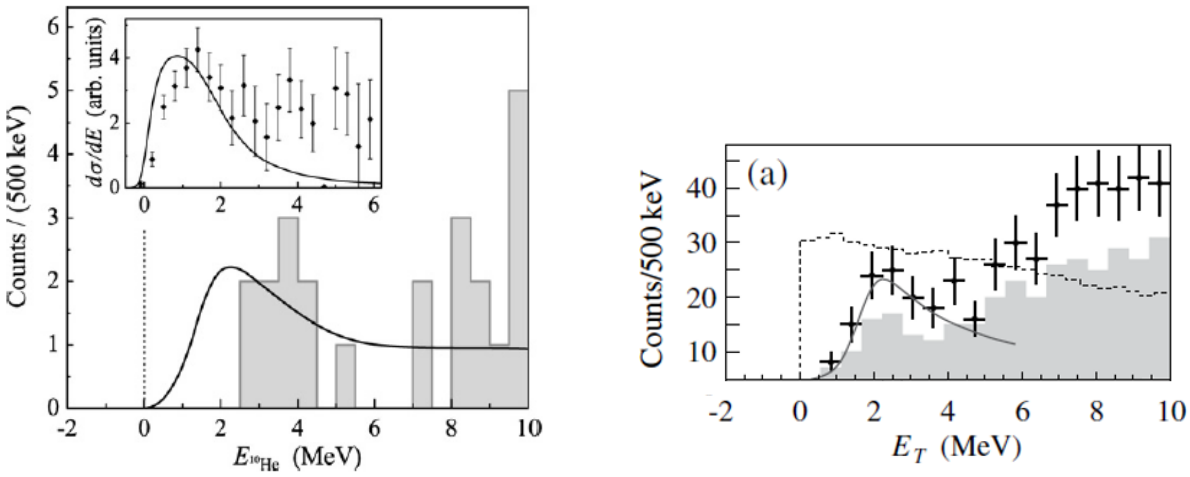

Figure 2.5: (a) ^{3}H(^{8}He,^{1}H)^{10}He spectrum from Ref. [20]. The shade histogram shows data. The solid black line shows the prediction from Ref. [22]. (b) ^{3}H(^{8}He,^{1}H)^{10}He spectrum from Ref. [21]. The crosses shows data with statistical error bars. The shaded histogram shows the missing mass spectra with a correlation gate which is described in Ref. [21].

$\sim$ 3 MeV state to be the ground state of ^{10}He and it is the same state measured by previous ^{11}Li experiments [14, 15] which concluded the ground state is below 1.7 MeV. They argued the extended wave-functions of the halo neutrons in the ^{11}Li beam shifts the peak of the observed decay energy down, according to reference [22]. This effect is discussed in Section 2.2 in detail.

The following refined ^{3}H(^{8}He,^{1}H)^{10}He experiment [21] produced a 21.5 MeV/u ^{8}He secondary beam from a 36 MeV/u ^{11}B primary beam. A tritium target running at a temperature of 26 K was used. Statistics were improved and angular correlations were reconstructed in this experiment. The authors claimed to observe a broad ground state at 2.1 $\pm$ 0.2 MeV with spin assignment 0^{+}, a 1^{-} excited state at a maximum energy between 4 - 6 MeV, and a 2^{+} state above 6 MeV. They argued that their result agreed with previous experiments and the same ^{11}Li initial state effect was used to explain why their new measured state is higher than of the ^{11}Li experiments.

2.1.4 ^{14}Be(−2p2n)

The first ^{10}He experiment performed at NSCL (National Superconducting Cyclotron Laboratory, East Lansing, USA) used a ^{14}Be 2n2p-removal reaction [23]. The experimental setup, data analysis, and simulations of this experiment were similar to the current experiment, which is described in the following chapters in detail. A 59 MeV/u ^{11}Li secondary beam was produced from a 120 MeV/u ^{18}O primary beam, and a 435 mg/cm^2 deuterated carbon target was used as the reaction target. The ^{8}He fragment and neutrons from ^{10}He decays were detected and the invariant mass spectrum of ^{10}He was reconstructed from these decay products. The decay energy spectrum is shown in Fig. 2.6.The authors evaluated an energy for the ground state of 1.60(25) MeV above the ^{8}He + n + n decay threshold with a width of 1.8(4) MeV. This ground state energy agreed with previous ^{11}Li(−p) experiments, although it disagreed with ^{3}H(^{8}He,^{1}H)^{10}He. The authors of this analysis argued the initial state effect cannot explain the discrepancy, because despite the halo structure of ^{14}Be, the dispersive 2p2n-removal reaction should disturb the halo neutrons and eliminate the initial state effect. The authors argued that because the decay energy measured from ^{14}Be(−2p2n) experiment disagreed with the ^{3}H(^{8}He,^{1}H)^{10}He experiments, it disproved the theory of initial state effects in reference [22].

2.1.5 ^{11}Li(^{2}H,^{3}He)^{10}He

The most recent ^{10}He measurement was carried out at RIKEN with the ^{11}Li(^{2}H,^{3}He)^{10}He reaction [24] and the measured missing mass spectrum is shown in Fig. 2.7. A 50 MeV/u ^{11}Li beam was produced from a 100 MeV/u ^{18}O beam. A 1.9 mg/cm^2 CD_2 target was used for the proposed reaction and a 1 mg/cm^2 natural carbon target was used for background

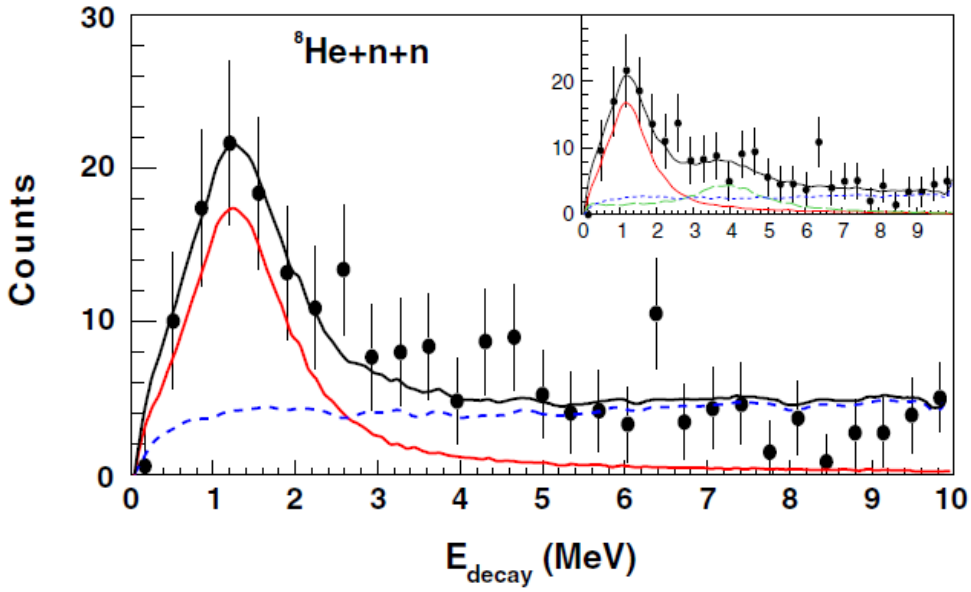

Figure 2.6: Invariant mass spectrum of ^{10}He from Ref. [23]. The solid circles represent experimental data. The solid red line represents a simulated 1.6 MeV state. The blue dotted line represents simulated non-resonant background. The solid black line shows the sum of the two simulations.

subtraction. ^{3}He recoils were measured to reconstruct the missing mass spectra of ^{10}He. ^{8}He, ^{6}He, and ^{4}He from ^{10}He decays were detected to determine the final states of ^{10}He decays. The measured spectra were fit by Breit-Wigner distributions, convoluted with Gaussian resolution functions. The authors of the article concluded the ground state of ^{10}He to be 1.4(3) MeV with a 1.4(2) MeV width. One excited state was reported to be at 6.3(7) MeV with a 3.2 MeV width. The authors also determined the ^{6}He + 4n decay channel to be stronger than the ^{8}He + n + n channel. Decays to ^{4}He + 6n were not observed.

2.2 Theoretical Efforts

There is also a debate about ^{10}He among theorists. After it was generally accepted that ^{10}He is unbound, theoretical works regarding the structure of ^{10}He were focused on calculating

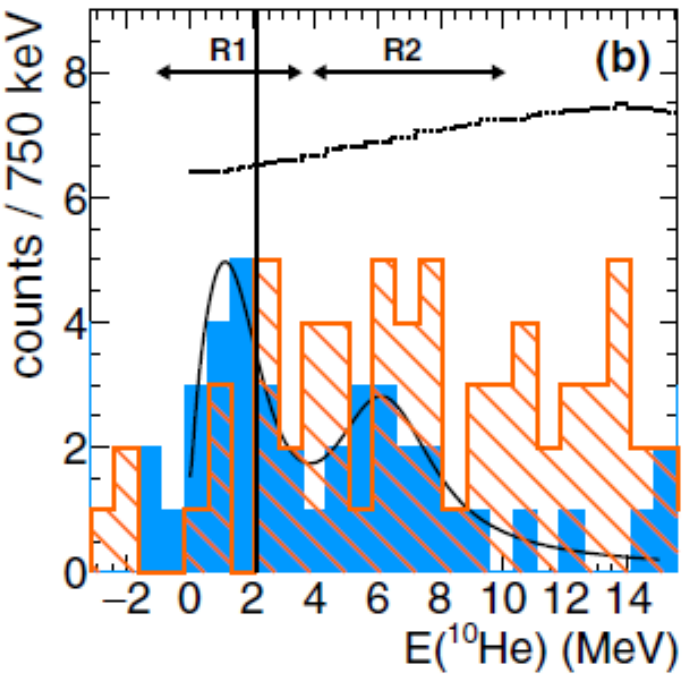

Figure 2.7: Missing mass spectra of ^{10}He from Ref. [24]. The solid blue histogram represents the missing mass spectrum in coincidence with ^{8}He fragments. The dashed red histogram represents the missing mass spectrum in coincidence with ^{6}He fragments

resonances in ^{10}He. Korsheninnikov et al. predicted with hyperspherical calculations that ^{10}He exists as a narrow three-body resonance with a resonance energy less than 1 MeV, and a width of 150 - 300 keV [25], before Korsheninnikov et al. reported the first observation of ^{10}He [14]. Shortly after the discovery of ^{10}He, Kato et al. calculated ^{10}He with three-body models using basis functions of the cluster orbital shell model (COSM) and the complex scaling method (CSM) [26]. They concluded that the ^{10}He ground state is at 2.14 MeV with a width of 1.63 MeV and an excited state at 5 MeV. Aoyama and Kato, et al. reported with the complex scaling method that the ^{10}He ground state resonance is at 1.8 MeV with a 1.4 MeV width and the two valence neutrons were considered to occupy the $p_{1/2}$ orbital [27]. Later, however, Aoyama, Kato, et al. reported with both the complex scaling method and the analytical continuation in the coupling constant (ACCC) method that the earlier calculated $[p_{1/2}p_{1/2}]_{0+}$ is not the ground state of ^{10}He, but that the ground state has a $[s_{1/2}s_{1/2}]_{0+}$ configuration near 0 MeV, which had not been observed so far [28]. Aoyama repeated similar ACCC calculations and reiterated that the ground state of ^{10}He is a three-body s-wave resonance ($[s_{1/2}s_{1/2}]_{0+}$) with a decay energy smaller than 0.05 MeV, and that this state had not been observed [29, 30, 31]. Kamada et al, calculated the energy of ground 0^+ state at 0.803 MeV with a core-excitation three-body model [32]. The most recent ^{10}He calculation reported by Fossez et al. was the only structure calculation using a many-body model [33]. The authors predicted a narrow double-halo ^{10}He ground state very close to threshold, and the predicted configuration was almost pure s-wave.

Rather than predicting states in ^{10}He, theoretical efforts were also specifically made to reconcile the conflicting results of ^{10}He experimental results, i.e. the discrepancy in the g.s. energy between the ^{3}H(^{8}He,^{1}H)^{10}He experiments with other measurements. Fortune suggested that the "ground state" measured so far might be two overlapping 0^+ states [34].

He argued that the relative population of the two 0^+ states changes with the reaction types so different experiments observed different energies of the "ground state". He calculated the relative ratio between the two states using simple reaction models [35]. Fortune then extracted that the *p*-shell 0^+ ground state is lower than 1.4 MeV and the *sd*-shell 0^+ excited state is higher than 2.1 MeV [36]. In a later refined work, Fortune indicated that the 1.07(7) MeV resonance measured by the experiment described in Section 2.1.2 is the ground state, and the first excited state is in the region between 2.1 to 3.1 MeV [37].

On the other hand, Grigorenko and Zhukov argued the states observed in the ^{3}H(^{8}He,^{1}H)^{10}He transfer experiment might be the same states measured in ^{11}Li knockout experiment, if the reaction dynamics were considered [22]. Their calculation suggests the extended wave-functions of the two halo neutrons in ^{11}Li beam "shifts" the observed decay energies down. The authors also indicated that for their explanation be correct, ^{9}He cannot have a virtual state, and they were unable to make ^{9}He and ^{10}He data consistent with their model. Grigorenko and Zhukov also predicted an *s*-state below 0.3 MeV according to the same theory [22]. Fortune commented that such an *s*-state would locate the mixed ground state below the two-neutron separation threshold [35, 34]. As discussed earlier in section 2.1.4, the result of the ^{14}Be($-$2p2n) experiment did not favor the theory proposed by Grigorenko and Zhukov.

A later theoretical prediction [39] indicated the result from the ^{14}Be($-$2p2n) experiment might still agree with ^{3}H(^{8}He,^{1}H)^{10}He experiments if the 2p2n-removal reaction were considered as an α removal. If that assumption were true, a similar initial state effect existed, therefore the "shifted" down ^{14}Be($-\alpha$) decay energy still agrees with the ^{3}H(^{8}He,^{1}H)^{10}He transfer experiments. In Ref. [39], Sharov et al. also extended the calculations performed by Grigorenko and Zhukov [22], and claimed that the ground state of ^{10}He observed from a ^{11}Li beam might be a superposition of 1^-, 0^+ and 2^+ excitations, and the 1^- excita-

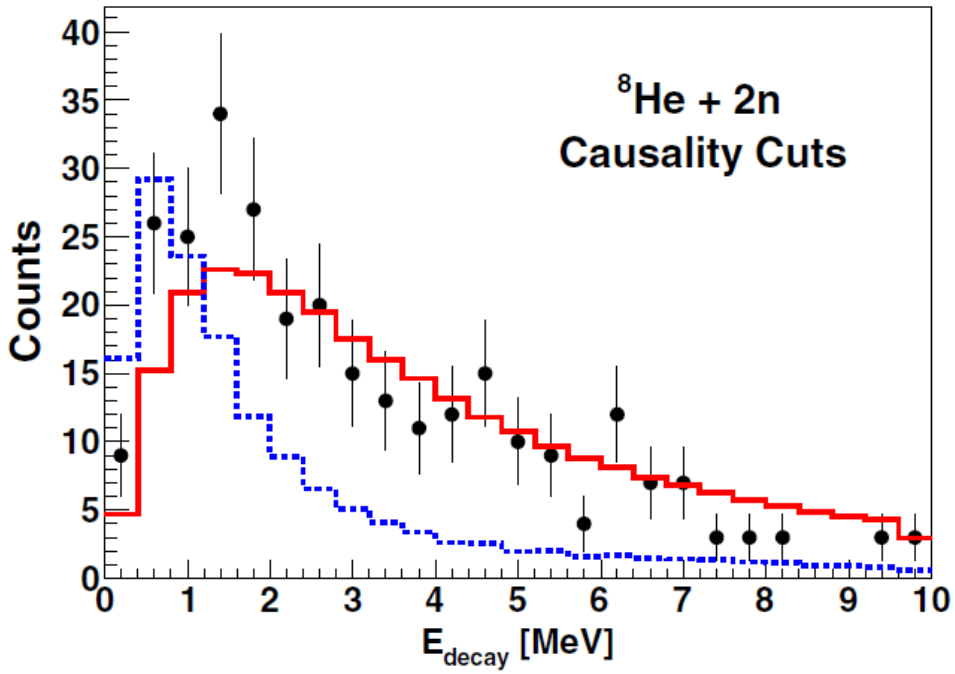

Figure 2.8: Invariant mass spectrum of ^{10}He from Ref. [38]. The solid circles represent data from ^{14}Be($-$2p2n). The solid red line represents the calculation from [39]. The blue dotted line represents the calculations from from [39] folded with the experimental response function. The causality cuts applied to this spectrum are discussed in Section 5.3.1.

tion is actually the lowest excitation. However, Sharov et al. used the three-cluster model and potential developed in Ref. [22], and they required the scattering length of ^{9}He to be positive, which is not supported by experiments. The authors of the ^{14}Be($-$2p2n) paper responded in Ref. [38]. The response pointed out that the authors of Ref. [39] compared pure theoretical line shapes with experimental spectra which were folded with the experimental response function, as shown in Fig. 2.8. The authors of the follow-up paper showed that after the experimental conditions were considered, the ^{14}Be($-\alpha$) calculation did not fit data, and concluded no evidence for initial state effects were found.

2.3 Summary of Previous Works

Previous studies of ^{10}He are conflicted in both experiment and theory. The effect of extended wave-functions of the halo neutrons in incoming beams were proposed to reconcile conflicting experimental measurements. Although the quantitative conclusions have been disproven by multiple theoretical and experimental analyses, the initial state effect itself remains intriguing. Measurements with other initial states are necessary to expand the understanding of ^{10}He and the initial state effect. Therefore, the current experiment was proposed to study ^{10}He using a compact non-halo ^{13}B beam, and a halo ^{11}Li beam.

Table 2.1: Summary of model predictions for ^{10}He.

Model Type	Assumption(s)	Main Prediction(s)	Ref.
Three-body	Hyperspherical harmonic bases	$E_{\text{g.s.}}$ <1 MeV, 150 keV<$\Gamma_{\text{g.s}}$<300 keV	[25]
Three-body	COSM bases CSM method	$E_{\text{g.s.}} = 2.14$ MeV, $\Gamma_{\text{g.s}} = 1.63$ MeV; $E_{\text{exc.}} \sim 5$ MeV	[26]
Three-body	COSM bases CSM method	$E_{\text{g.s.}} = 1.8$ MeV, $\Gamma_{\text{g.s}} = 1.4$ MeV, p-wave	[27]
Three-body	COSM bases ACCC method	$E_{\text{g.s.}} \sim 0$ MeV, s-wave $E_{\text{exc.}} = 1.68$ MeV, p-wave	[29]
Three-body	COSM bases ACCC method	$E_{\text{g.s.}} \sim 0$ MeV, s-wave	[28] [30]
Three-body	COSM bases ACCC method	$E_{\text{g.s.}} \sim 0.05$ MeV, $\Gamma_{\text{g.s}} = 0.21$ MeV, s-wave	[31]
Three-body	Core-excitation, AGS bases	$E_{\text{g.s.}} = 0.803$ MeV, $\Gamma_{\text{g.s}} = 0.67$ MeV, 0^+; $E_{\text{exc.}} = 1.25$ MeV, $\Gamma_{\text{exc.}} = 0.21$ MeV, 1^-	[32]
Three-body Dynamical	^{10}He source wave-functions from ^{11}Li; sudden removal	$E_{\text{g.s.}} \geq 2$ MeV, p-wave; the observed peak shifted to lower energies with halo sources; three-body virtual s-state less than 0 MeV	[22]
Three-body Dynamical	^{10}He source wave-functions from ^{11}Li; sudden removal	2.0 MeV $< E_{\text{g.s.}} <$ 2.3 MeV, p-wave; the observed peak shifted to lower energies with halo sources;	[39]
Many-body	α-core, single particle Berggren bases	$E_{\text{g.s.}} \sim 0$ MeV, s-wave, "double halo" structure	[33]

Chapter 3

Theoretical Background

This chapter will discuss the decay models and line shapes used in the simulations. The full derivation is beyond the scope of this chapter. Therefore, only the framework will be provided. For more details, the readers are referred to the original works.

3.1 Decay Models

Given a decay energy, the decay model for two-body decays is straightforward since kinematics are determined by energy and momentum conservation. The two decay products are distributed uniformly in their center-of-mass frame.

Three-body decays or n-body decays (n>3), however, cannot be easily determined by the conservation laws because there are additional degrees of freedom in the final state. Decay models are needed to decide the angles of the decay products or the energy partition among different two-body pairs. For example, in the phase space decay model decay products uniformly fill the phase space in the center-of-momentum frame. In this model, the kinematics are governed by the n-body phase integral, defined as [40]

$$R_n = \int \delta^4(P_0 - \sum_{i=1}^{n} P_i) \prod_{j=1}^{n} \delta(P_j^2 - m_j^2) d^4 P_j \tag{3.1}$$

where P_0 is the 4-momentum of the unbound nucleus, P_i and P_j are the 4-momenta of the

decay products, m_i and m_j are the masses of the decay products, and the statistical factor, $\delta(P_j^2 - m_j^2)d^4P_j$, in the spherical coordinates is written as

$$\delta(P_j^2 - m_j^2)d^4P_j = \frac{\vec{p_i}}{E_i} d|\vec{p_i}| d\cos(\theta_i) d\phi_i, \tag{3.2}$$

where $\vec{p_i}$ is the three momentum. Then, distributions of any kinematic parameters, such as momenta or angles, are given by

$$\sigma(\alpha) = \frac{dR_n}{d\alpha}. \tag{3.3}$$

The full description of the phase space model is given in Ref. [40].

3.2 Decay Energy Line Shapes

3.2.1 Breit-Wigner Line Shape

When the final state interaction is not influenced by the reaction mechanism, the process of a 1-neutron decay can be treated like a neutron scattering off the residual fragment. For this problem, R-matrix phenomenology can be used to derive Breit-Wigner distributions [41] which are widely used for the description of resonant states. This section provides a brief summary of the derivation given in Thompson and Nunes [42]. More details about R-matirx theory can also be found in the work of Lane and Thomas [43]. For 2-neutron decays, such as ^{10}He, the two neutrons can be thought of as coupling to the same orbital. Then a Breit-Wigner line shape can be used to describe the decay of ^{10}He.

The decay of a resonance involves entrance and exit channels. Therefore, multi-channel

R matrices are considered and they can be written as [42, p. 296]

$$\mathbf{R}_{\alpha'\alpha}(E) = \sum_{p=1}^{P} \frac{\gamma_{p\alpha}\gamma_{p\alpha'}}{e_p - E} \tag{3.4}$$

where α' and α represent the entrance and the exit channels, respectively, e_p is a pole in the $\mathbf{R}$ matrix, γ is a reduced width, and E is essentially the decay energy. Then, the scattering $\mathbf{S}$ matrix can be written in terms of the $\mathbf{R}$ matrix:

$$\mathbf{S} = \left(\mathbf{t}^{1/2}\mathbf{H}^{+}\right) \frac{1 - a\mathbf{R}\left(\mathbf{H}^{-\prime}/\mathbf{H}^{-} - \beta\right)}{1 - a\mathbf{R}\left(\mathbf{H}^{+\prime}/\mathbf{H}^{+} - \beta\right)} \tag{3.5}$$

where $\mathbf{H}^{\pm}$ has only diagonal elements $H_{\alpha}^{\pm} = G_{\alpha} \pm iF_{\alpha}$, where G_{α} and F_{α} are Coulomb functions [42, p. 61]. The $\mathbf{t}$ matrix also has non-zero elements on the diagonal as $t_{\alpha} \equiv \hbar^2/2\mu_{\alpha}$, where μ_{α} is the reduced mass. Here β is the logarithmic derivative at an arbitrary radius a where the nuclear interaction is negligible. A 'logarithmic' $\mathbf{L}$ matrix can be defined as [42, p. 306]

$$\mathbf{L} = \mathbf{H}^{+\prime}/\mathbf{H}^{+} - \beta = \frac{1}{a}(S + iP - a\beta) \tag{3.6}$$

where the penetrability P and shift function S are diagonal matrices and their matrix elements are

$$P_{\alpha} = \frac{k_{\alpha}a}{F_{\alpha}^2 + G_{\alpha}^2}, \tag{3.7}$$

$$S_{\alpha} = \left(\dot{F}_{\alpha}F_{\alpha} + \dot{G}_{\alpha}G_{\alpha}\right) P_{\alpha}. \tag{3.8}$$

Here dots represent derivatives with respect to $\rho = kR$, where k is the quantum mechanical

wave number and R is the radial coordinate. Then the $\mathbf{S}$ matrix can be written as

$$\mathbf{S} = \Omega \frac{1}{\sqrt{\mathbf{t}\mathbf{H}^{-}\mathbf{H}^{+}}} \frac{1 - a\mathbf{R}\mathbf{L}^{*}}{1 - a\mathbf{R}\mathbf{L}} \sqrt{\mathbf{t}\mathbf{H}^{-}\mathbf{H}^{+}}\Omega, \tag{3.9}$$

where Ω is defined as a diagonal matrix with elements $\Omega_\alpha = e^{i\phi\alpha}$, with Ω_α a hard-sphere phase shift.

The transformation $\mathbf{v}^{1/2}\mathbf{S}\mathbf{v}^{-1/2}$ is used to construct a symmetric matrix $\widetilde{\mathbf{S}} \equiv \mathbf{v}^{1/2}\mathbf{S}\mathbf{v}^{-1/2}$,

$$\widetilde{\mathbf{S}} = \Omega \left[1 + 2iP^{1/2}(1 - a\mathbf{R}\mathbf{L})^{-1}\mathbf{R}P^{1/2}\right]\Omega. \tag{3.10}$$

Suppose there are two channels and one pole. Then, $\mathbf{S}$ simplifies to:

$$\tilde{\mathbf{S}}_{12} = e^{i\phi 1}\left[\frac{2iP_\alpha^{1/2}\gamma_\alpha\gamma_{\alpha'}P_{\alpha'}^{1/2}}{e_p - E - \gamma_1^2\left(S_1 - a\beta\right) - i\gamma_1^2 P_1 - \gamma_2^2\left(S_2 - a\beta\right) - i\gamma_2^2 P_2}\right]e^{i\phi 2}. \tag{3.11}$$

To organize Equation 3.11, the formal width Γ_α, the energy shift Δ_a, the total energy shift Δ_T, and the total formal width Γ_T are defined as

$$\begin{aligned}
\Gamma_\alpha &= 2\gamma_\alpha^2 P_\alpha \\
\Delta_\alpha &= -\gamma_\alpha^2(S_\alpha - a\beta) \\
\Delta_T &= \sum_\alpha \Delta_\alpha = -\gamma_1^2 S_1^0 - \gamma_2^2 S_2^0 \\
\Gamma_T &= \sum_\alpha = 2\gamma_1^2 P_1 + 2\gamma_2^2 P_2,
\end{aligned}$$

where $a\beta$ can be set to any constant. It is suggested in Ref. [42, p. 299] to set $a\beta$ so $S_\alpha - a\beta = 0$ at the pole, known as the natural boundary condition. Then, the cross section

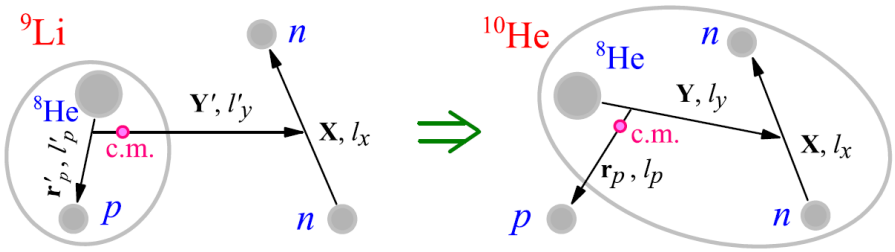

Figure 3.1: Coordinate schemes for the sudden proton-removal calculations from Ref. [39].

is

$$\begin{aligned}\sigma_{12} &\propto \left|\widetilde{\mathbf{S}}_{\alpha\alpha'}\right|^2 \\ &= \frac{\Gamma_2}{\left(E - e_p + \Delta_T\right)^2 + \Gamma_T^2/4}.\end{aligned} \tag{3.12}$$

Since decay through the entrance channel is less likely, $\Gamma_2 >> \Gamma_1$, approximations can be made such as $\Gamma_T \sim \Gamma_2$ and $\Delta_T \sim \Delta_2$. Then, with the natural boundary condition, the line shape for the neutron decay is:

$$\sigma_l\left(E; e_p, \Gamma_0\right) \propto \frac{\Gamma_l\left(E; e_p; \Gamma_0\right)}{\left[e_p - E + \Delta_l\left(E; e_p, \Gamma_0\right)\right]^2 + \frac{1}{4}\left[\Gamma_l\left(E; e_p, \Gamma_0\right)\right]^2} \tag{3.13}$$

where

$$\Gamma_0 = 2\gamma^2 P_l\left(e_p\right). \tag{3.14}$$

3.2.2 Three-Body Dynamical Model

Predictions including reaction dynamics from Refs. [22, 39] were used as the line shapes for the ^{10}He three-body decay energy where the state of the daughter nuclei are affected by their halo (^{11}Li) parents. These predictions are based on the sudden removal of a proton from ^{11}Li, and an outline of the original works is provided below.

The model starts by constructing the ^{11}Li cluster wave-function in the form

$$\Psi^{J_i M_i}_{^{11}\mathrm{Li}}\left(\mathbf{X},\mathbf{Y}',\mathbf{r}'_p\right) = \left[\Psi^{(3b)}_{^{11}\mathrm{Li}}\left(\mathbf{X},\mathbf{Y}'\right)\bigotimes\Psi_{^{9}\mathrm{Li}}\left(\mathbf{r}'_p\right)\right]_{J_i M_i}, \tag{3.15}$$

where the coordinates are defined in Fig. 3.1, $\Psi^{(3b)}_{^{11}\mathrm{Li}}\left(\mathbf{X},\mathbf{Y}'\right)$ is the three-body cluster wave-function of ^{11}Li, and $\Psi_{^{9}\mathrm{Li}}\left(\mathbf{r}'_p\right)$ is the ^{8}Li-p single particle wave-function. The readers are referred to Refs. [22, 39] for more details about how this ^{11}Li cluster wave-function was numerically constructed.

The reaction populating ^{10}He is modeled as the sudden removal of a proton from the ^{9}Li core and a momentum transfer to the remaining ^{8}He cluster. To describe that process, a Raynal-Revai transformation [44] is performed taking $\{\mathbf{Y}',\mathbf{r}'_p\}$ to $\{\mathbf{Y},\mathbf{r}_p\}$, which connects the proton coordinate. Then, the ^{10}He source wave-function is obtained by applying the annihilation operator

$$\Phi_{\mathrm{q}}(\mathbf{X},\mathbf{Y}) = \int d^3\mathbf{r}_p e^{i\mathbf{q}\mathbf{r}_p}\Psi_{^{11}\mathrm{Li}}\left(\mathbf{X},\mathbf{Y},\mathbf{r}_p\right), \tag{3.16}$$

where for different J^π the source wave-functions are given by the angular momentum decomposition

$$\begin{aligned}\Phi^{JM}_{q,\gamma,l_p}(X,Y) = &\int d\Omega_x d\Omega_y d\Omega_q \Phi_{\mathrm{q}}(\mathbf{X},\mathbf{Y}) \\ &\times\left[\left[\left[Y_{l_x}(\hat{X})\otimes Y_{l_y}(\hat{Y})\right]_L\otimes\chi_S\right]_J\otimes Y_{l_p}(\hat{q})\right]_{JM},\end{aligned} \tag{3.17}$$

where γ is a multi-index ($\gamma=\{LSl_xl_y\}$) that defines the complete set of angular momentum quantum numbers.

The ^{10}He source wave-function is used for solving the inhomogeneous Schrodinger equa-

tion

$$\left(\hat{H}_3 - E_{\rm decay}\right) \Psi^{JM(+)}_{E_{\rm decay}}(X,Y) = \Phi^{JM}_q(X,Y), \tag{3.18}$$

where $E_{\rm decay}$ is the decay energy and $\Psi^{JM(+)}_{E_{\rm decay}}(X,Y)$ is the outgoing ^{10}He wave-function. Then, the decay energy line shape predicted by this model is proportional to the flux with the outgoing asymptotic

$$\frac{d\sigma}{dE_{\rm decay}} \sim j\left(E_{\rm decay}\right) = \frac{1}{M}\,{\rm Im}\int d\Omega_5 \Psi^{(+)\dagger}_{E_T} \rho^{5/2} \frac{d}{d\rho} \rho^{5/2}\, \Psi^{(+)}_{E_T}\Big|_{\rho_{\rm max}} \tag{3.19}$$

3.2.3 Correlated Background

In another model, in which ^{10}He is even more influenced by the incoming halo beams, the decay is described as a correlated background [18, 45]. In this model, the ^{10}He system is the remnant of the ^{11}Li halo neutrons without any final state interactions, and mathematically the decay energy distributions are the Fourier transformations of the wave-function of the ^{11}Li halo neutrons. The correlated background was originally developed to describe the break up of halo beams. Then the use was extended to unbound nuclei with the assumption that the center-of-mass of the fragment in the unbound three-body system coincides with the center-of-mass of the core in the halo beam. This section summarizes the main results of the correlated background based on the original work of Forssen et al. [18]. The readers are also referred to the appendix of Ref. [45] for an advanced treatment of the function $\chi^{l_x l_y}_{KL}(\rho)$ which is discussed below.

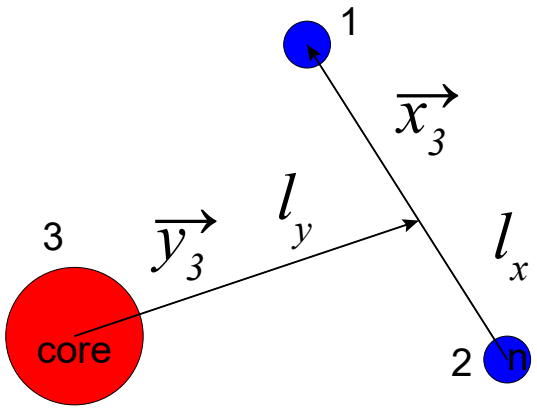

Figure 3.2: Coordinate scheme for one of the translation invariant Jacobi coordinates. Labels $\vec{y_3}$, l_y, $\vec{x_3}$, l_x are corresponding to $\mathbf{Y}'$, l'_y, $\mathbf{X}$, l_x in Fig. 3.1, respectively.

Translation invariant Jacobi coordinates are defined first as

$$\begin{aligned} \vec{x}_l &= \sqrt{A_{ij}}\,(\vec{r}_i - \vec{r}_j) \\ \vec{y}_l &= \sqrt{A_{(ij)l}}\left(\frac{A_i\vec{r}_i + A_j\vec{r}_j}{A_i + A_j} - \vec{r}_l\right), \end{aligned} \tag{3.20}$$

where $l \in (1,2,3)$, $\vec{r}_i$ is the Cartesian coordinates of the i-th particle, A_i is the mass number of the i-th particle ,A_{ij} is the reduced mass number of the particle pair ij, and $A_{(ij)l} = (A_i + A_j)A_l/\left(A_i + A_j + A_l\right)$. One set of the Jacobi coordinates is shown in Fig. 3.2. Note this particular set is similar to coordinates used in the previous subsection.

A three-body wave-function can be expanded in hyperspherical harmonics [46] without spin and isospin

$$\Psi\left(\vec{x}_l, \vec{y}_l\right) = \rho^{-5/2} \sum_{KLl_xl_y} \chi_{KL}^{l_xl_y}(\rho)\Gamma_{KL}^{l_xl_y}\left(\Omega_5^\rho\right), \tag{3.21}$$

where K is the extra quantum number hypermomentum defined as $K = l_x + l_y + 2\mu \quad (\mu = 0,1,2,\ldots)$, ρ is the hyperradius defined as $\rho = (x_l^2 + y_l^2)^{(1/2)}$, $\Gamma_{KL}^{l_xl_y}\left(\Omega_5^\rho\right)$ is the hyperspherical harmonics basis, $\left(\Omega_5^\rho\right) \equiv \left\{\theta_\rho, \hat{x}_l, \hat{y}_l\right\}$ represents the five angles parameterizing a hypersphere

with a hyperangle $\theta_\rho \equiv \arctan(x_l/y_l)$ and angular coordinates $\{\hat{x}_l, \hat{y}_l\}$ corresponding to $\vec{x}_l$ and $\vec{y}$, and the asymptotics of $\chi_{KL}^{l_x l_y}(\rho)$ is

$$\chi_{KL}^{l_x l_y}(\rho) \sim \exp(-\kappa_0 \rho). \tag{3.22}$$

$\Psi(\vec{x}_l, \vec{y}_l)$ can be expressed in momentum representation as

$$\Psi(\vec{q}_l, \vec{p}_l) = \frac{1}{(2\pi)^3} \int \Psi(\vec{x}_l, \vec{y}_l) \exp\left[\mathrm{i}\left(\vec{q}_l \cdot \vec{x}_l + \vec{p}_l \cdot \vec{y}_l\right)\right] \mathrm{d}\vec{x}_l \mathrm{d}\vec{y}_l \tag{3.23}$$

where Jacobi momenta are defined as

$$\begin{aligned} \vec{q}_l &= \sqrt{A_{ij}} \left(\frac{\vec{k}_i}{A_i} - \frac{\vec{k}_j}{A_j} \right) \\ \vec{p}_l &= \sqrt{A_{(ij)l}} \left(\frac{\vec{k}_i + \vec{k}_j}{A_i + A_j} - \frac{\vec{k}_l}{A_l} \right), \end{aligned} \tag{3.24}$$

where k_i is the momentum of the i-th particle. A variable $\kappa^2 = \vec{q}_l^{\,2} + \vec{p}_l^{\,2}$ can be defined so that

$$E = \frac{\hbar^2}{2m} \left(\frac{\vec{k}_1^{\,2}}{A_1} + \frac{\vec{k}_2^{\,2}}{A_2} + \frac{\vec{k}_3^{\,2}}{A_3} \right) = \frac{\hbar^2}{2m} \left(\vec{q}_l^{\,2} + \vec{p}_l^{\,2} \right) = \frac{\hbar^2}{2m} \kappa^2, \tag{3.25}$$

where m is the nucleon mass, E is the internal energy of the beam particles as well as the decay energy of unbound systems, and the relation $dE \propto \kappa d\kappa$ can be obtained.

Substituting Equation 3.21 into Equation 3.23, the wave-function in momentum space is

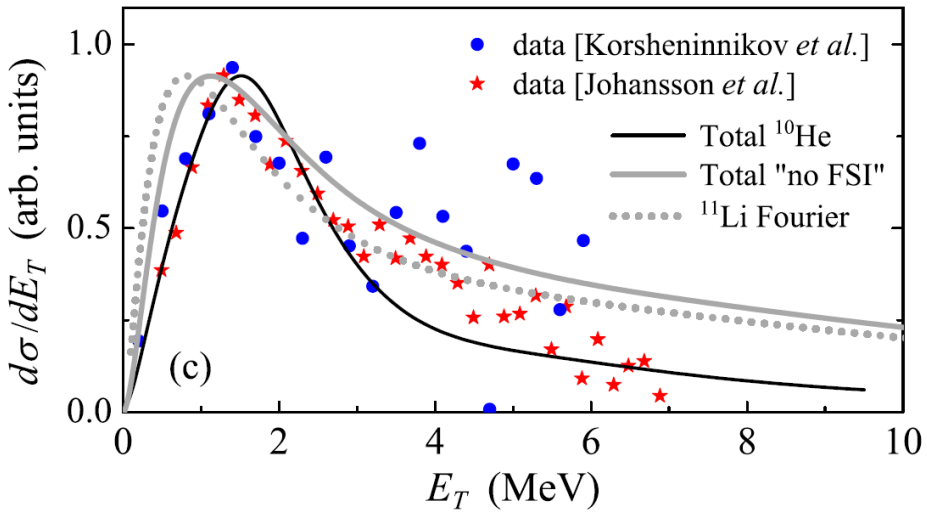

Figure 3.3: Measured and predicted spectra of ^{10}He from Ref. [39]. The line shape of the correlated background is denoted as "^{11}Li Fourier". The prediction of the three-body dynamical model is denoted as "Total ^{10}He".

obtained

$$\begin{aligned}\Psi\left(\vec{q}_l,\vec{p}_l\right) &= \frac{1}{(2\pi)^3}\int \exp\left[\mathrm{i}\left(\vec{q}_l\cdot\vec{x}_l+\vec{p}_l\cdot\vec{y}_l\right)\right]\Psi\left(\vec{x}_l,\vec{y}_l\right)\mathrm{d}\vec{x}_l\mathrm{d}\vec{y}_l \\ &= \sum_{KLl_xl_y}\chi^{l_xl_y}_{KL}(\kappa)\Gamma^{l_xl_y}_{KL}\left(\Omega^{\kappa}_5\right) \\ \chi^{l_xl_y}_{KL}(\kappa) &= \frac{\mathrm{i}^K}{\kappa^2}\int_0^{\infty}\chi^{l_xl_y}_{KL}(\rho)J_{K+2}(\kappa\rho)\rho^{1/2}\mathrm{d}\rho\end{aligned} \tag{3.26}$$

For $K=0$, the hyperspherical harmonic is a constant, and the wave-function of ^{11}Li has a simple form,

$$\Psi\left(\vec{x}_l,\vec{y}_l\right)\propto\frac{\exp\left(-\kappa_0\rho\right)}{\rho^{5/2}}. \tag{3.27}$$

Here κ_0 can be related to the binding energy E_b by $\kappa_0^2=2mE_{\mathrm{b}}/\hbar^2$. Substituting Equation 3.27 into Equation 3.26 and performing the radial integral gives

$$\Psi\left(\vec{q}_l,\vec{p}_l\right)\propto\frac{1}{\left(\kappa_0^2+\kappa^2\right)^{7/4}}F\left(\frac{7}{4},\frac{3}{4},3,\frac{\kappa^2}{\kappa_0^2+\kappa^2}\right), \tag{3.28}$$

where the function F is the standard hypergeometrical function [47]. Then the momentum

distributions are given by:

$$\frac{\mathrm{d}^6 N}{\mathrm{d}\vec{q}_l \mathrm{d}\vec{p}_l} \propto |\Psi\left(\vec{q}_l, \vec{p}_l\right)|^2 \propto \frac{1}{\left(\kappa_0^2 + \kappa^2\right)^{7/2}} F^2\left(\frac{7}{4}, \frac{3}{4}, 3, \frac{\kappa^2}{\kappa_0^2 + \kappa^2}\right) \tag{3.29}$$

Combining the phase space factor $\mathrm{d}\vec{q}_l \mathrm{d}\vec{p}_l = \kappa^5 \mathrm{d}\kappa \mathrm{d}\theta_\kappa \mathrm{d}\Omega_q \mathrm{d}\Omega_p$ and the relation $dE \propto \kappa d\kappa$ from Equation 3.25, the decay energy distribution of a ^{11}Li correlated background is

$$\frac{\mathrm{d}N}{\mathrm{d}E_{\mathrm{decay}}} \propto \frac{E_{\mathrm{decay}}^2}{\left(E_{\mathrm{b}} + E_{\mathrm{decay}}\right)^{7/2}} F^2\left(\frac{7}{4}, \frac{3}{4}, 3, \frac{E_{\mathrm{decay}}}{E_{\mathrm{b}} + E_{\mathrm{decay}}}\right). \tag{3.30}$$

The line shapes predicted from the correlated background model and the three-body dynamical model are shown in Fig. 3.3.

Chapter 4

Experimental Techniques

4.1 Beam Production

The experiment was carried out at the National Superconducting Cyclotron Laboratory (NSCL) at Michigan State University in August 2015. A non-halo ^{13}B beam and a halo ^{11}Li beam were used for populating ^{10}He or ^{9}He systems. Both ^{13}B and ^{11}Li are unstable against β decay with half-lives of 17.33(17) ms and 8.75(14) ms [48], respectively. They cannot be directly accelerated due to these short half-lives. Therefore, the fast fragmentation method [49] was used to produce these short lived species. The half-lives are long enough for them to be delivered from the fragment separator to the experimental vault.

A stable ^{18}O primary beam was accelerated to 120 MeV/u with the coupled K500 and K1200 cyclotrons at NSCL [50]. Targets of 3196 mg/cm^2 ^{9}Be and 2609 mg/cm^2 ^{9}Be were then bombarded by the primary beam for the production of ^{11}Li and ^{13}B, respectively. The thicknesses were different for optimizing the yields of the secondary beams. The fragmentation reactions produce a large variety of nuclei from which ^{11}Li or ^{13}B were selected by the A1900 Fragment Separator [51] based on the magnetic rigidities ($B_\rho = p/q$, where p is the momentum and q is the charge). A 1050 mg/cm^2 aluminum wedge was additionally inserted after the second dipole for better separation. The momentum slit for ^{13}B was set to 0.5 % to improve purity but for the more exotic ^{11}Li it was set to 2 % to increase intensity. The ^{11}Li

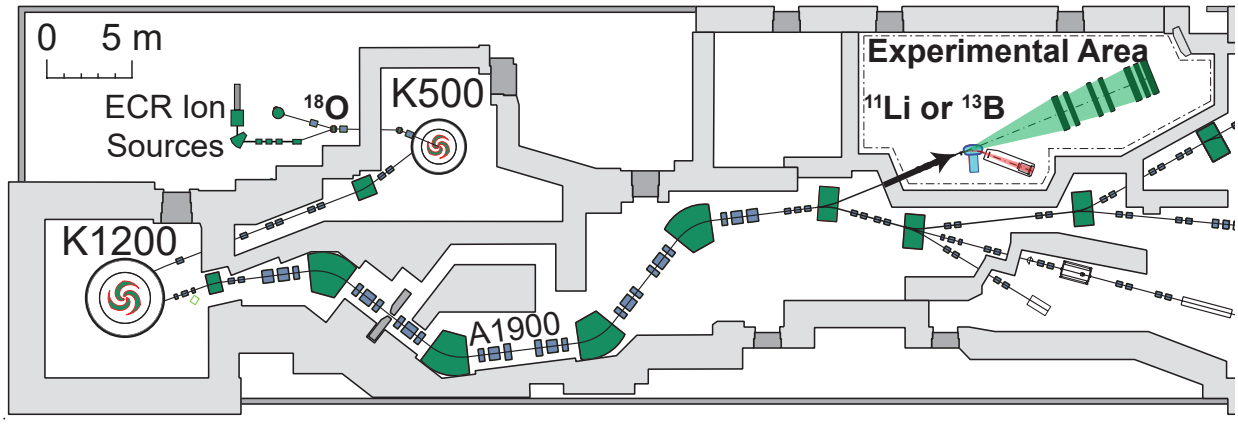

Figure 4.1: Schematic of the experimental area of the NSCL.

secondary beam was delivered to the experimental vault with a magnetic rigidity 3.55763 Tm, corresponding to 44.03 MeV/u. The ^{13}B beam was delivered to the experimental vault with a magnetic rigidity 2.60827 Tm, corresponding to 47.24 MeV/u. The layout of the NSCL experimental area is shown in Fig. 4.1.

4.2 Experimental Setup

After the A1900 Fragment Separator, the secondary beams entered the experimental area, which is shown as Fig. 4.2. The beams were focused by a quadrupole triplet magnet and then impinged on a 405 mg/cm^2 thick ^{9}Be reaction target. After leaving the reaction target, charged reaction fragments and unreacted beam particles were bent by a superconducting dipole magnet called Sweeper [52] into a vacuum box containing various charged particle detectors, including a pair of Cathode Readout Drift Chambers (CRDCs), an ionization chamber and a thin timing scintillator. The dipole magnet had a 43.3° bending angle and a 1 meter bending radius, and it could be operated at up to a magnetic rigidity of 4 T·m. For the ^{13}B beam, the current was set to 340 A, corresponding to a 3.6923 T·m magnetic

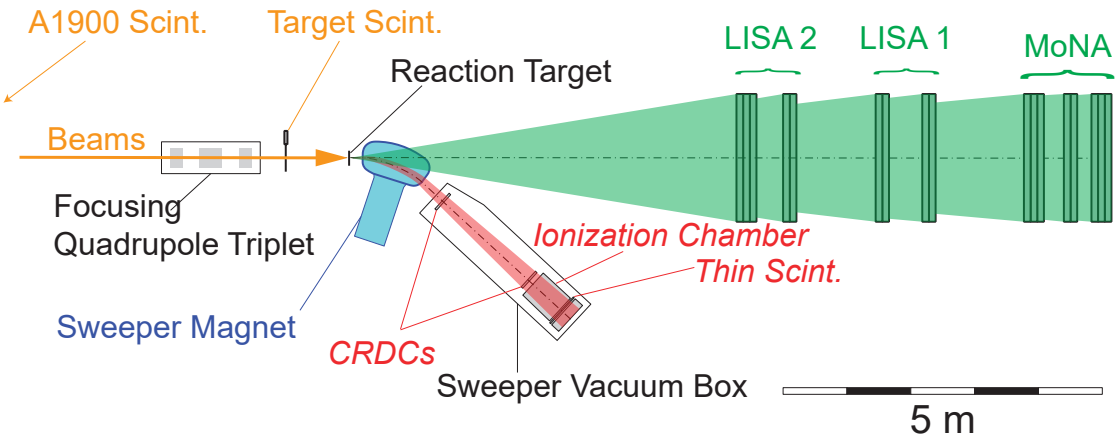

Figure 4.2: Schematic of the experimental area. LISA was placed on two separate tables with LISA 2 in the front table and LISA 1 in the back table. MoNA was placed on one table behind LISA.

rigidity. For the ^{11}Li beam, the current was set to 347 A, corresponding to 3.7498 T·m. The Sweeper magnet has a 14 cm vertical gap through which neutrons traveled straight without being diverted by the magnetic field. They were then detected by two plastic scintillator arrays called the Modular Neutron Array (MoNA)[53] and the Large-area multi-Institutional Scintillator Array (LISA) [54].

4.2.1 Charged Particle Detection

4.2.1.1 Timing Scintillators

Two out of the three timing scintillators were located in the beamline: the A1900 scintillator and the target scintillator. The A1900 scintillator was 1000 μm thick, located 10.88 m upstream from the reaction target. The target scintillator was 420 μm thick, located 1.04 m upstream from the reaction target. Each of the two scintillators was made of the organic plastic scintillator material BC-404 [55] and coupled to one photomultiplier tube (PMT). Combining the timing information provided by the A1900 scintillator and the target scin-

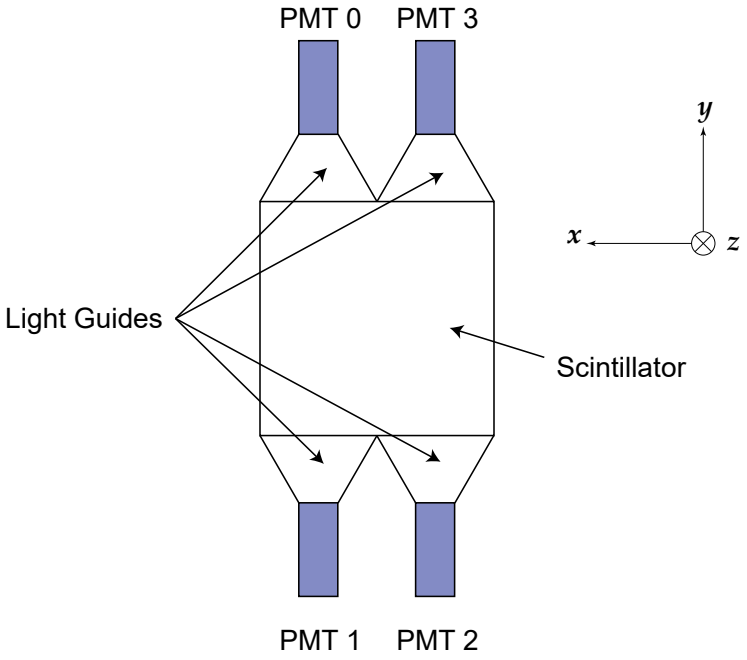

Figure 4.3: Schematic of the last thin scintillator viewed from upstream to downstream.

tillator, the time-of-flight (TOF) of beam particles could be measured. Energy deposited in the target scintillator was also measured as an auxiliary method for beam identification. Additionally, the radio-frequency (RF) of the cyclotrons was recorded, providing correlations with the primary beam that helped with beam separation.

The last timing scintillator was located immediately behind the ionization chamber in the Sweeper vacuum box. The size of this scintillator is 55 cm by 55 cm by 5 mm. Four PMTs were coupled to this scintillator through four trapezoidal light guides, as illustrated by Fig. 4.3. The materials used for the thin scintillator was organic plastic EJ-204, which is similar to BC-404 used for the A1900 and target scintillators.

Typical organic scintillators utilize the π-electron structure in the molecules polymerized into plastics. The energy interval between the first (S_0) and second (S_1) singlet states of

the π-electron are 3 to 4 eV for materials of interest. Each singlet configuration can be further divided into a series of levels with spacing on the order of 0.15 eV. Since the room temperature is equivalent to 0.025 eV which is much smaller than the spacing between those levels, most of the π-electrons are in the ground state. When a charged particle passes through, part of its energy lost in the plastic scintillators excites electrons to excited states. While higher-lying states quickly decay to S_1 through radiationless internal conversion, S_1 electrons de-excite to S_0 with prompt fluorescent light emitted. This light can be collected and multiplied by PMTs. The decay time of BC-404 and EJ-204 is 1.8 ns, and therefore fast counting is possible with these materials.

4.2.1.2 Cathode Readout Drifting Chambers

The first CRDC was located 1.73 m behind the reaction target, calculated along the central path of the Sweeper magnet. The distance between the two CRDCs was 1.54 m. The working gas used in the CRDCs was a mixture of 25% isobutane and 75% CF_4 at a pressure of 40 Torr, and the two CRDCs were physically connected by a single gas handling system. A 1000 V drift voltage was applied to each CRDC. When a charged particle passed through, it created electron-hole pairs along its path. Due to the applied drift electric field, those electrons moved towards the anode wire and 128 cathode pads distributed along the X-direction, as indicated in Fig. 4.4. The electrons caused an avalanche near the Frisch grid used for eliminating the position dependence of the drift electric field. The avalanche electrons then were collected by pads. The Y-position of the charged particle was determined by the drift time of the electrons. The X-position was determined by the charge distribution on the pads, which are further described in the next chapter. The centroid of the CRDC was used as the Z-position of the charged particle measurement. Combing the spatial measurements made

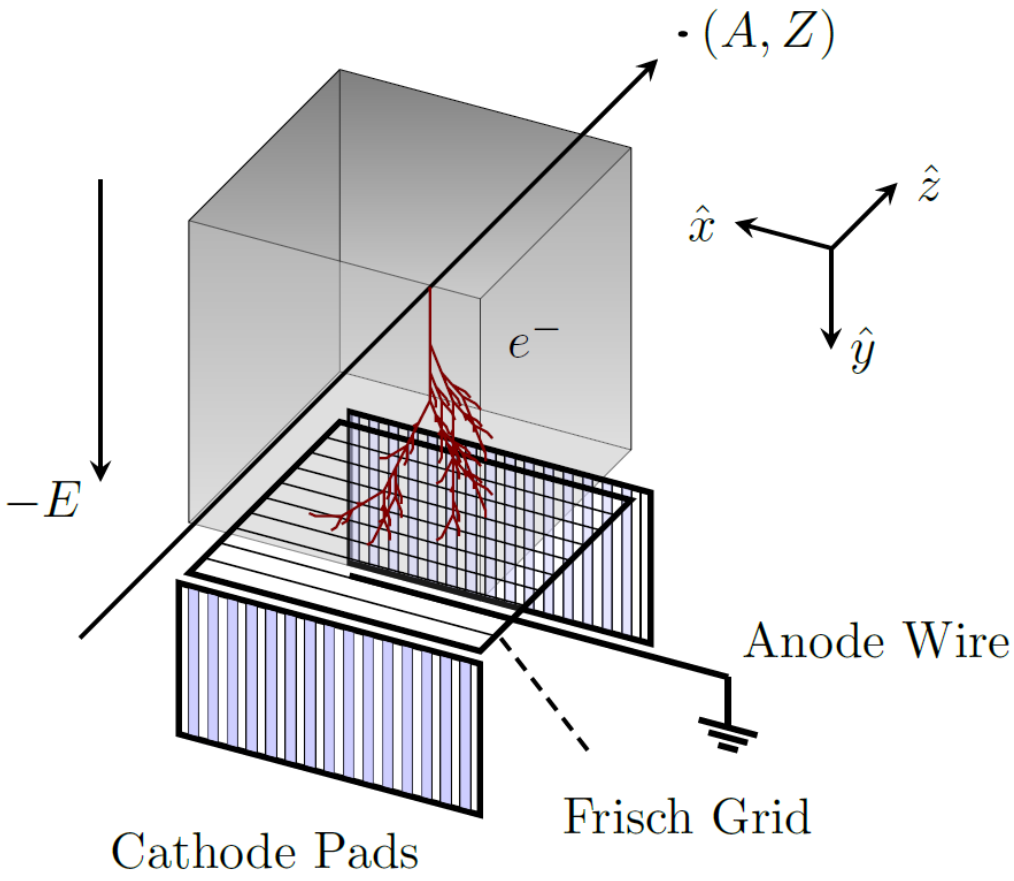

Figure 4.4: Schematic of a CRDC from Ref. [56]. The z-direction has been expanded.

by the pair of CRDCs, the angular distribution of the charged particles could be derived.

4.2.1.3 Ionization Chamber

The ionization chamber was located immediate behind the second CRDC. The mechanism of the ionization chamber is similar to the CRDCs. However, the fill gas in the ionization chamber was a mixture of 90 % argon and 10 % percent methane (P-10). The operating pressure during the experiment was 520 Torr and a drift voltage of 800 V was applied. The ionization chamber was used for measuring the energy loss of a charged particle in the gas, which can be used for charge number identification. Therefore 16 pads of the

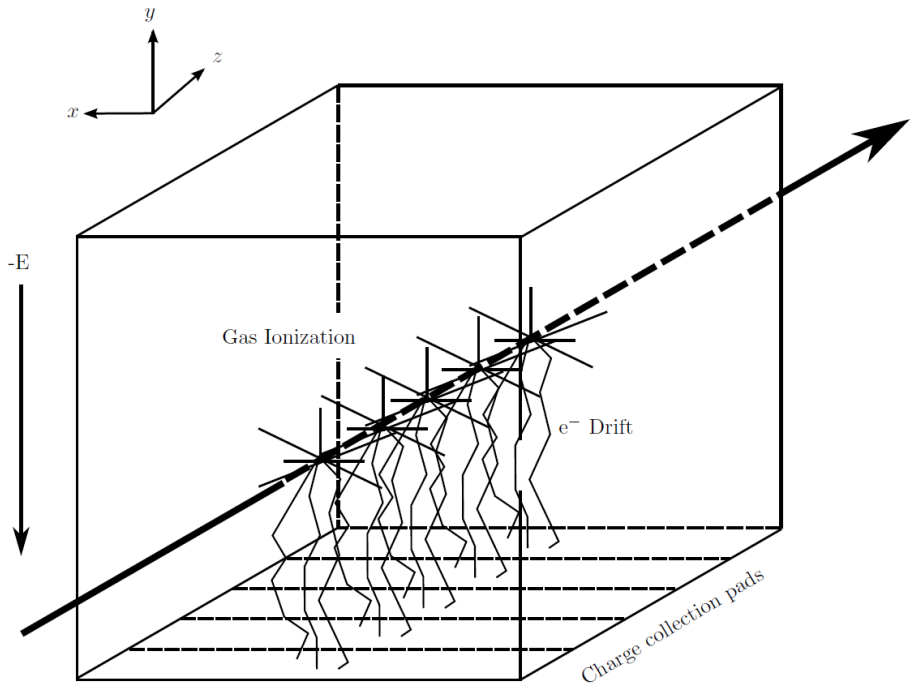

Figure 4.5: Schematic of the ionization chamber from Ref. [57].

ionization chamber were distributed along the Z-direction to increase the accuracy of the energy measurements, as shown in Fig. 4.5. The active volume was $40 \times 40 \times 65$ cm^3.

4.2.2 Neutron Detection

Neutrons were detected by the Modular Neutron Array (MoNA) [53] and the Large-area multi-Institutional Scintillator Array (LISA) [54]. They were designed to be identical modular arrays in terms of number of detector bars, electronics and DAQ. LISA was set on two tables during the experiment. The front table (LISA2) consisted of 5 layers of bars with the front face of the first layer at 6.05 m behind the reaction target. Each layer consisted of 16 bars with the exception of the first layer, where the top bar was missing since it was under repair at the time. There was a gap between the third layer and the fourth layer, because pre-experiment simulations showed that gaps help improve the multi-neutron detection effi-

ciency. The LISA 2 table hosted 4 layers of bars and there was a gap in the middle for the same reason. In total LISA had 143 scintillator bars. MoNA was positioned on one single table. There were eight layers with each layer consisting of 16 bars, and two gaps were after the third and fifth layer, as shown in Fig. 4.2. Originally MoNA had 9 layers of 16 bars each, but at the time of the experiment, the ninth layer was used at another experimental facility. In total there were 271 active bars in the experimental setup. Each bar was coupled to two photomultiplier tubes (PMTs) through light guides at the end of the bars. The Y and Z coordinates of a neutron hit were determined by the physical location of the bar, while the X position is derived from the difference of the TOFs measured by the PMTs attached to the two end of this bar. The TOF of the hit was the arithmetic average of the TOFs from the two PMTs while the light deposited was calculated as the geometric average of the light from each PMT.

MoNA consists of BC-408 and LISA consists of EJ-204 and the two materials are equivalent except they were made by different companies. Scintillation light was produced through similar mechanisms in those materials and is described in the Section 4.2.1.1. However, since neutrons do not carry charges, they cannot directly transfer energies to electrons. They must first undergo a (in)elastic scattering with a charged particle and transfer recoil energy. For elastic scattering, the recoil energy is:

$$E_R = \frac{4A}{(1+A)^2}(\cos^2\theta)E_n \tag{4.1}$$

where A is the mass number of the charged particle, E_n is the energy of the neutron and θ is the scattering angle in the lab frame. The formula indicates that the amount of detectable energy deposited decreases with increasing mass number. Therefore, a high hydrogen ra-

tio is desired for plastic scintillators aiming to detect neutrons. BC-408 and EJ-204 are polymerized from C_9H_{10} in order to achieve a high detection efficiency.

4.2.3 DAQ

Ref. [58, 59, 60, 56, 57] discussed the electronics and data acquisition (DAQ) for the setup in detail. This section provides a brief overview of the timing part and highlights the major temporary changes made to the electronics and DAQ during the experiment.

The trigger logic was processed by Xilinx Logic Modules (XLMs) with different levels. "Level 1" determined if there was a valid event in MoNA or LISA and passed the result to "Level 2". A valid event was defined as at least one detector bar having a valid signal from both constant fraction discriminators (CFD) receiving input from the PMTs at its two ends. Level 2 then waited for a system trigger. If a system trigger was received, Level 2 communicated with the DAQ and the event was recorded. Otherwise Level 2 sent a fast clear signal to Sweeper and MoNA-LISA electronics. The system trigger was provided by the PMT 0 in Fig. 4.3.

MoNA-LISA ran in common stop mode. Typically, the common stop for MoNA-LISA was provided by the CFD connected to the target scintillator. However, during the experiment, data with this setting could not simultaneously record timing and light deposited signals due to the high beam rates. Temporarily using the thin 0 signal as the common stop for MoNA-LISA fixed the issue. The timing of the new common stop depended on the time-of-flights of the charged reaction products. Thus, event by event corrections were necessary and details are discussed in the next chapter. The change is reflected in the abbreviated schematic Fig. 4.6.

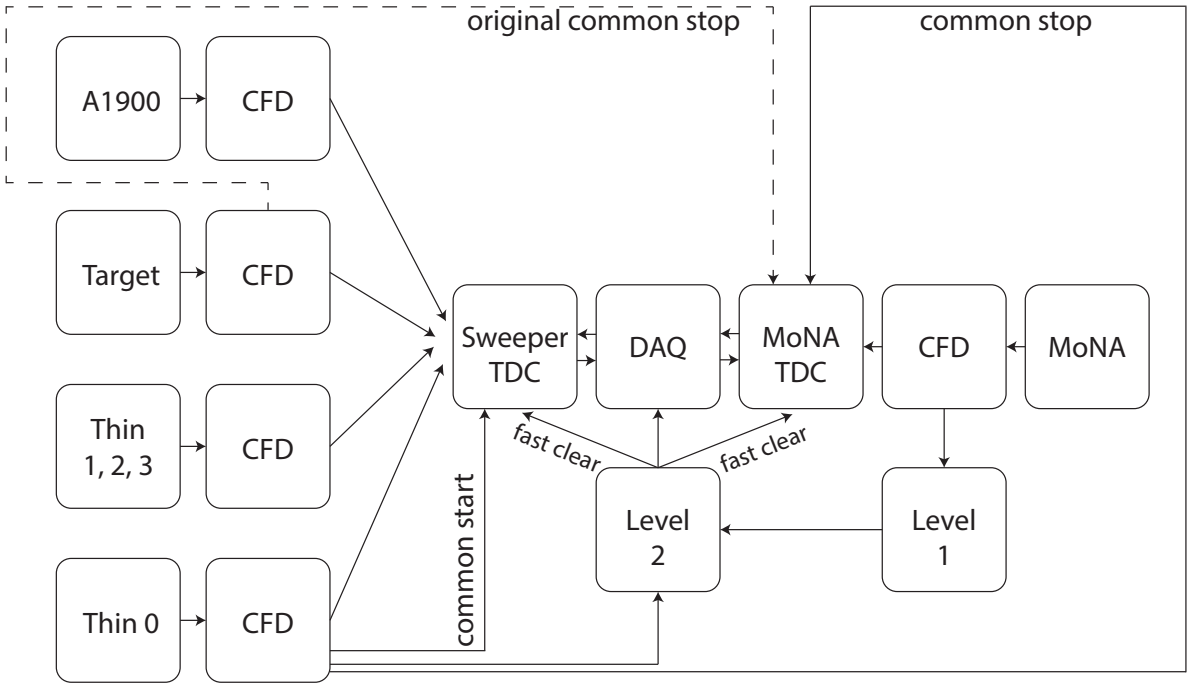

Figure 4.6: Abbreviated schematic of the electronics and DAQ. The electronics and DAQ of both MoNA and LISA are represented by the lable "MoNA".

4.3 Invariant Mass Spectroscopy

Direct measurements of neutron unbound states are not possible due to their very short lifetimes of about 10^{-22} s. However, the energies released from the decays of those states which are called decay energies can be measured through an indirect method named invariant mass spectroscopy. Considering a four-momentum of an unbound nucleus

$$\mathbf{P}_i^{\nu} = (E_A, \vec{p_A}) \tag{4.2}$$

where E_A is the total energy and $\vec{p_A}$ is the three-momentum. Relativistic momentum conservation gives

$$\mathbf{P}_A^\nu = \sum_{i=1}^{n} \mathbf{P}_i^\nu \tag{4.3}$$

where the right hand side is the sum of four-momenta over all n decay products of the nucleus.

The decay energy of the above mentioned unbound nucleus is

$$E_{\text{decay}} = M_A - \sum_{i=1}^{n} M_i \tag{4.4}$$

where M_A is the invariant mass of the unbound nucleus, defined as $M_A^2 = (\mathbf{P}_A^\nu)^2$, and M_i is the invariant mass of one of the decay products. Since M_A, M_i are Lorentz invariants, they can be calculated in any frame. Then in the rest frame of each decay product we have

$$M_i = m_i \tag{4.5}$$

where m_i is the rest mass of the decay product. M_A can be derived by

$$\begin{aligned} M_A^2 &= (\mathbf{P}_A^\nu)^2 \\ &= \sum_{i=1}^{n}\sum_{j=1}^{n} \mathbf{P}_i^\nu \mathbf{P}_{\nu i} \\ &= \sum_{i=1}^{n} M_i^2 + 2\sum_{i=1}^{n-1}\sum_{j=i+1}^{n} (E_i E_j - \vec{p_i}\cdot\vec{p_j}) \\ M_A &= \sqrt{\sum_{i=1}^{n} M_i^2 + 2\sum_{i=1}^{n-1}\sum_{j=i+1}^{n} (E_i E_j - \vec{p_i}\cdot\vec{p_j})} \end{aligned} \tag{4.6}$$

Explicitly, for a one-neutron decay, the decay energy is

$$E_{decay} = \sqrt{m_{A-1}^2 + m_n^2 + 2(E_{A-1}E_n - \vec{p}_{A-1} \cdot \vec{p_n})} - m_{A-1} - m_n \tag{4.7}$$

where the subscript $A-1$ represents the fragment and n represents the neutron from the decay. With two or more neutrons emitted, the expression of E_{decay} can be demonstrated with cross terms added.

Chapter 5

Data Analysis

This chapter first discusses how the raw data recorded from each electronic module were calibrated and how the events of interest were selected from the whole data set; then, the process of reconstructing physical observables will be described. Observables, like decay energy, cannot be directly compared with theoretical calculations since the experimental measurements include the resolutions, efficiencies, and acceptance of the experimental setup. Monte Carlo simulations that were used for extracting the physics of interest will be described at the end of the chapter.

5.1 Calibrations and Corrections

5.1.1 Timing Scintillators

As discussed in the previous chapter, timing scintillators were coupled to PMTs. The raw timing data from those PMTs were processed by time-to-digital converters (TDCs) and must be converted to nanoseconds. Because the FPGAs were operated at 50 MHz, the raw timing data from timing scintillators also contain a 20 ns jitter originating from the FPGA processing. Since a TDC measures the time interval between a scintillator and the master trigger (provided by "thin PMT 0", as illustrated in Fig. 4.3), the raw timing value from "thin PMT 0" was used for jitter subtraction event-by-event. The calibrated time for a

timing scintillator is:

$$t_{\text{cal}} = (t_{\text{raw}} - t_{\text{raw}}^{\text{thin0}}) \times 0.0625 \frac{\text{ns}}{\text{channel}} + t_{\text{offset}} \tag{5.1}$$

where 0.0625 ns/channel is the conversion from channel to nanosecond, determined by the manufacturer, and verified using a time calibrator module. The time offset t_{offset} was calibrated using data taken from a run for which the reaction target was out and the unreacted beam was centered (named a beam down center run hereafter). The time offset t_{offset} was chosen so that t_{cal} corresponded to the time that a particle traveling at the beam velocity passed through the scintillator, taking t=0 to be the time the beam passed through the target. Since the thin scintillator was coupled to four PMTs, the calibrated time was the average of the four PMTs' calibrated times.

For the target scintillator and the thin scintillator, the scintillator light output was also processed and recorded by analog-to-digital converters (ADCs). In the current analysis, light signals were only used for event quality checks, so they were left in arbitrary units. Because the thin scintillator had four PMTs, the PMT light signals were scaled so their centroids were aligned. The thin scintillator light output is given by

$$q_{\text{thin}} = \frac{\sqrt{q_{\text{top}}^2 + q_{\text{bottom}}^2}}{2} \tag{5.2}$$

where q_{top} and q_{bottom} are the average of the two top (PMT 0 and PMT 3) and the two bottom (PMT 1 and PMT 2) PMTs, respectively. For the A1900 scintillator, only timing information was recorded.

5.1.2 Cathode Readout Drifting Chambers

Multiple steps were taken to transform raw data from the CRDCs to spatial information of charged particle tracks.

As discussed in Section 4.2.1.2, charge distribution on CRDC pads were used to determine the X position of a charged particle passing through a CRDC. Therefore, the charge collected on each pad has to be correctly counted.

The charge collected on each pad was divided into one to four samples. A Riemann-sum used those samples to determine the charge integral on a pad. Therefore, the raw total charge on a pad is given by

$$q_{\text{pad}} = \frac{1}{N_{\text{sw}}} \sum_{i=0}^{N_{\text{sw}}} q_i \tag{5.3}$$

where N_{sw} is the number of samples (often referred to as the sample width) of the pad and q_i is the charge collected in a sample.

Two issues related to Equation 5.3 were encountered during data analysis. The first issue was the original code omitted the normalization by the sample width. The second issue was an overflow of the sample width. The sample width is calculated according to

$$N_{\text{sw}} = N_{\text{end}} - N_{\text{begin}} + 1 \tag{5.4}$$

where N_{end} and N_{begin} are the number of the first sample and the number of the last sample, respectively. Those numbers were assigned by the electronics, and they continuously increased from 0 to 31. If N_{begin} was large enough, N_{end} might exceed 31 and start counting from 0 again. If that happened, several samples were discarded since their sample number was smaller than N_{begin}, and 31 was used as N_{end}, making the calculated N_{sw} smaller than

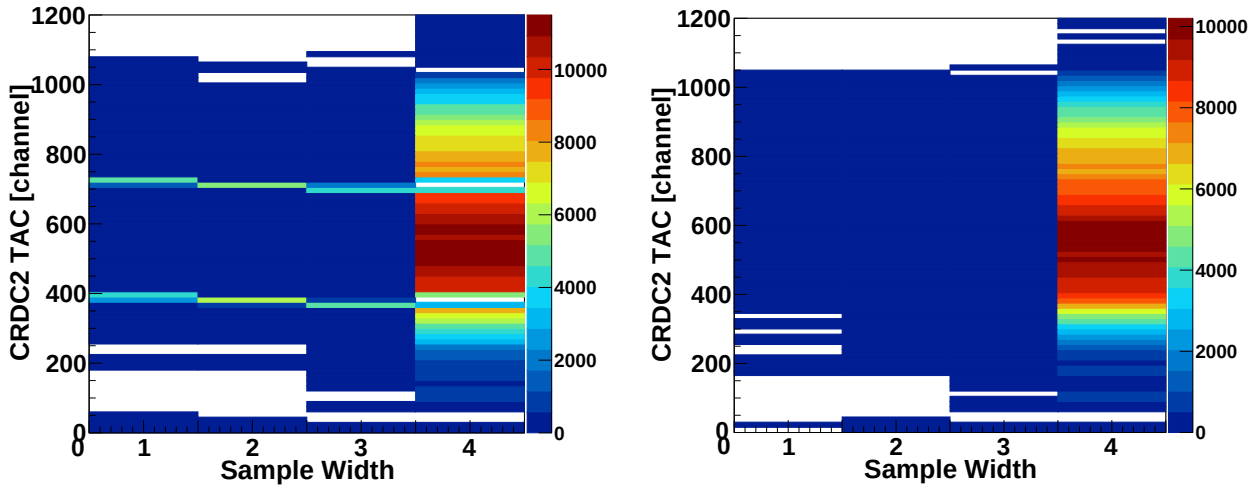

(a) (b)

Figure 5.1: CRDC2 TAC versus sample width. (a) before the N_{sw} overflow fix; (b) after the N_{sw} overflow fix.

what it should be. The overflow happened in coincidence with specific values of CRDC TAC, as can be seen in Fig. 5.1a. This issue was fixed by adding 32 to N_{end} when N_{end} was smaller than N_{begin}. A plot of CRDC2 TAC versus sample width after fixing the N_{sw} overflow issue can be seen in Fig. 5.1b.

Leakage currents in the CRDCs were also included in the pad charge readout; these are referred as pedestals. The pedestals had to be subtracted to correctly determine the total charge. Pedestal values for each pad were extracted from data taken when the beam was off.

After a Riemann-sum was completed correctly and the pedestal was subtracted, each pad needed to be gain-matched to account for differences in the electronics response of each channel to the same amount of charge. A continuous sweep run was used for the gain match. During this run, the reaction target was moved out, and the current of the sweeper magnet was gradually changed so the beam spot smoothly moved across the entire CRDC2.

A pad-max was identified on an event-by-event basis as the index of a pad with the largest pedestal-subtracted charge among all 128 pads of a CRDC. Pad 70 of CRDC1 and

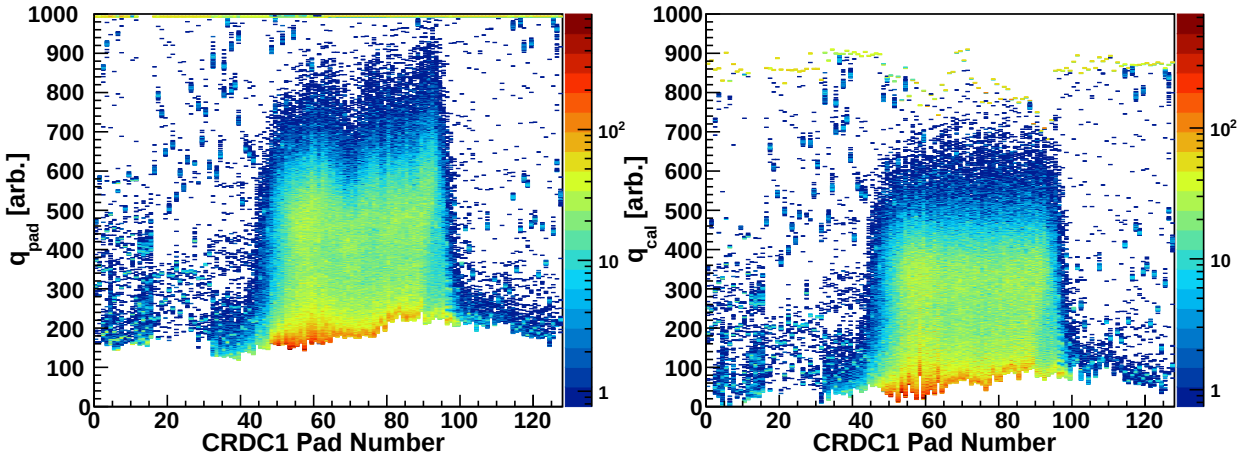

Figure 5.2: Raw (left) and calibrated (right) CRDC1 pad charge summary from a continuous sweep run.

Pad 81 of CRDC2 were selected as the reference pads. The charge spectrum of the reference pad was drawn using only events where the pad registering the maximum charge was close to the reference pad. By requiring this, it can be guaranteed that the charged particle passed nearby the reference pad. The mean value of this gated spectrum, m_{ref}, was extracted from a Gaussian fit. A similar procedure was used to obtain the mean value for all other pads. The gated spectra of other pads should be aligned with the gated spectrum of the reference pad since they were the response to the same amount of charge due to the same beam. Therefore, the gain-matched pad charge is given by:

$$q_{\text{cal}} = \frac{m_{\text{ref}}}{m_{\text{pad}}}(q_{\text{pad}} - q_{\text{ped}}) \tag{5.5}$$

where q_{ped} is a charge pedestal of the pad. The raw and calibrated spectra for CRDC1 and CRDC2 can be seen in Fig. 5.2 and Fig. 5.3, respectively.

For each event, the gain-matched charge registered by each pad plotted versus pad number was fit with a Gaussian to determine the interaction point in a CRDC in units of pad index.

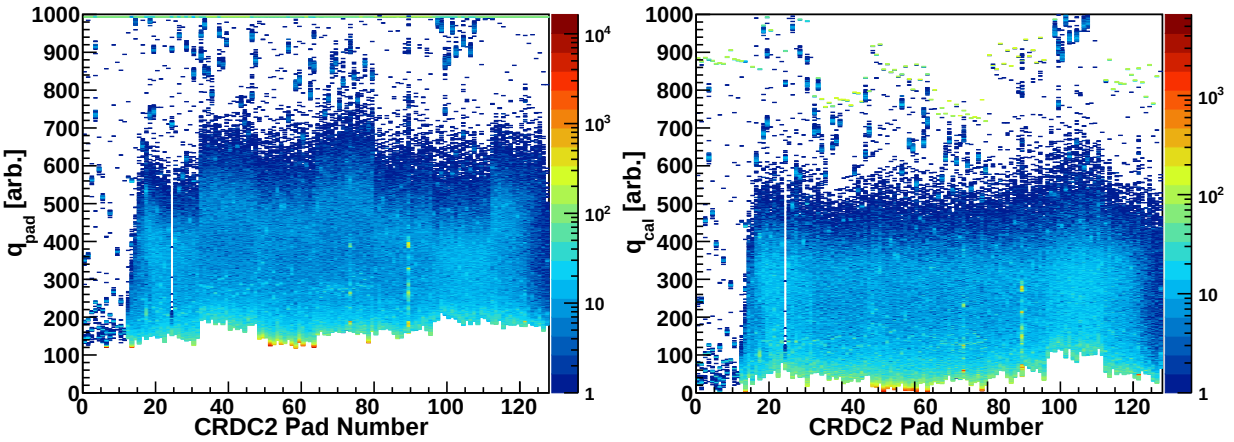

Figure 5.3: Raw (left) and calibrated (right) CRDC2 pad charge summary from a continuous sweep run.

Table 5.1: CRDC pads that were not used in fit

Device	Pad Number
CRDC 1	0-48, 95-127
CRDC 2	0-13, 24, 89, 124

Several pads exhibited irregular responses, so they were excluded from the fit. Since CRDC1 was closer to the magnet, areas far away from its center cannot be illuminated. Consequently, pads in those areas cannot be gain-matched and the charge collected on them cannot be correctly counted. Therefore, those ungain-matched pads were also excluded from the fit. The summary of all excluded pads are listed in Table 5.1.

As explained in Section 4.2.1.2, the Y position of a charged particle interacting with a CRDC was determined from the drift time of electrons. This drift time was measured by a time to amplitude converter (TAC). Slopes and offsets were needed to linearly transform the TAC data and the fitted pad number to Y position and X position, respectively. The X slopes were given by the 2.54 mm/pad spacing between pads. To determine X offsets and Y slopes, mask runs were used. For a mask run, a Tungsten mask with known holes and slits was inserted in front of a CRDC to block the beam, and only the areas right behind the holes

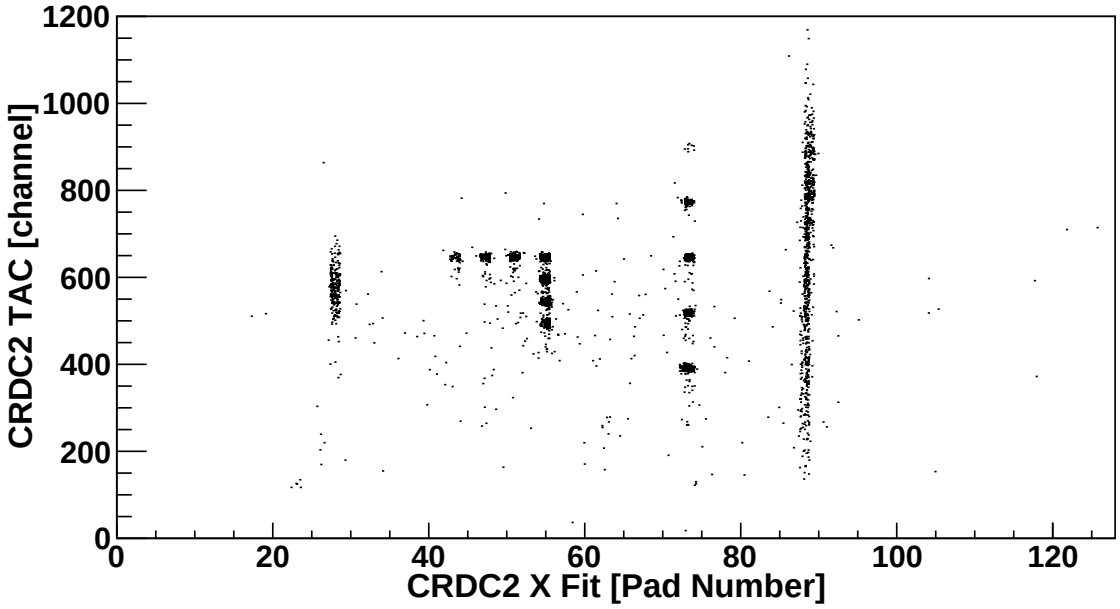

Figure 5.4: TAC versus CRDC2 X fit from a mask run.

and slits can be illuminated. An example spectrum of TAC vs. interacting point from a mask run is shown in Fig. 5.4, and it can be seen that holes and slits can be clearly identified. The known locations and distances between holes on the mask were used to calculate X offsets and Y slopes. However, since a mask might not be fully inserted, Y offsets obtained from a mask run might not be correct. Therefore, the Y centroid of a beam from a beam down center run was used to define Y=0. As a result, Y offsets for different beams were slightly different. The final offsets and slopes for the CRDCs are shown in Table 5.2. Note the sign change between devices for the X offset and slopes. This is because the pads are numbered from the opposite direction for the two CRDCs. Fig. 5.5 shows an example calibrated positions spectrum for the CRDC2.

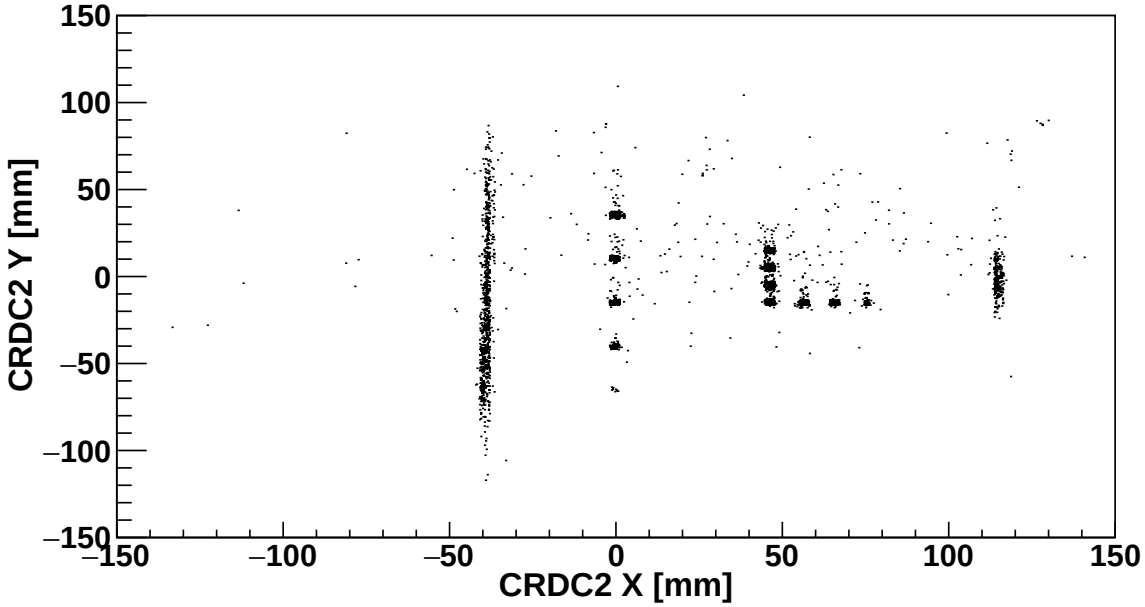

Figure 5.5: Calibrated CRDC2 Y versus CRDC2 X spectrum from a mask run.

Table 5.2: CRDC slopes and offsets

Device	X slope [mm/pad]	X offset [mm]	Y slope [mm/ch]	Y offset (^{13}B beam) [mm]	Y offset (^{11}Li beam) [mm]
CRDC 1	2.54	-185.2	-0.20	114.4	115.9
CRDC 2	-2.54	186.7	-0.20	112.2	118.4

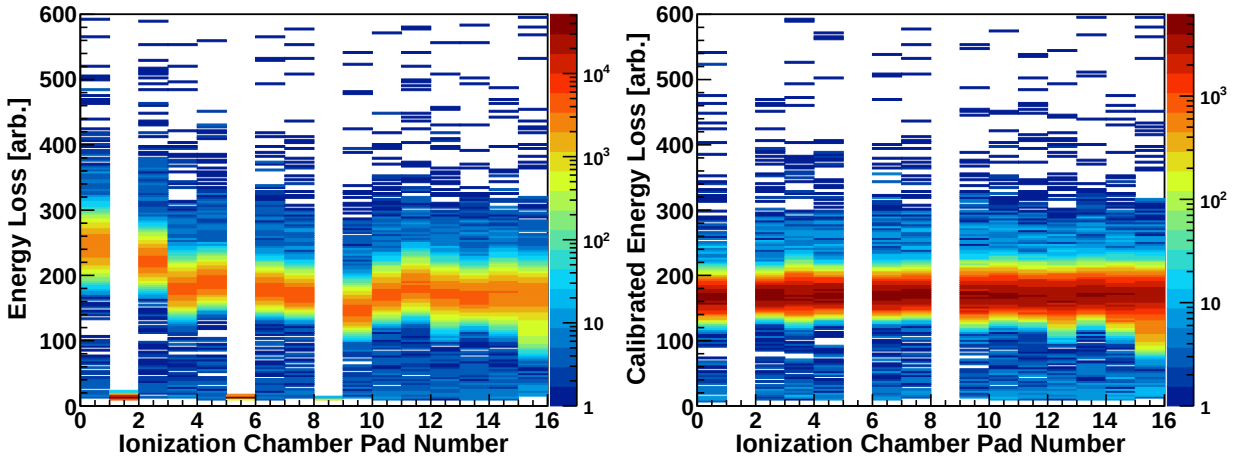

Figure 5.6: Raw (left) and calibrated (right) ionization chamber pad energy loss summary from a continuous sweep run.

5.1.3 Ionization Chamber

As discussed in Section 4.2.1.3, the energy loss of a charged particle that passed through the ionization chamber was measured by 16 pads along the Z direction. Signals from those pads were processed by analog-to-digital converters (ADCs). An ADC measures the height of a signal rather than integrating over the signal. Therefore, pedestals were not present in ionization chamber data so pedestal subtraction was not necessary. The raw energy loss of a pad was simply scaled so that the centroid of this pad was aligned with the centroid of the reference pad which was chosen to be Pad 7. A beam down center run was used for this calibration. Fig. 5.6 shows the energy loss of each pad before and after calibration. It also can be seen in Fig. 5.6 that Pad 1, Pad 5, and Pad 8 exhibited abnormal responses, so they were excluded from the rest of the analysis.

The average energy loss (ΔE) as measured by good pads, showed some dependence on the position of beam. Therefore, each calibrated pad was corrected using a fifth order polynomial, so that the energy loss of this pad as a function of CRDC2 X position was flat.

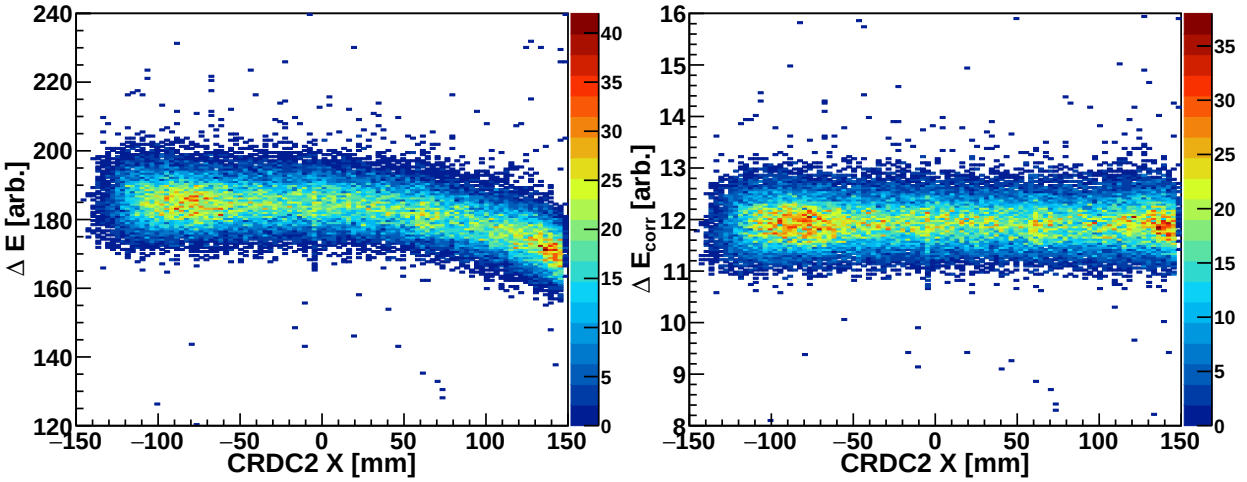

Figure 5.7: Original (left) and corrected (right) ionization chamber energy loss versus CRDC2 X from a continuous sweep run.

A beam down center run was used for this correction. The corrected energy loss, ΔE_{corr}, is given by the equation

$$\Delta E_{\text{corr}} = \frac{A}{N} \sum_{i=0}^{i=15, i\neq 1,5,8} \frac{q_i}{\sum_{n=0}^{5} k_{i,n} x^n} \tag{5.6}$$

where A is an arbitrary normalization factor, N is the number of good pads, q_i is the calibrated pad charge, $k_{i,n}$ is a correction coefficient, and x is the CRDC2 X position. The energy loss versus CRDC2 X position before and after applying the position correction can be seen in Fig. 5.7.

5.1.4 MoNA-LISA

5.1.4.1 Light Calibration

As described in Section 4.2.2, for one hit, scintillation light was produced in a bar of MoNA-LISA. This light signal was processed and recorded by charge-to-digital converters (QDCs) which were connected to the anodes of the two PMTs at the end of the bar. It was necessary

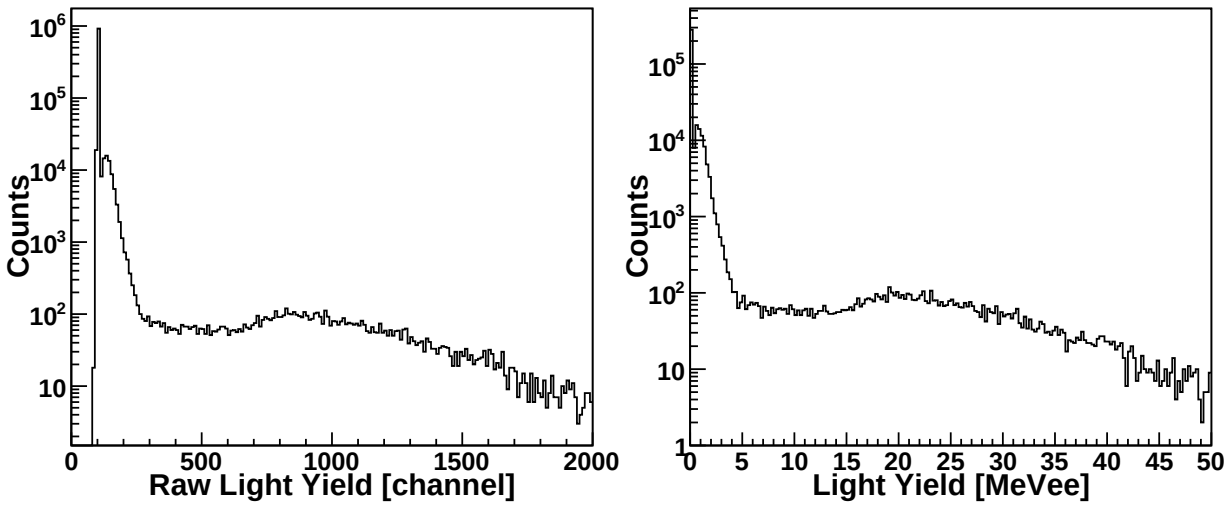

Figure 5.8: Example light spectra. The left panel shows the raw spectrum, where the peak of cosmic muon is at around channel 900. The right channel shows the calibrated light spectrum where the cosmic-ray peak appears at about 20 MeVee.

to convert raw QDC data to light yield in units of MeVee (MeV electron equivalent) so that the experimental light yield could be compared to simulations.

The linear QDC calibration was carried out using several cosmic-ray runs taken before the experiment. For a cosmic-ray run, each PMT of MoNA-LISA was operated in self-trigger mode, so data for cosmic muons could be recorded. The high voltage of each PMT was adjusted first to put the cosmic muon peak for all PMTs at about 900 channels in each raw QDC spectrum, as shown in the left panel of Fig. 5.8. Once this gain match was finished, a new cosmic-ray run was taken. The light yield of cosmic muons traveling a bar is about 20.5 MeVee. Therefore, offsets and slopes were chosen so that pedestals were placed at 0, and the cosmic muon peak was placed at 20.5 MeVee, as shown in the right panel of Fig. 5.8. The calibrated light yield of a bar was the geometrical average of the signals from its two PMTs, as described in Section 4.2.2.

Once the QDC calibration was finished, hardware QDC thresholds were set to suppress

pedestals. The values of these thresholds were determined by

$$QDC_{\text{thresh}} = \frac{q_{\text{ped}}}{16} + 2 \tag{5.7}$$

where q_{ped} is the pedestal value. These thresholds imposed cutoffs in 16-channel increments in the QDC spectra and above pedestals, since QDC raw data were stored in 12-bit while QDC thresholds were stored in 8-bit. Since hardware thresholds as well as QDC slopes, were different, those thresholds translated to different values in the unit MeVee. To achieve uniform thresholds in all calibrated spectra, a 0.91 MeVee post-experimental software threshold was applied to each PMT. The same light threshold was used for simulations.

5.1.4.2 Timing Calibration and Correction

The timing information of MoNA-LISA was processed and recorded by TDCs. The slopes converting TDC channel to nanosecond was calibrated with a time calibrator that provided pulses at 40 nanosecond intervals.

The time of an interaction in a bar was determined by the averaged time of both PMTs and is referred to as tmean. The reference time when the beam particles hit the target (tmean=0) reference was chosen as described in Section 5.1.1. A few steps were necessary to determine the offsets for all detectors.

First, tmean offsets for each bar were calibrated with a cosmic-ray run. This run was taken after the light calibration and the TDC slope calibration were completed. For each layer, the top bar was chosen as the reference bar. Then, muons that passed all 16 bars of the layer were used to calculate the expected time of each bar, since the velocity of 1 GeV cosmic muons is known to be 29.8 cm/ns [60, 56]. The tmean offsets for single bars were the

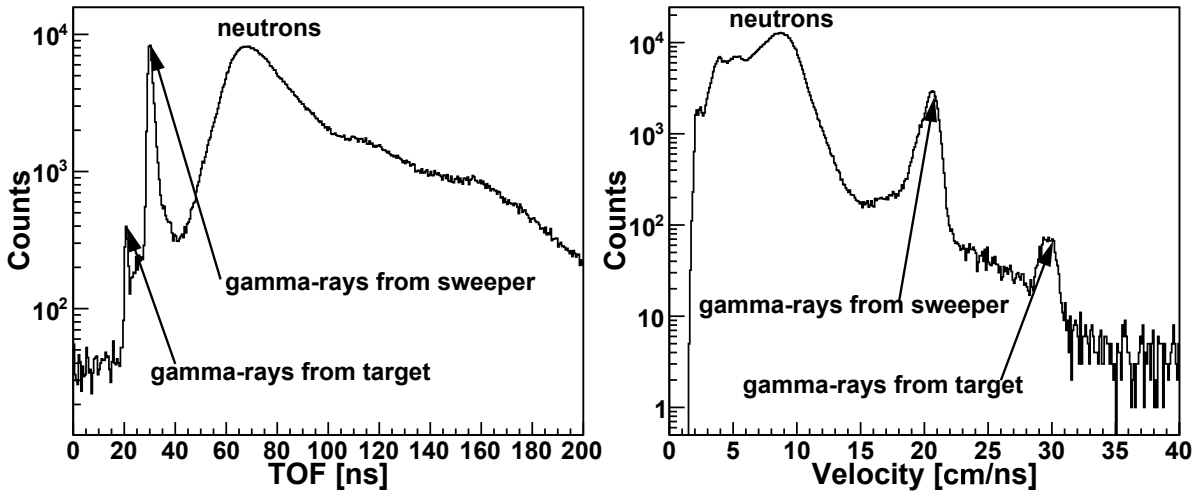

Figure 5.9: Corrected TOF and velocity spectra for MoNA-LISA. A coincidence with the front layer is required. Events in the first sharp peak in time are gamma-rays originating from the target; the peak was correctly placed at 30 cm/ns. The second sharp peak in time is due to gamma-rays produced by the beam hitting the Sweeper chamber. The velocities of the sweeper gamma-rays peak at less than the speed of light since in the calculation the TOFs from the target to the sweeper chamber for the beam particles were erroneously treated as part of the gamma-ray TOFs. The broad peak corresponds to the neutrons.

values that shifted the tmean of each these bar to the expected time.

Once the offsets for the bars were applied, muons that passed the top bar of one layer and the bottom bar of another layer were used to set offsets for one layer relative to another. The tmean offsets for layers were determined in a similar way as described above.

Due to the orientation of the detector tables, muons did not pass through bars on separate tables. Therefore, the global tmean offsets for each table could not be determined using cosmic-ray runs. Instead, a collimator run was taken before the production runs. A thick target was placed in the target chamber, and it was bombarded by the beams from the A1900 to produce a large number of gamma-rays. The expected γ-ray flight time was compared to the measured value to extract global offsets for each table.

Usually these steps provided accurate tmean values for MoNA-LISA. However, as described in section 4.2.3, during the experiment, the common stop for MoNA-LISA was

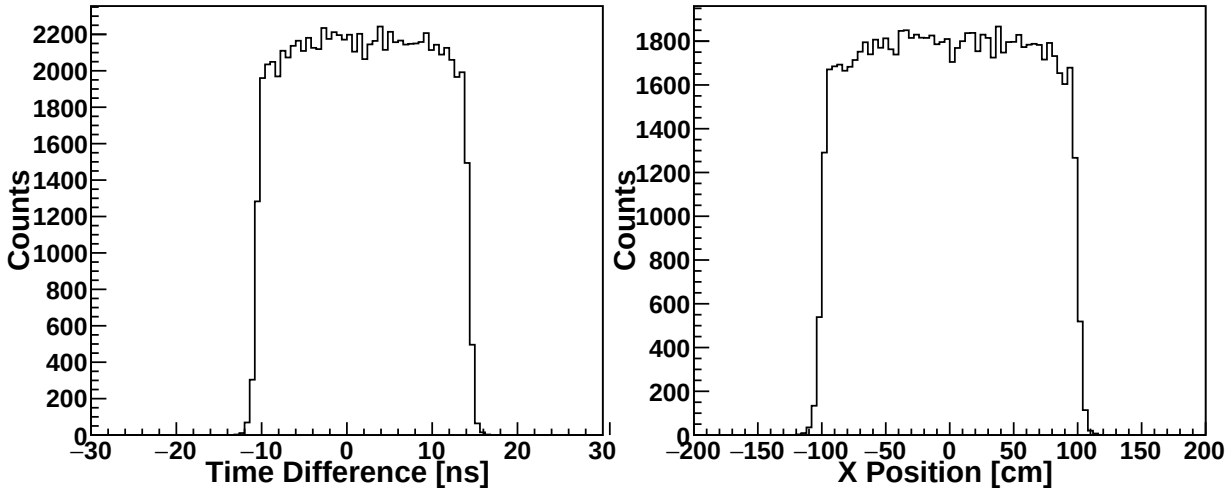

Figure 5.10: Example time difference spectrum and X position spectrum for one MoNA-LISA bar.

changed to the thin 0 signal from the target scintillator signal. This change happened after the collimator run. This change meant the common stop was delayed by an amount of time that varied event-by-event,

$$TOF_{\text{corr}} = TOF - (t_{\text{cal}}^{\text{thin0}} - t_{\text{cal}}^{\text{target}}) + \text{offset}, \tag{5.8}$$

where TOF is the original MoNA-LISA time of flight. An offset was needed since delay cables were added to the new common stop. To determine this offset, TOF and velocity spectra were plotted with all ^{13}B beam production runs chained together. The offset was chosen so the gamma-rays from the target peaked at 30 cm/ns, as shown in Fig. 5.9.

5.1.4.3 Position Calibration

The X position of an interaction along a bar was determined by the time difference between the left and right PMT signals. A linear calibration was used, and the time difference spectra of bars were plotted with a long cosmic-ray run. This cosmic-ray run was taken after time

calibration was finished, and it required that both PMTs of a bar registered a signal. Fermi functions were used to find the edges. The slope of a bar is given by:

$$\text{slope} = \frac{200 \text{ cm}}{R_{\text{edge}} - L_{\text{edge}}} \tag{5.9}$$

where 200 cm is the physical length of a bar. The offset is given by

$$\text{offset} = 100 \text{ cm} - \text{slope} \times R_{\text{edge}} \tag{5.10}$$

where 100 cm is used to put the center of the time difference at zero. The raw time difference spectrum and the X position spectrum of a bar are shown in Fig. 5.10.

5.2 Event Selection

Although the experiment was designed to measure ^{10}He from specific secondary beams, these desired ^{10}He events accounted for a small portion of the experimental data. Other isotopes produced by the beams, or reaction products from other beam components, were recorded as well. On the other hand, events might contain inaccurate or invalid information. For example, if the charge collected by a CRDC in an event was incomplete, the X position from the fit of the pad charge distribution, which is described in Section 5.1.2, might not be valid. This section covers how events of interest and of good quality were selected from the whole data set.

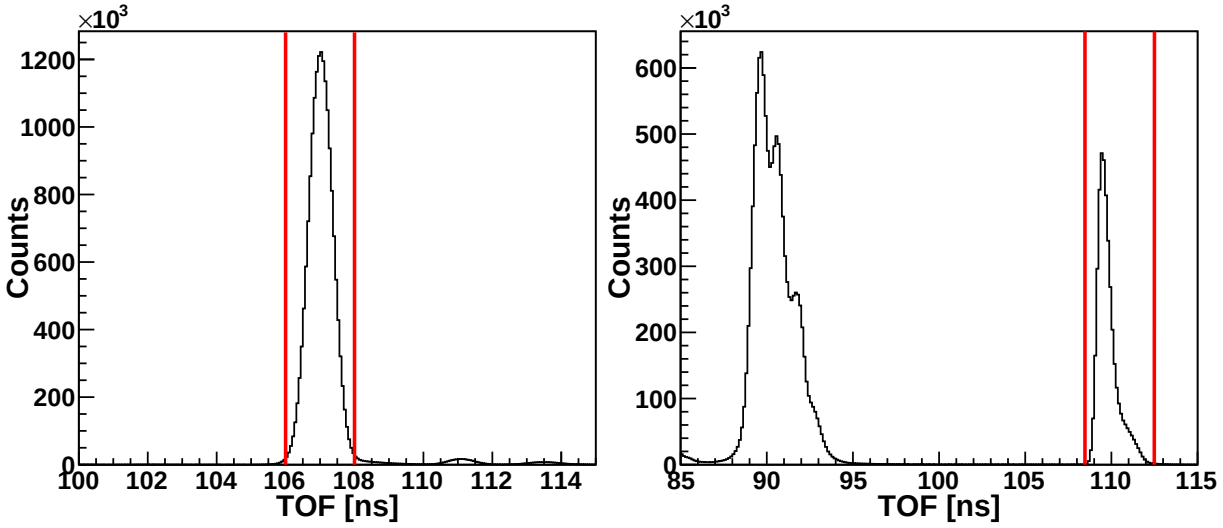

Figure 5.11: TOF for incoming beams from the A1900 scintillator to the target scintillator. Events between solid red lines were selected as in coincidence with interested beams. The left panel shows the ^{13}B beam gate, and the right panel shows the ^{11}Li beam gate.

5.2.1 Beam Identification

Even though in the A1900 Separator devices such as wedges and slits were used to limit transmission of other beams, secondary beams were not pure. However, since the A1900 Separator selected charged particles with the same rigidity, other beam species arrived at the experimental area at a different time since their A/Z ratios were different from the beam of interest. Therefore, events originating from different beams can be separated by their TOFs between the A1900 scintillator and the target scintillator.

Fig. 5.11 shows beam gates for the ^{13}B and ^{11}Li beams. While the ^{13}B beam was almost pure, the ^{11}Li beam was not. In order to increase the ^{11}Li rate, a momentum slit had to be opened large, allowing additional beam contaminants to leak through. Nevertheless, the right panel of Fig. 5.11 shows that ^{11}Li were well separated from the contaminants.

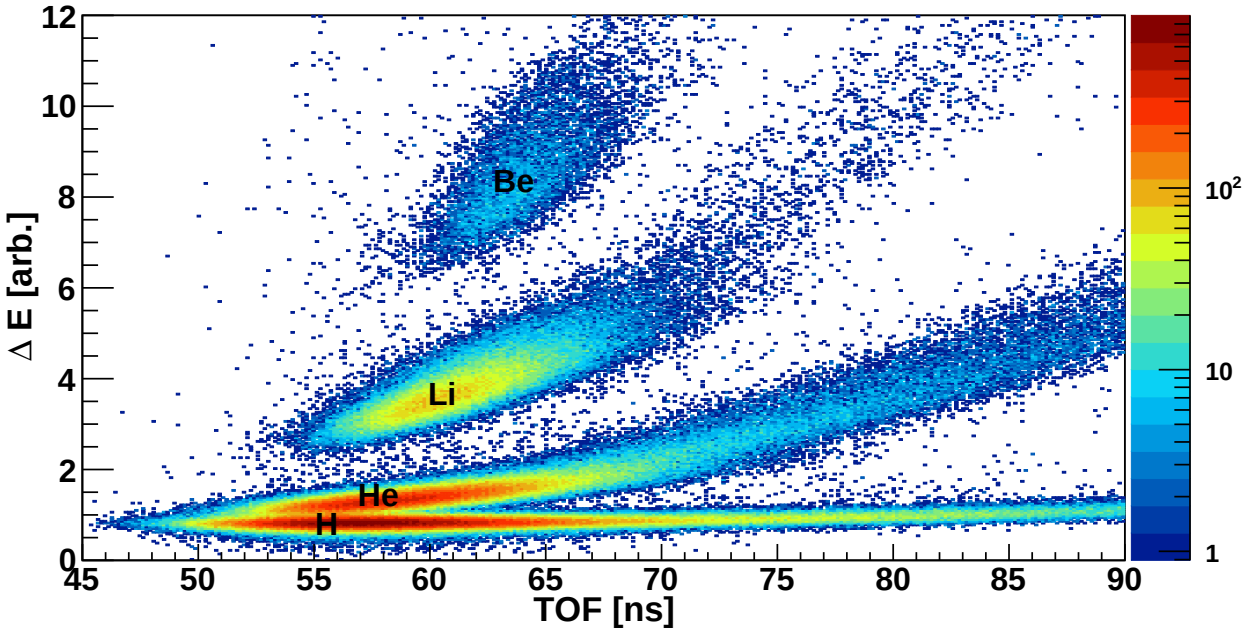

Figure 5.12: Energy loss in the ionization chamber vs TOF from the target scintillator to the thin scintillator for the ^{13}B beam. Neutron coincidence was required.

5.2.2 Element Identification

The energy loss of a charged particle in matter is determined by the Bethe formula [61],

$$-\frac{dE}{dx} = A\frac{Z^2}{v^2}B(v), \tag{5.11}$$

where A is a constant, Z is the charge number of the particle, v is the velocity and $B(v)$ changes slowly with particle energy for non-relativistic particles. That means ΔE measured by the ionization chamber was proportional to Z^2/v^2. Element identification (Z separation) was achieved by plotting the ionization chamber ΔE versus the TOF from the target scintillator to the thin scintillator. An example plot used for element identification is shown in Fig. 5.12. Element bands can be clearly seen and identified. 2D gates can be drawn around these bands to select individual elements.

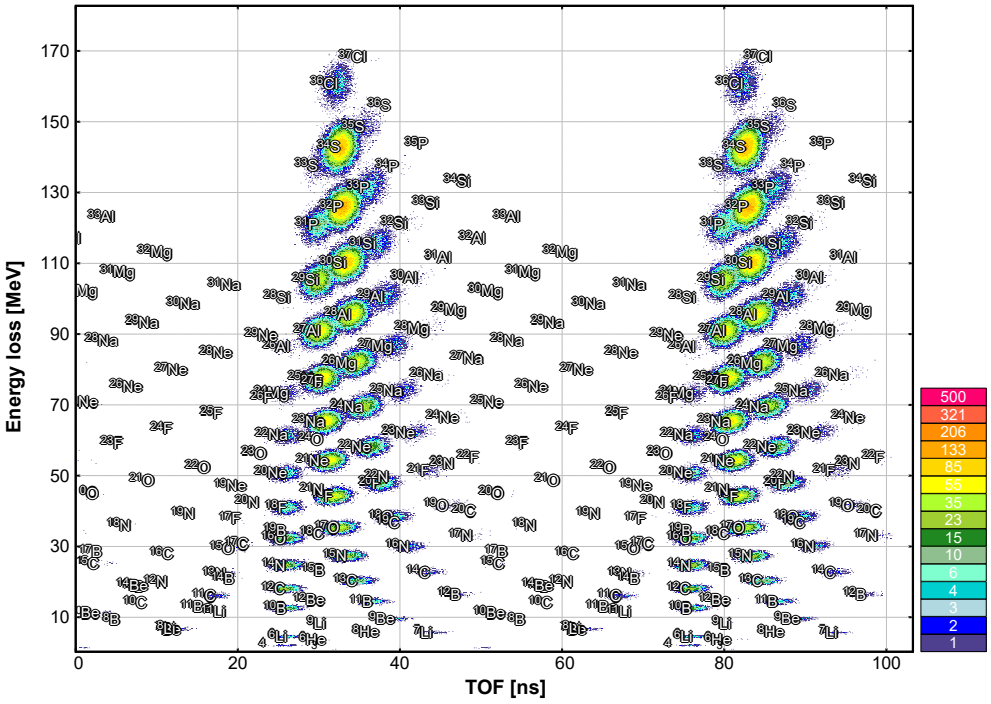

Figure 5.13: Example S800 ionization chamber energy loss versus TOF used for particle identification. The fragmentation of an 85 MeV/u ^{36}Ar beam was simulated using LISE++ [62].

5.2.3 Isotope Identification

For a spectrometer used for bound nuclei experiments, such as the S800 at NSCL, element identification and isotope identification are simultaneously achieved, as shown in Fig. 5.13. However, the same separation was not observed in Fig. 5.12 because the Sweeper magnet is just a bending magnet and not a full spectrometer. Also the short flight distance reduced the TOF resolution. In addition, the energy and angular spreads of the charged particles for the current neutron-unbound experiment were larger due to neutron decays. As a result the individual isotope overlapped with the element bands. Nevertheless, for a given element, different isotopes follow different trajectories, and if appropriate variable transformations are made, different isotopes can be separated.

The TOFs from the target scintillator to the thin scintillator, X position in the focal

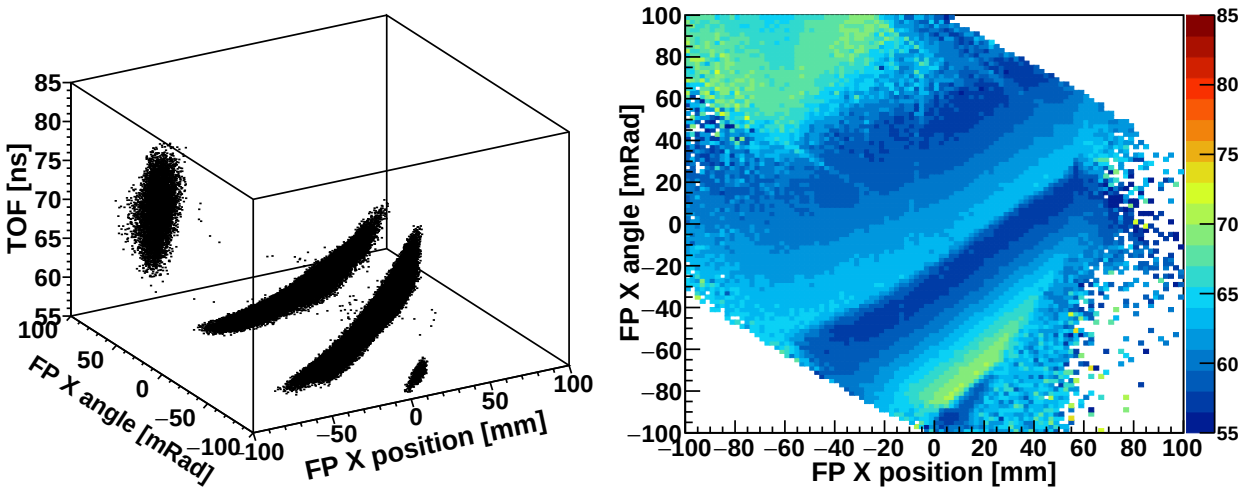

Figure 5.14: 3D correlation and 2D projection of He isotopes from the ^{13}B beam. The color in the right panel represents TOF (the z-axis in the left panel). In the 3D plot, the cluster that is in between 60 ns and 75 ns, and away from the other three bands, corresponds to He particles that hit the Sweeper chamber. They were excluded from further analysis.

plane (FP), and X angle in the FP were selected for isotope identification.

As shown in the left panel of Fig. 5.14, isotopes were well-separated in the 3D plot of the TOFs from the target scintillator to the thin scintillator, X position in the focal plane (FP), and X angle in the FP. Then, auxiliary variables were constructed to decorrelate each isotope. The first is used to decorrelate the FP position and angles. It is defined as

$$xtx = \theta_{x,FP} - (a \cdot x_{FP} + b \cdot x_{FP}^2) \tag{5.12}$$

where x_{FP} is the focal plane X position, $\theta_{x,FP}$ is the focal plane X angle, and a and b are constant coefficients. The two coefficients were extracted from fitting the boundary between the light blue and dark blue in the 2D projection with a second order polynomial. Then, xtx could be drawn against TOF, as shown in Fig. 5.15. Now the isotope bands could be identified in a 2D variable space. A final variable was constructed that projected the three bands into a 1D plot. It is defined as

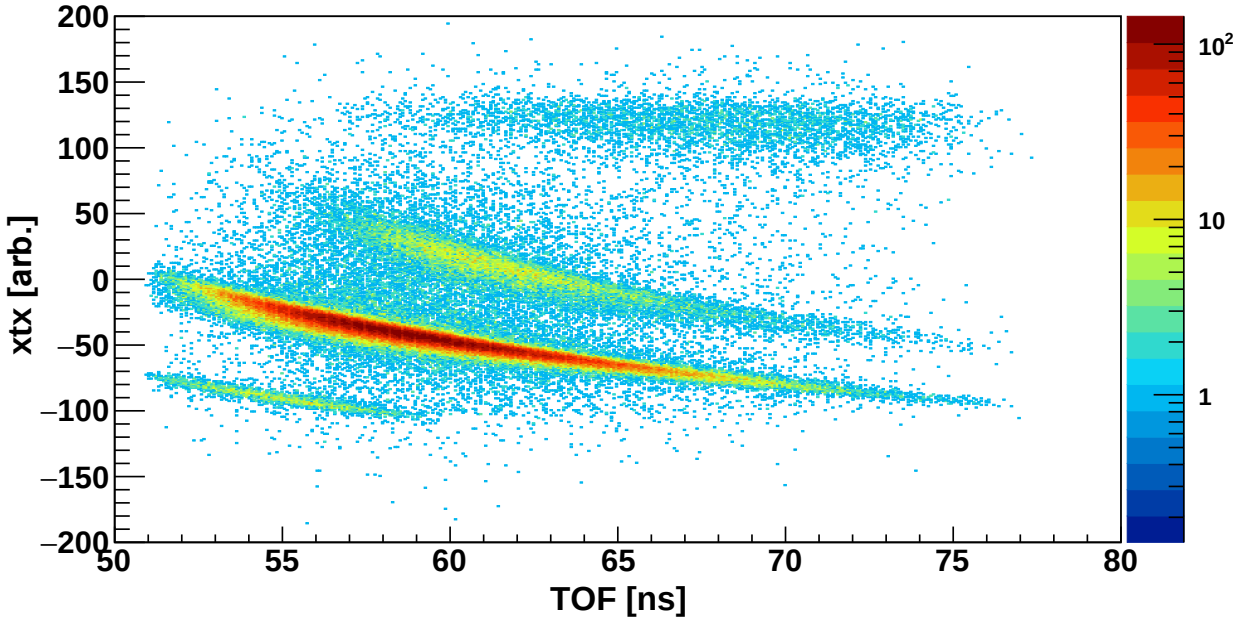

Figure 5.15: xtx versus TOF for He isotopes from the ^{13}B beam. The most intense band is attributed to ^{6}He.

Table 5.3: Coefficients used for isotope identification

Beam	a	b	c	d
^{13}B	0.717268	0.00281395	-35.538	0.231951
^{11}Li	0.659213	0.00411903	-9.08	0

$$xtx\_tof = xtx - (c \cdot TOF + d \cdot TOF^2) \tag{5.13}$$

where TOF is the time-of-flight from the target scintillator to the thin scintillator, and c and d are constant coefficients. The two coefficients were extracted from fitting an isotope band in the xtx vs. TOF plot with a second (first) order polynomial.

An xtx_tof spectrum for He isotopes is shown in Fig. 5.16. Similar spectra for heavier elements might display large overlaps between isotope peaks. However, since ^{5}He and ^{7}He are unbound, He isotopes can be clearly separated and identified in Fig. 5.16. All coefficients used for He isotope identification are listed in Table 5.3.

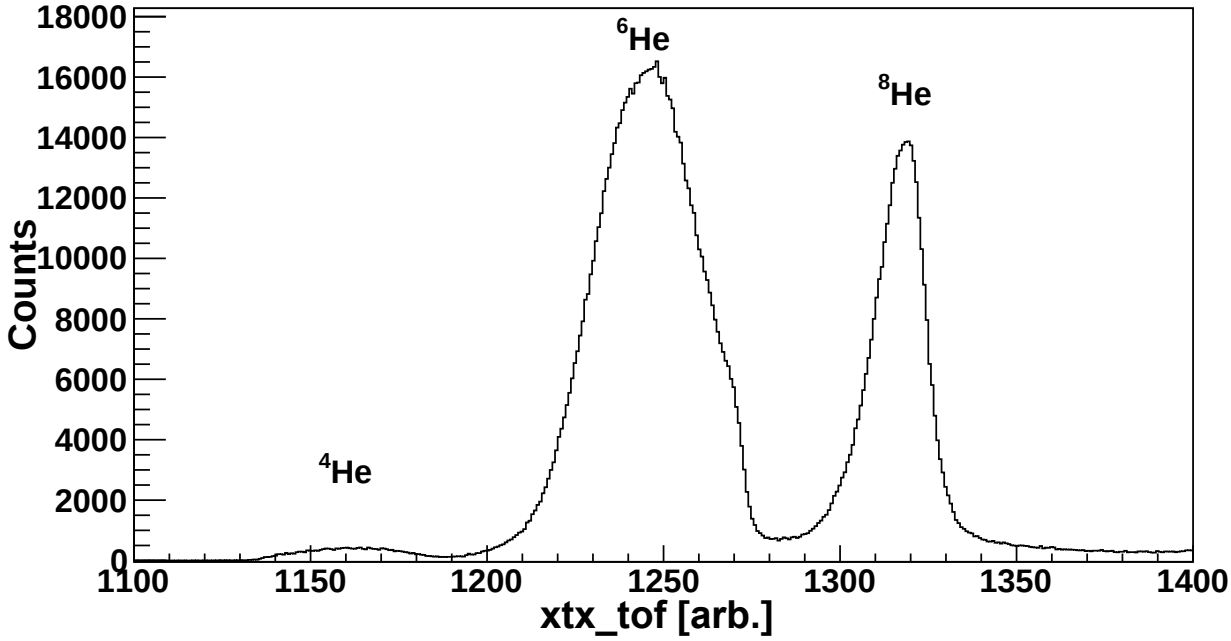

Figure 5.16: *xtx_tof* used for isotope identification in the ^{13}B beam data set.

5.2.4 Event Gates

Event gates were used to improve the accuracy and validity of selected events. Not all event gate were necessary for all isotopes form the different beams.

5.2.4.1 CRDC Gates

The accuracy of position information measured with the CRDCs was crucial to extracting information about the fragments leaving the target. In Fig. 5.17, the CRDC padsum is plotted against the sigma of a Gaussian fit to the charge distribution across CRDC pads. The plots show a band where the width increases with padsum. Events deviating from this band were excluded by applying 2D gates as shown in the figure.

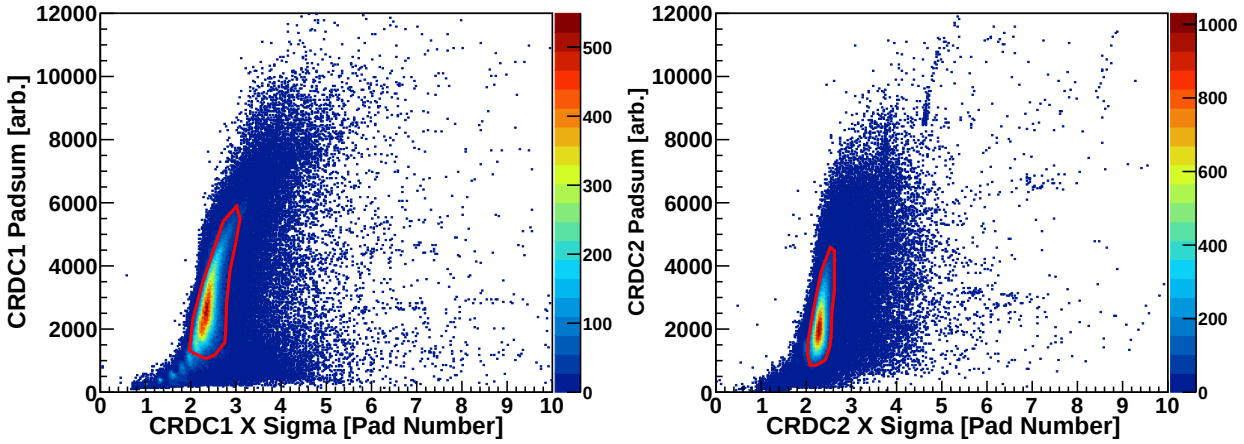

Figure 5.17: CRDC Padsum versus X sigma for ^{8}He fragments from the ^{13}B beam. CRDC quality gates are shown as red circles. Each gate selects approximately 80% of the events registered by a CRDC.

5.2.4.2 Neutron Gates

MoNA-LISA recorded signals not only from neutrons, but from gamma-rays, charged particles, and random events. Light yield was plotted against TOF throughout the whole 400-ns TDC window, as shown in Fig. 5.18. The time range between 50 ns and 150 ns corresponds to beam velocity neutrons and events outside this range were excluded. A uniform band of events below 3 MeVee distributed throughout the time window for both beams was due to uncorrelated random evens (mostly gamma-rays). The random rate for ^{13}B was 7 times bigger than for ^{11}Li. Therefore, a 3 MeVee light gate was applied to data from the ^{13}B beam, and no light gate was applied to ^{11}Li data, as a trade-off between reducing noise and keeping good events.

5.2.4.3 Beam Gates

As shown in Fig. 5.19, the ^{13}B beam production run contained background events in the target scintillator light output spectrum. These might be caused by random events due to

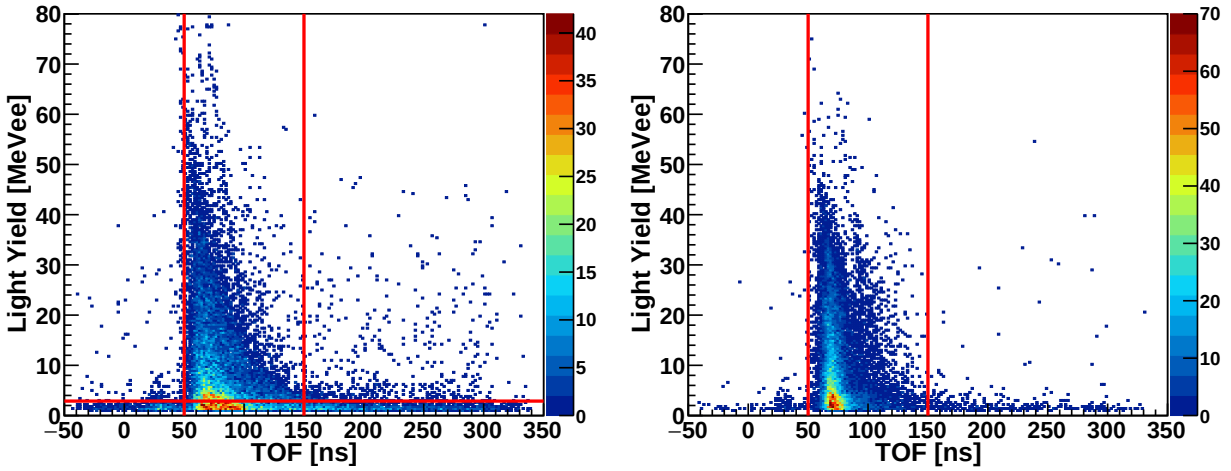

Figure 5.18: MoNA-LISA light yield versus TOF for ^{8}He fragments from the ^{13}B beam (left) and the ^{11}Li beam (right). Events between the vertical lines and above the horizontal line are selected as good neutron events. ^{8}He fragments originating from the ^{11}Li beam (right panel) do not have a light yield gate (thus the absence of a horizontal line).

the high beam rate. Therefore, a horizontal gate in the target scintillator light spectrum was applied to data from the ^{13}B beam to remove those events. The light output from the ^{11}Li beam did not exhibit such events, thus no gates were not applied to the ^{11}Li beam.

5.3 Classification of Two-Neutron Events

5.3.1 Causality Cuts

The reconstruction of three-body decay energies requires the correct identification of two-neutron events. Even if MoNA-LISA records two interactions in coincidence with a ^{8}He fragment, it is possible that a neutron scatters in one bar and then subsequently interacts in another, creating two interactions that can be incorrectly identified as two neutrons. These cases are called "false 2-neutron events". In contrast, if two different neutrons are detected, the event is a "true 2-neutron event". Contributions from false 2-neutron events can be

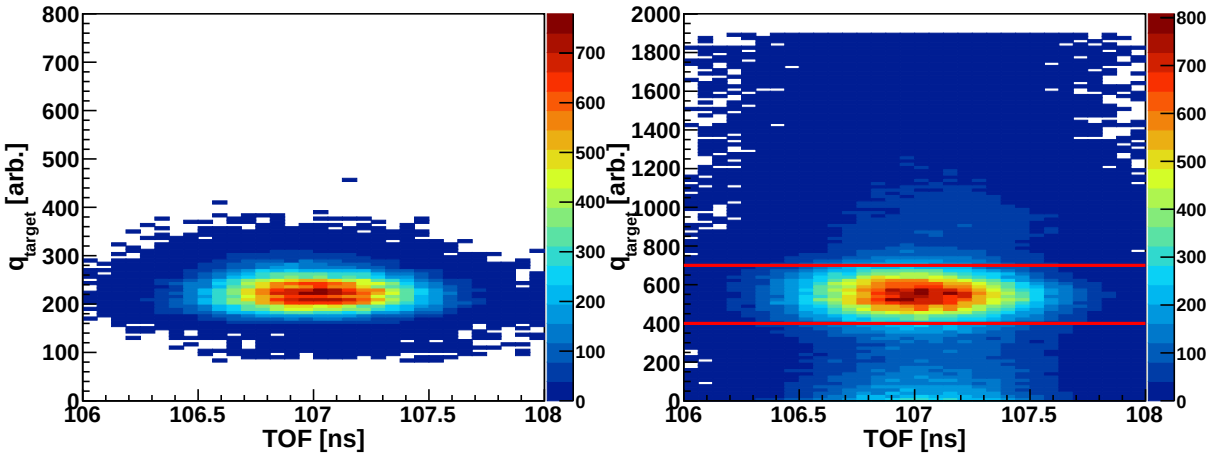

Figure 5.19: Target scintillator light output versus TOF from the A1900 to the target scintillator for ^{8}He fragments using the ^{13}B data from a beam down center run (left) and a production run (right). Events between outside the red lines were excluded from data. The vertical scales are different since the voltage of the target scintillator PMT changed between the beam down center and the production run.

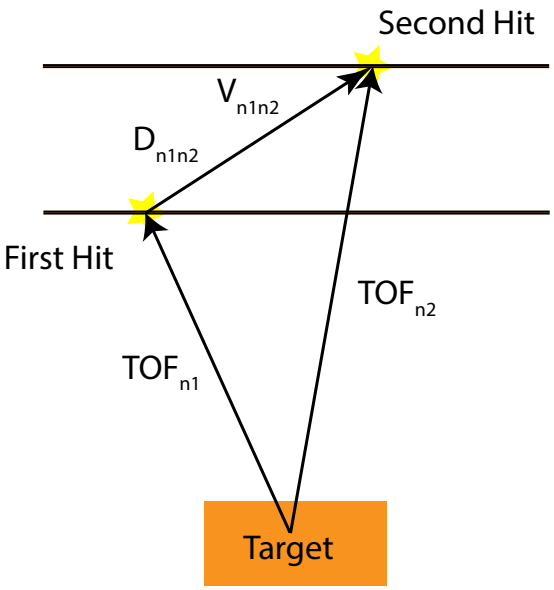

Figure 5.20: Schematic of a 2-neutron event.

Table 5.4: Parameters used for causality gates

Beam	A [cm/ns]	B [cm]
^{13}B	14	30
^{11}Li	11	30

significantly reduced by applying causality cuts. This technique assumes that two hits in the detector arrays are caused by the same neutron. Then, a hypothetical velocity for the neutron from the first interaction to the second interaction can be calculated as

$$V_{n1n2} = \frac{D_{n1n2}}{TOF_{n2} - TOF_{n1}} \tag{5.14}$$

where TOF_{n1} and TOF_{n1} are corrected TOFs measured by MoNA-LISA, and D_{n1n2} is the distance between the two hits, as illustrated in Fig. 5.20. If the event is a false 2-neutron event, V_{n1n2} tends to be smaller than the beam velocity, and it's more likely that D_{n1n2} is small. Therefore, causality cuts require

$$\begin{aligned} V_{n1n2} &> A \\ D_{n1n2} &> B \end{aligned} \tag{5.15}$$

where A and B are causality parameters. A is usually chosen as the high limit of the beam velocity, and B is usually the distance between a few adjecent MoNA-LISA bars. The actual values used in the current analysis are listed in Table 5.4.

Causality cuts have previously been applied to extract three-body decay energy spectra in other two-neutron unbound systems [23, 63, 64, 65, 66]. The two-neutron detection efficiencies with and without causality cuts are shown in Fig. 5.21.

The gated efficiency drops near 0 MeV because the kinematics required by causality cuts

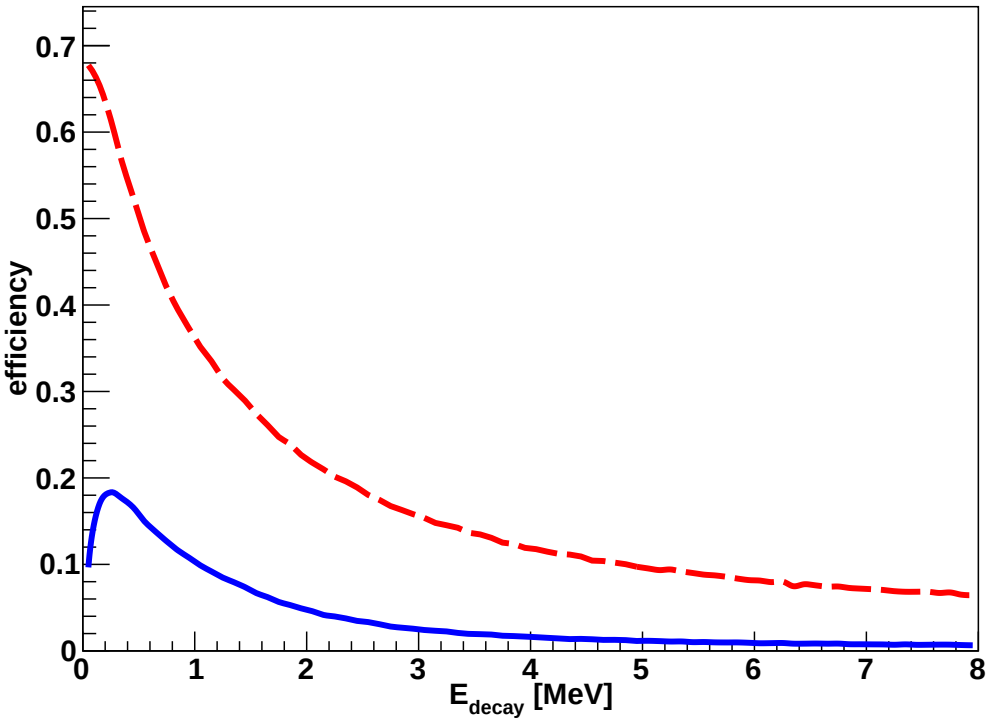

Figure 5.21: 2-neutron efficiency (dashed red) and gated 2-neutron efficiency (solid blue). A simulation with phase space decay model and realistic beam parameters for ^{11}Li beam was used for estimating these efficiencies.

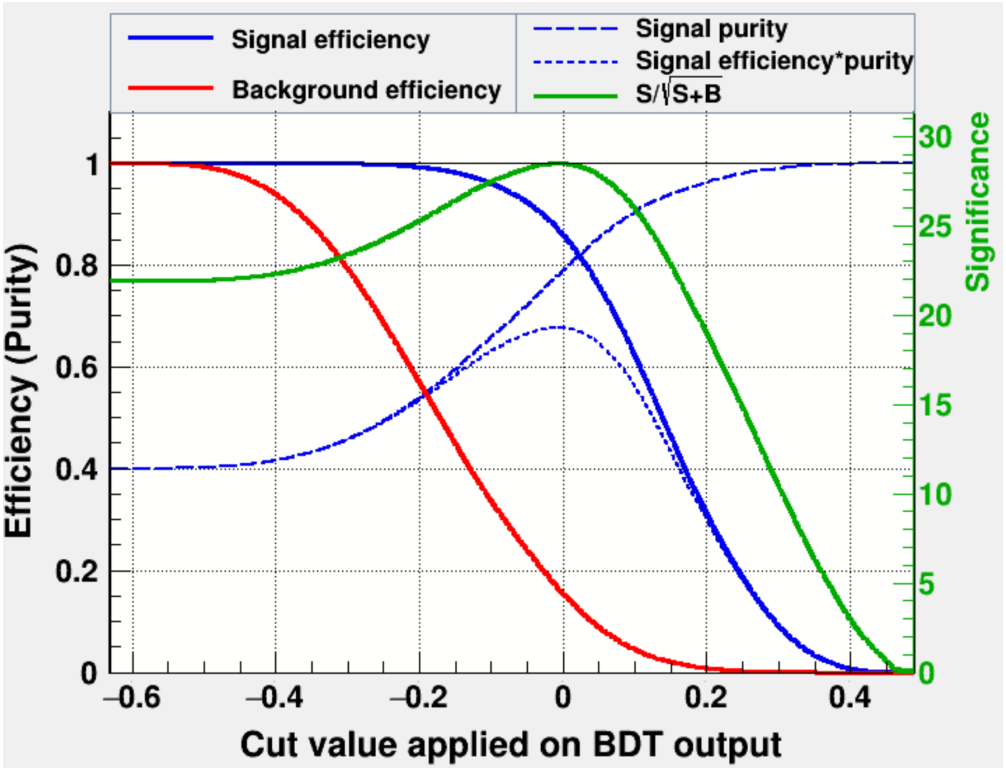

Figure 5.22: Cut efficiencies estimated from simulated ^{11}Li beam data.

reject more events at low energy. However, the efficiency still has a finite value at zero decay energy.

5.3.2 Machine Learning Methods

The classification of 2-neutron events was also attempted using machine learning. This approach was accomplished with TMVA (Toolkit for Multivariate Data Analysis) [67] built-in to the data analysis framework ROOT [68]. For this approach, several variables in simulated data were used first to train and test a classifier. Then, the classifier was used to evaluate experimental data, based on the corresponding variables. A probability for each event to be a false 2-neutron event can be estimated from the classifier. A detailed description is provided in Appendix A.

Machine learning methods show the potential to achieve higher efficiency of the true 2-neutron event selection, compared to causality cuts. For the ^{11}Li beam data, causality cuts return a signal purity = 0.78 and a signal efficiency = 0.49. For the same purity, the boosted decision trees achieve a signal efficiency = 0.87, as shown in Fig. 5.22, increasing the signal efficiency by 78%. However, machine learning methods also add complexity to analysis, since simulations must be performed first for training a classifier, and the dependence of the classifier distribution on simulation parameters. To avoid complexity and to be consistent with the previous analysis, the rest of the analysis was performed with causality cuts.

5.4 Reconstruction

5.4.1 Neutron 4-Momentum Reconstruction

Neutron 4-momenta, as well as fragment 4-momenta, were reconstructed in the lab frame in the current work. The magnitude of the neutron velocity is

$$v_n = \frac{|\vec{D}|}{TOF_{\text{corr}}} \tag{5.16}$$

where TOF_{corr} is the corrected neutron TOF and $\vec{D}$ is the vector from the reaction target to a neutron interaction in MoNA-LISA as $\vec{D}$. Then, the Lorentz factor, the momentum, and the energy are calculated according to relativistic mechanics.

5.4.2 Fragment 4-Momentum Reconstruction

The fragment 4-momenta to be reconstructed are the momenta at the reaction target, where the unbound nuclei decayed. However, the CRDCs measure the fragment positions and

angles after the Sweeper magnet. Therefore, the fragments need to be tracked back to the target. This was achieved by the ion-optics program COSY INFINITY (referred as COSY hereafter) [69].

To use COSY, a magnetic field map was generated using IGOR_PRO [70] first, based on previous Hall probe measurements and the current of the Sweeper magnet. Then, the magnetic field map is used as an input to COSY, which generates an ion-optical matrix M relating the beam parameters at the target to the parameters at CRDC1

$$\begin{bmatrix} x^{CRDC1} \\ \theta_x^{CRDC1} \\ y^{CRDC1} \\ \theta_y^{CRDC1} \\ L \end{bmatrix} = M \begin{bmatrix} x^{\text{target}} \\ \theta_x^{\text{target}} \\ y^{\text{target}} \\ \theta_y^{\text{target}} \\ \delta_E \end{bmatrix} \tag{5.17}$$

where x and y stand for positions, θ stands for corresponding angles, CRDC1 or target represents the location of the coordinates, L is the tracking length, and δ_E is defined by

$$K.E._{\text{frag}} = E_{\text{ref}}(1 + \delta_E) \tag{5.18}$$

where $K.E._{frag}$ is the kinetic energy of the fragment and E_{ref} is the reference energy determined by the rigidity of the field map.

This matrix uses target information as the input, but since the coordinates are measured

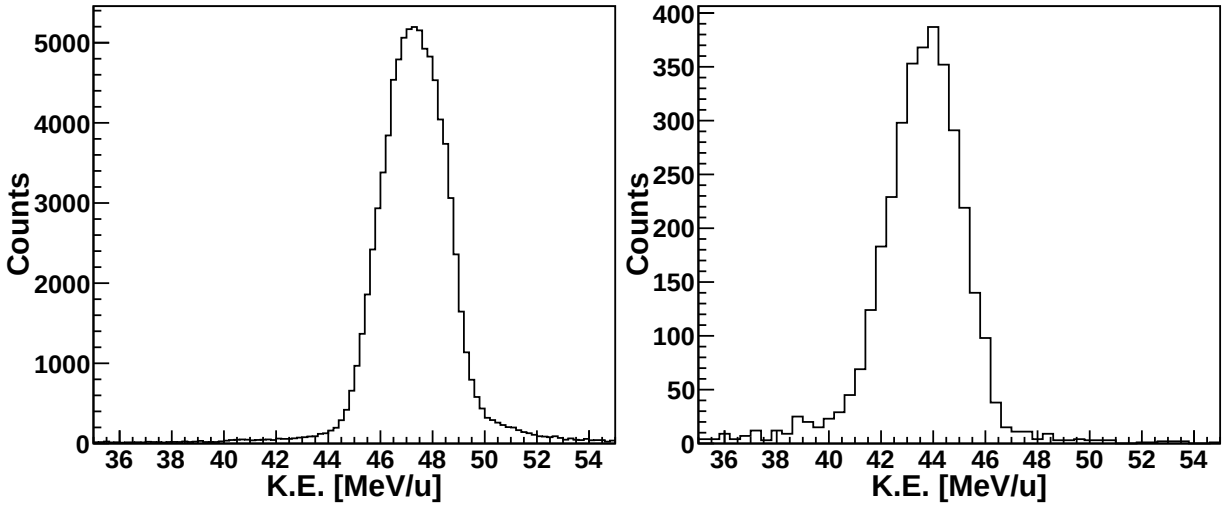

Figure 5.23: Reconstructed kinetic energy for ^{13}B (left) and ^{11}Li (right) beam using beam down center runs. Expected beam energies (47 MeV/u and 44 MeV/u, respectively) are well-reproduced.

at CRDC1 a transformed matrix M' [69] has to be used such that

$$\begin{bmatrix} \theta_x^{target} \\ y^{target} \\ \theta_y^{target} \\ \delta_E \\ L \end{bmatrix} = M' \begin{bmatrix} x^{CRDC1} \\ \theta_x^{CRDC1} \\ y^{CRDC1} \\ \theta_y^{CRDC1} \\ x^{\text{target}} \end{bmatrix}; \tag{5.19}$$

x^{target} was not measured, however, a constant representing the x centroid of the beam can be substituted for a measured value. Reconstructed beam kinetic energies are shown in Fig. 5.23 for verification.

The relation between the kinetic energy and the Lorentz factor is:

$$K.E._{\text{frag}} = M_f(\gamma_f - 1) \tag{5.20}$$

where M_f is the mass of the fragment, γ_f is the Lorentz factor of the fragment. Using angles at the target, the fragment 4-momenta can be reconstructed similarly according to relativistic mechanics in the previous section.

5.4.3 Decay Energy Reconstruction

Using the 4-momenta of the fragments and neutrons, the decay energy of the unbound system can be reconstructed according to Equation 4.7 in Section 4.3. Explicitly, the two-body decay energy of ^{8}He + n is

$$E_{decay} = \sqrt{m_f^2 + m_n^2 + 2(E_f E_n - \vec{p_f} \cdot \vec{p_n})} - m_f - m_n \tag{5.21}$$

where f stands for the ^{8}He fragment. The three-body decay energy of ^{8}He + 2n decay is

$$E_{decay} = \sqrt{m_f^2 + 2m_n^2 + 2T} - m_f - 2m_n. \tag{5.22}$$

Hhere T is written as:

$$T = E_f E_{n1} + E_f E_{n2} + E_{n1} E_{n2} - \vec{p_f} \cdot \vec{p}_{n1} - \vec{p_f} \cdot \vec{p}_{n2} - \vec{p}_{n1} \cdot \vec{p}_{n2} \tag{5.23}$$

where n1 and n2 stands for the two neutrons. The three-body and two-body decay energy spectra from the two beams are shown in Fig. 5.24 and Fig. 5.25.

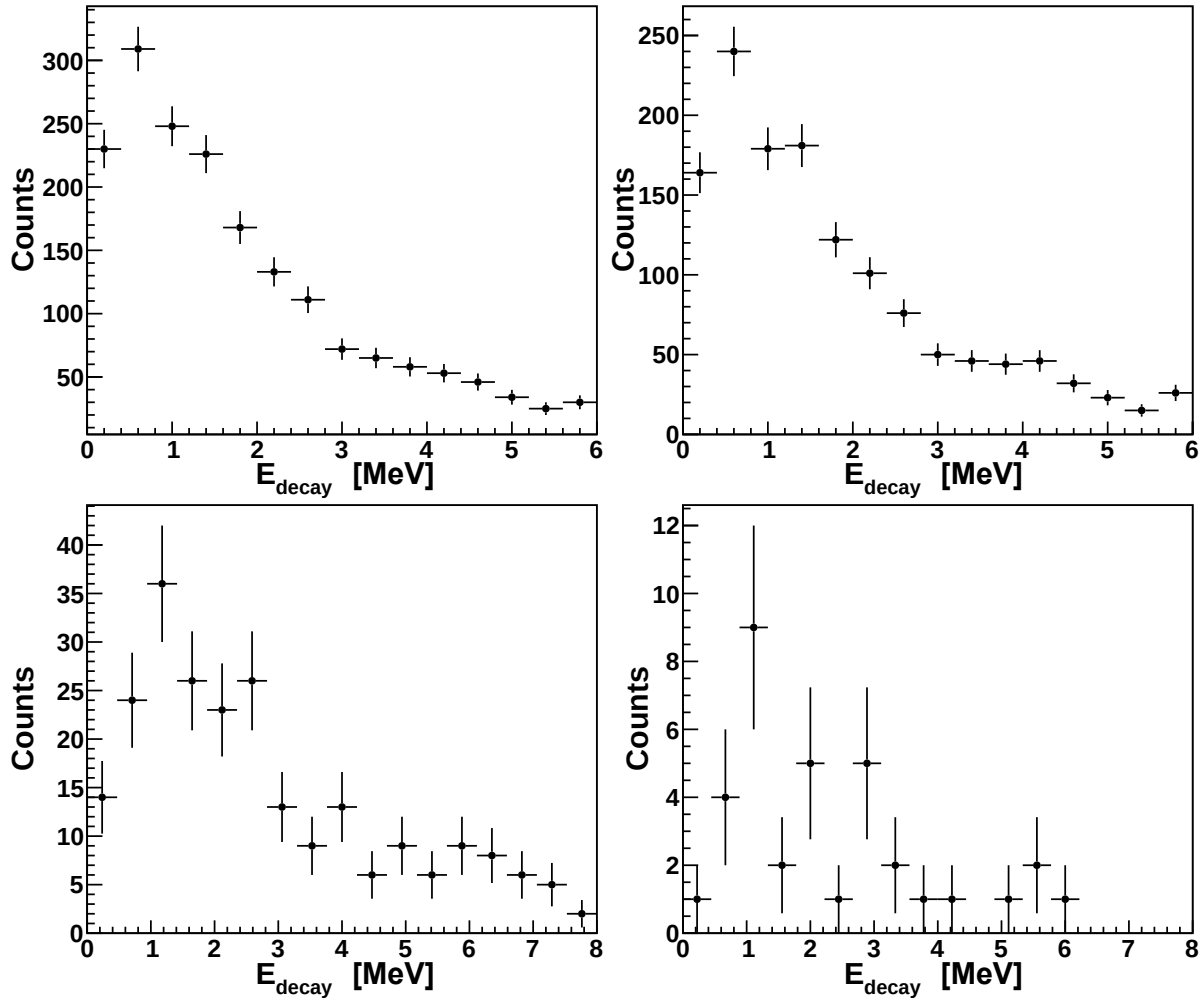

Figure 5.24: Decay energy spectra from the ^{13}B beam. The upper left shows the ^{8}He + n two-body decay energy. The upper right shows the ^{8}He + n two-body decay energy with a neutron multiplicity=1 gate. The lower left shows ^{8}He + 2n three-body decay energy. The lower right shows causality-gated ^{8}He + 2n three-body decay energy.

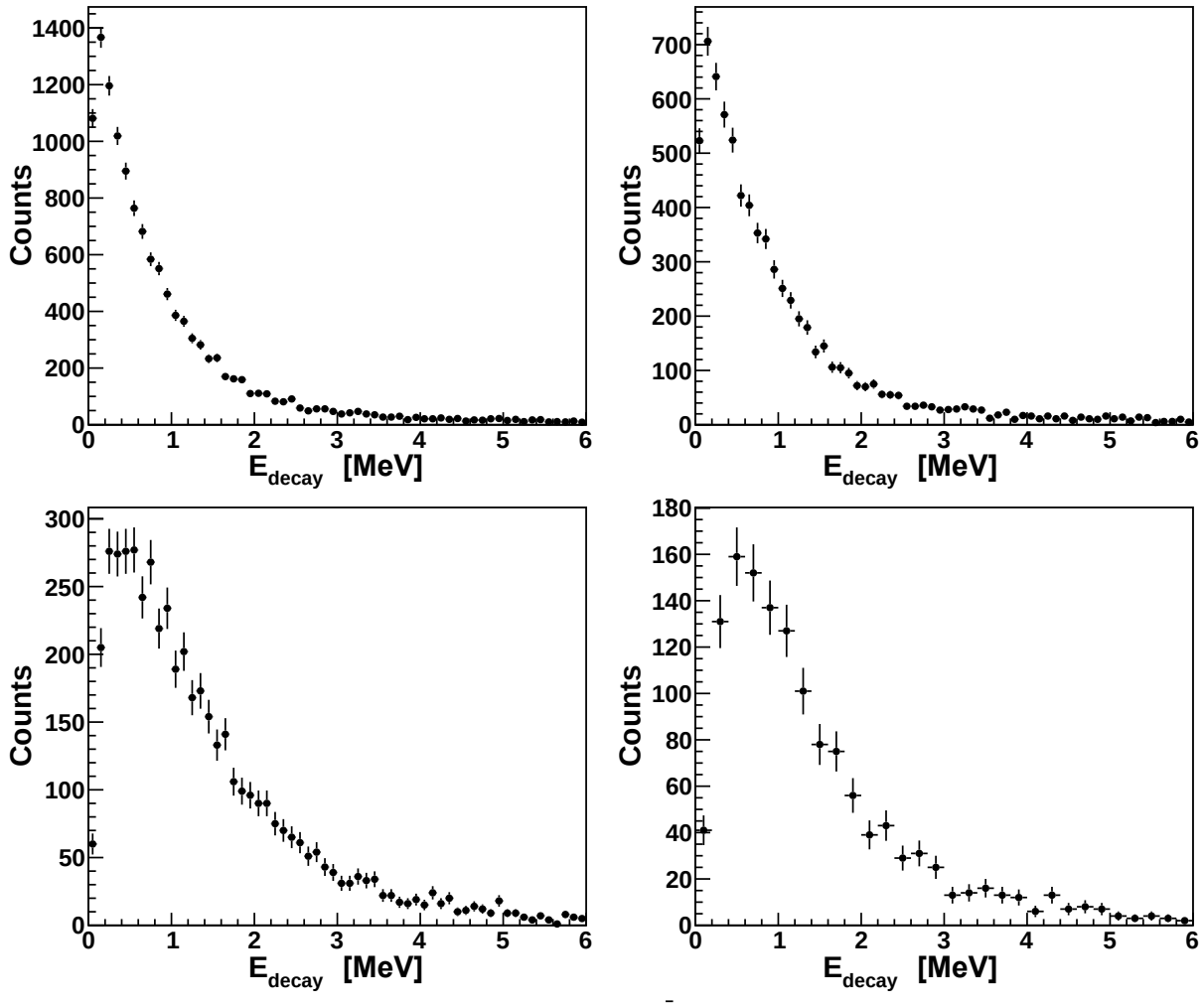

Figure 5.25: Decay energy spectra from the ^{11}Li beam. The left-upper shows the ^{8}He + n two-body decay energy. The upper left shows the ^{8}He + n two-body decay energy. The upper right shows the ^{8}He + n two-body decay energy with a neutron multiplicity=1 gate. The lower left shows ^{8}He + 2n three-body decay energy. The lower right shows causality-gated ^{8}He + 2n three-body decay energy.

5.5 Simulations

Monte Carlo simulations including theoretical decay energy distributions, decay modes, reaction mechanisms, beam parameters, magnetic fields, as well as detector acceptances, efficiencies, and resolutions were performed for comparison with data. The same simulation program has been used for many previous experiments, and the details and verification of this program were thoroughly discussed in Refs. [60, 57, 56]. Thus, this section only briefly describes the results of the simulations of ^{10}He.

The simulation starts by creating the beam particles at the surface of the target. The positions and angles of the beam are modeled by Gaussian distributions. The parameters were extracted from the CRDC position and angle measurements of a beam down center run, using the transformation matrix

$$\begin{bmatrix} \theta_x^{\text{target}} \\ y^{\text{target}} \\ \theta_y^{\text{target}} \\ x^{\text{target}} \\ \\ L \end{bmatrix} = M'' \begin{bmatrix} x^{CRDC1} \\ \theta_x^{CRDC1} \\ y^{CRDC1} \\ \theta_y^{CRDC1} \\ \\ \delta_E \end{bmatrix}, \tag{5.24}$$

where δ_E was calculated from the beam energy.

Once created, the beam particles are drifted to reaction positions, which were randomly chosen throughout the thickness of the target. Energy loss and straggling are applied before the reaction. The reaction is treated in two steps. First, nucleons are removed from the beam particle to form ^{10}He, while the kinetic energy per nucleon is kept the same. Then, a parallel momentum kick based on the work of Goldhaber [71] and a transverse momentum kick based

on the work of Bibber [72] are added to the ^{10}He. The ^{10}He then decays according to a line shape described in Section 3.2. The energies and momenta of the three decay products (^{8}He + n + n) are determined by the phase space decay model (TGenPhaseSpace [40] in ROOT).

The charged reaction fragments are drifted to the back of the target, taking into account the energy loss and straggling. Then, a forward COSY matrix transports the fragments from the target to CRDC1. A free drift is applied between CRDC1 and CRDC2. Positions of the fragments at CRDC1 and CRDC2 were folded with Gaussian resolutions to simulate the detector response. Combining with angles calculated from these folded positions, a fragment trajectory through the Sweeper is determined as discussed in Section 5.4.2. A comparison of simulated fragments to data is shown in Fig. 5.26 where the measured positions, measured angles, and tracked angles are plotted. It should be mentioned that, for the data, the measured Y angles, and tracked X and Y angles are narrower. However, they have minor effects on decay energy spectra.

Neutrons from the decays are handled by GEANT4 [73, 74] using the neutron physics package MENATE_R [75]. The Sweeper chamber is modeled as steel to simulate the geometric cut on the neutrons. For the neutrons that interact with MoNA-LISA, the deposited energy is converted to light output. The light propagates to the two ends of the detector bar according to Birks' law [76]. An event is recorded only if both of the ends receive a light signal greater than 0.91 MeVee. This is used to simulate the software light threshold described in Section 5.1.4.1. Gaussian distributions were added to the neutron X position and the neutron TOF to account for the detector resolutions.

The neutron 4-momentum reconstruction, fragment 4-momentum reconstruction, and decay energy reconstruction were performed for data and simulated events in the same way. The same gates were used as causality cuts. By treating simulations and data the same way,

spectra from simulations could be used to fit data, and the parameters of the theoretical line shape for ^{10}He could be extracted.

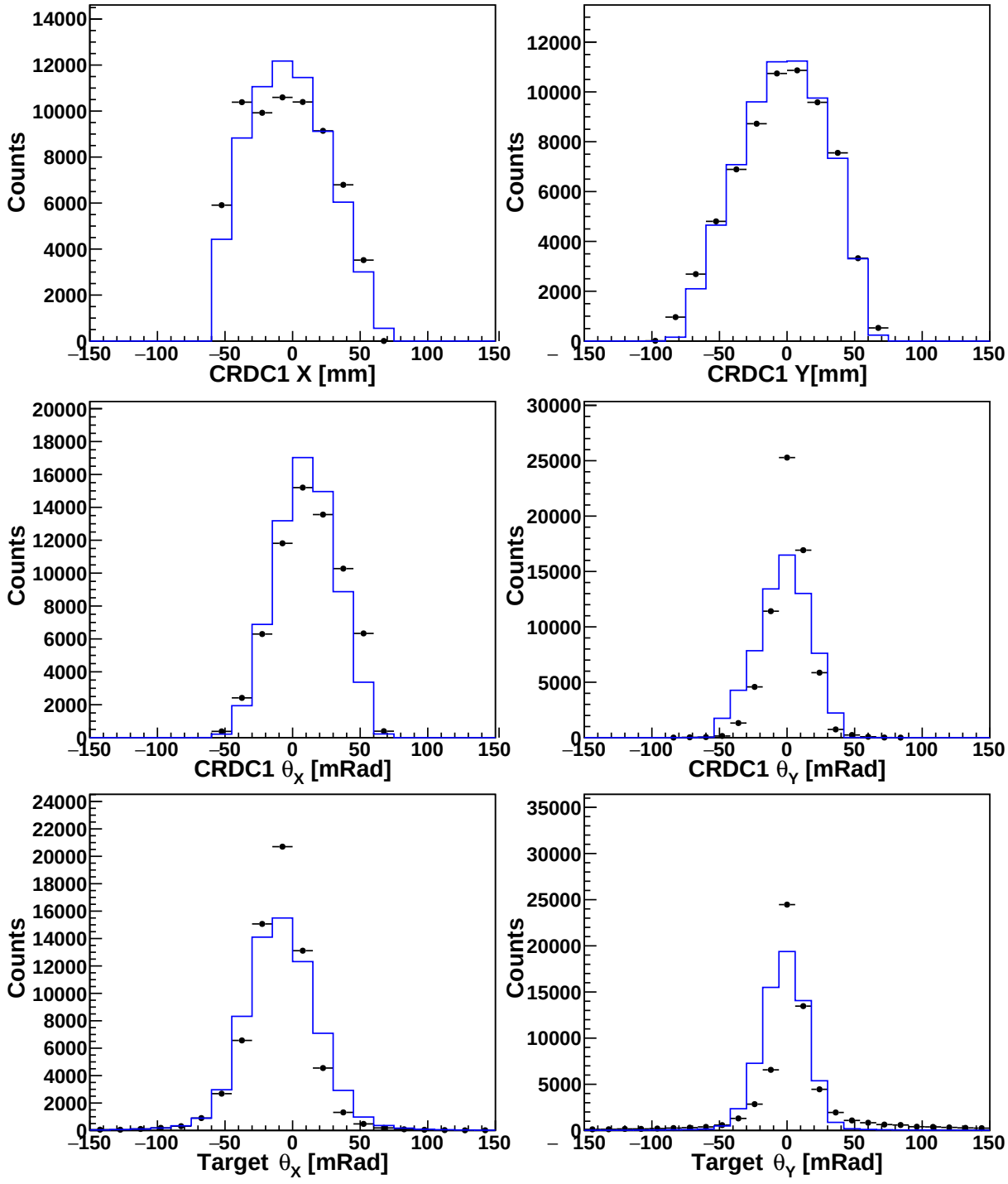

Figure 5.26: Comparison of simulated fragment to data for ^{8}He from the ^{11}Li beam.

Chapter 6

Results and Discussion

6.1 ^{13}B beam

Fig. 6.1 shows the measured and simulated decay energy spectra from the ^{13}B beam. The ^{8}He + n two-body decay energy is broad, and there are no prominent structures at higher decay energies. In the ungated three-body decay energy, a peak seems appear at around 1 MeV. However, with the causality cuts are applied, the greatly reduced statistics do not show any peaks. The highest bin at about 0.8 MeV in the gated spectrum cannot be a narrow resonance since it is narrower than the resolution. This 9-count spike may be caused by statistical fluctuations.

The simulations consist of four components. A state at 1.6 MeV from Ref. [23] is used as the ground state of ^{10}He, and a 1.0 MeV p-state and a 3.0 MeV d-state are used for simulating resonant states in ^{9}He. The resonance energies and widths come from an experiment performed in the same experimental area, the analysis of which is still in progress. A Maxwellian distribution with temperature 4.5 MeV was used as a phenomenological description for the de-excitation from high-lying ^{9}He continuum.

Although 1.6 MeV was used as the resonance energy of the ^{10}He ground state in Fig. 6.1, changing it to 2.1 MeV (which was extracted from a ^{3}H(^{8}He,p)^{10}He transfer experiment [21]) results equally good fit. This is understandable since the causality-gated spectrum has

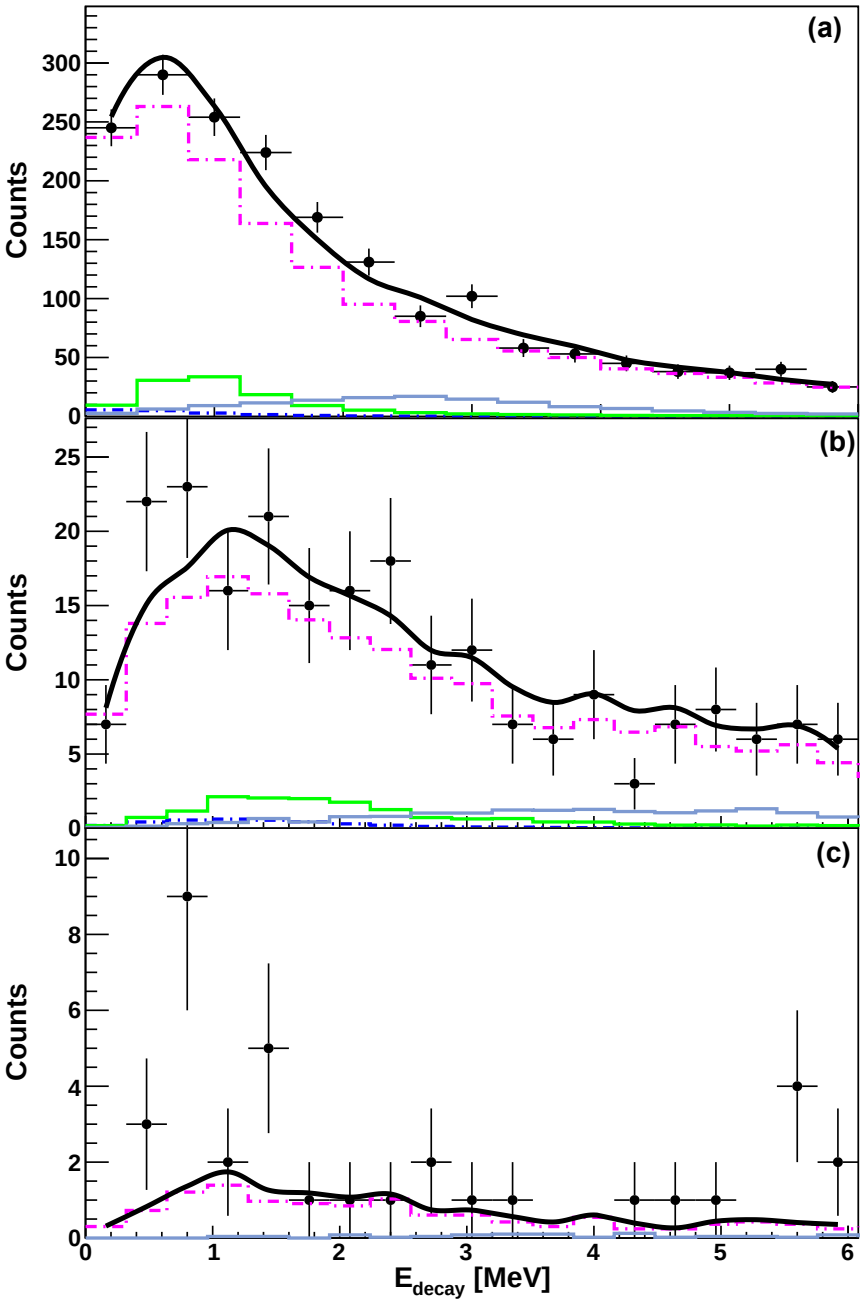

Figure 6.1: (a) Two-body decay energy spectrum. (b) Ungated three-body decay energy spectrum. (c) Decay energy spectrum gated on causality cuts. Data are presented as crosses and solid circles. The black solid line shows the sum of simulations. The purple dot-dash line is the thermal background. The p-state and d-state in ^{9}He are shown as the green solid and dark blue solid lines, respectively. The light blue dot-dash line shows the state in ^{10}He.

low statistics, so the fit is not sensitive to the states in ^{10}He which decay by emitting two neutrons. Therefore, results from the compact ^{13}B beam cannot resolve the two ^{10}He ground state energies extracted from reactions of different types.

In knockout reactions, the cross sections for populating the ground state of final nucleus decreases with the number of removed nucleons. However, the fit in Fig. 6.1 indicates the population of ^{10}He is significantly weaker than that of ^{9}He. This suggests that the population of ^{9}He contains contributions other than direct knock-out. Simple combinatorics can be used to estimate the relative populations of ^{9}He and ^{10}He. Assume multi-nucleon removal reactions only remove nucleons above the s-shell (i.e., on top of the α core), and the possibility of removing each nucleon is the same. Then, 3 protons and 6 neutrons can be removed from ^{13}B. Given a 3-nucleon removal reaction, the probability of populating ^{10}He from ^{13}B beam (^{13}B($-$3p)^{10}He) is $\binom{3}{3}/\binom{9}{3} = 1.2\%$. On the other hand, given a 4-nucleon removal reaction, the probability of populating ^{9}He (^{13}B($-$3p1n)^{9}He) is $\binom{3}{3} \times \binom{6}{1}/\binom{9}{4} = 4.8\%$. Also, one might calculate the probability of ^{8}He direct population (^{13}B($-$3p2n)^{8}He) is 11.9%. Those simple estimations indicate that the spectrum of ^{8}He in coincidence with neutrons is dominated by the decay of ^{9}He.

More insights can be gathered from studying the components of the ^{9}He contribution. Even though ^{9}He resonant states extracted from another experiment fit data, the non-resonant thermal background accounts for 90% of the observed spectrum. This suggests that the 3p1n-removal reaction is dispersive and excites ^{9}He to the high-lying continuum. Therefore, the 3-proton knockout reaction is not ideal for investigating 2-neutron decays since the spectrum is dominated by the 1-neutron decay competition, and the 2-neutron information will be usually embedded in the 1-neutron thermal background. In addition, the ^{8}He direct population channel discussed above also contributes to the background. For

these reasons, the current experiment cannot resolve the ground state of ^{10}He using a compact ^{13}B beam. Even increasing the measurement time to improve the statistics might not be sufficient to extract the ^{10}He resonance parameters. These factors should be taken into consideration in the design of future experiments.

6.2 ^{11}Li Beam

Fig 6.2 shows the measured and simulated decay energy spectra from the ^{11}Li beam. All measured spectra from the ^{11}Li beam are significantly narrower than the spectra from the ^{13}B beam. The measured three-body decay energy spectrum with the causality gates shows that a large number of counts survived the cuts, suggesting substantial 2n contributions. In fact, the best fit to data contains only one component, which is the ^{10}He correlated background described in Section 3.2.3. The ^{11}Li binding energy E_b = 369 keV [77] is used for the correlated background calculation. The observation of a dominant correlated background means that the observed ^{10}He spectra are heavily influenced by the initial state.

In contrast to the result from the ^{13}B beam, ^{9}He contributions are not observed in the ^{11}Li data. Usually, the 1p1n-removal is expected in addition to the 1p-removal. However, the absence of ^{9}He can be understood from the structure of ^{11}Li beam. For population of ^{9}He, a ^{11}Li($-$1p1n) reaction is necessary. Knocking out a neutron and a proton from the ^{9}Li core is more plausible than knocking out a proton from the core and a neutron from the halo. The former leads to a neutron hole state in ^{9}He since neutrons in the core are deeply-bound compared to the valence neutrons in the halo. Since the two-neutron separation energy of ^{8}He is only 2.1 MeV [77], it possible the high-lying neutron hole state in ^{9}He directly decays to ^{6}He + 3n. Therefore, ^{9}He contributions are not significant in the coincidence spectra of

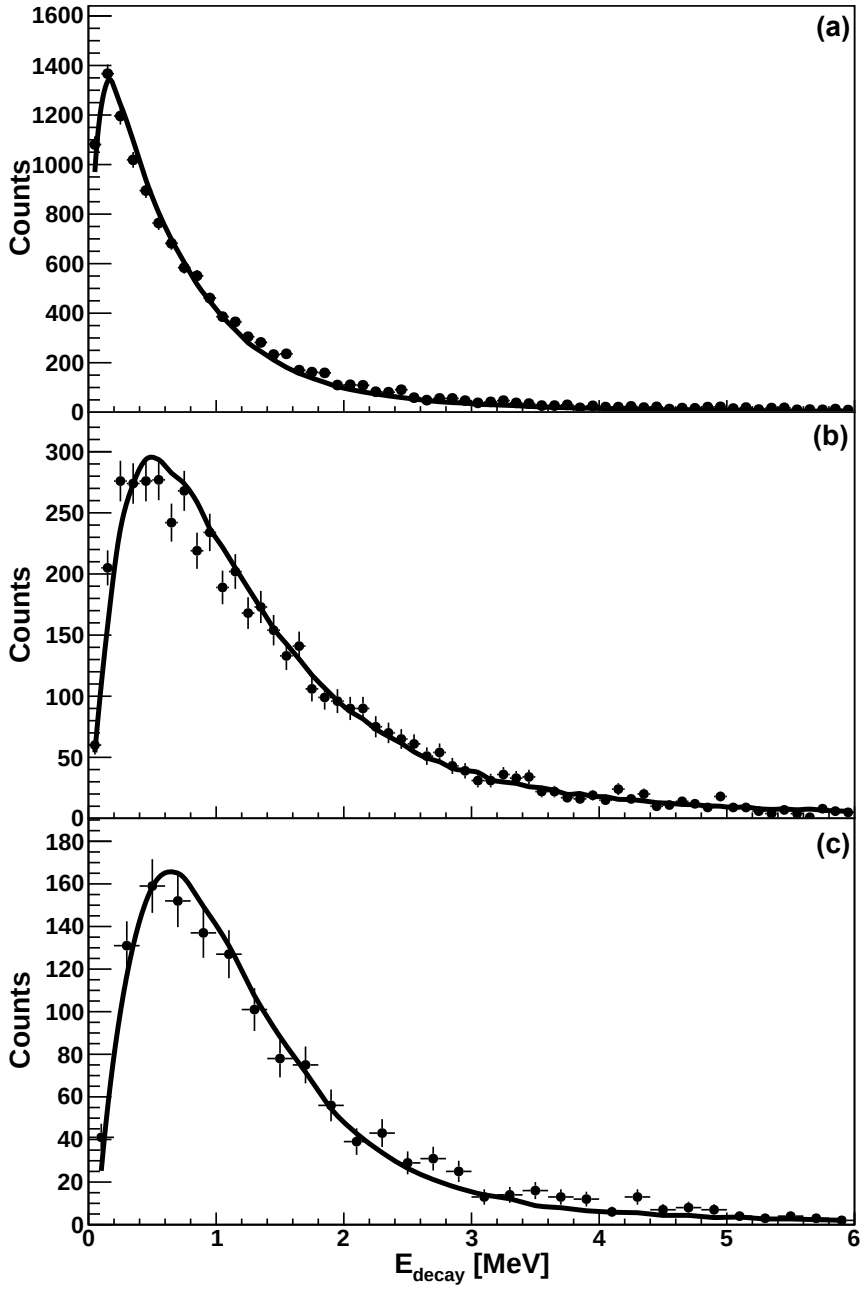

Figure 6.2: (a) Two-body decay energy spectrum. (b) Ungated three-body decay energy spectrum. (c) Decay energy spectrum gated on causality cuts. Data are presented as crosses and solid circles. The black line shows the simulation of the correlated background model.

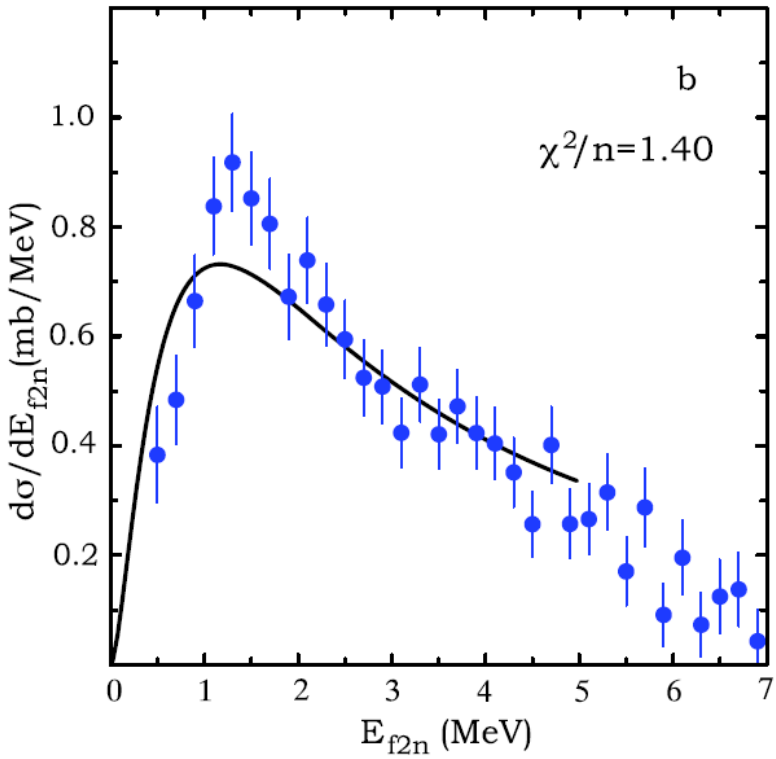

Figure 6.3: Invariant mass spectrum for ^{10}He from Ref. [16]. The data are presented as blue solid circles. The correlated background is shown as black solid lines.

^{8}He fragments.

Simulations of resonances and/or a thermal background in ^{10}He were fit to data, but they resulted in unphysically large width and poor χ^2 values. Fitting with a ^{10}He resonant state with a correlated background was also attempted. However, the scale factor of any resonant state added was optimized to 0 by the χ^2 minimization procedure. This was in contrast with the similar GSI experiment for which a ^{11}Li beam was used [16], where a resonant state could be fit on top of the correlated background, even though in a follow-up paper the authors concluded that their data should be interpreted as a 1.54 MeV ground state plus a 3.99 MeV excited state [17], instead of a 1.42 MeV ground state plus a correlated background. Sharov, Egorova and Grigorenko later argued that these conclusions were not

valid from the point of view of full reaction dynamics [39]. Still, there are inherent differences between the GSI and the current ^{11}Li beam experiments, since the correlated background that fits the current data did not fit GSI experiment, as shown in Fig. 6.3. Besides why the ^{3}H(^{8}He,p)^{10}He transfer experiments observed different ground state energies of ^{10}He than all other experiments, there is one more interesting question to be answered: why the current experiment observed different line shapes although the same ^{11}Li beam was used.

Although the χ^2 minimization optimized the contribution of the ^{10}He resonant state to 0, considering the resolutions of the experiment setup, resonant contributions can account for up to 10% of the ^{10}He spectra without significantly reducing the quality of the fit, as shown in Fig. 6.4. This indicates that some resonant contributions cannot be ruled out, however, not as dominant as in the GSI experiment.

This discrepancy might be explained with the the difference in time scales, since Zhukov and Grigorenko's theory predicts that the "shift" of the resonance energy is a consequence of the large size of the ^{11}Li halo and the short lifetimes of neutron-unbound states. The GSI experiment ran at 280 MeV/u whereas the current experiment at 44 MeV/u, therefore, the timescale for the target and the beam particles being in contact with each other was shorter for GSI than for the current experiment. Simply estimations can be made by dividing the sum of the diameters by the beam velocities: the contact time is 1.0×10^{-22} s for the GSI experiment and 2.5×10^{-22} s for the current experiment. The extracted width from the GSI experiment was 1.91 MeV [17] which would corresponds to a halflife of 2.4×10^{-22}. While the contact time in the GSI experiment is significantly shorter, the contact time in the present experiment is about the same. Thus, there was not sufficient time to form ^{10}He and the decay might be still influenced by the structure of the initial ^{11}Li halo state.

However, as summarized by Table 6.1, there were ^{11}Li beam experiments ran at lower

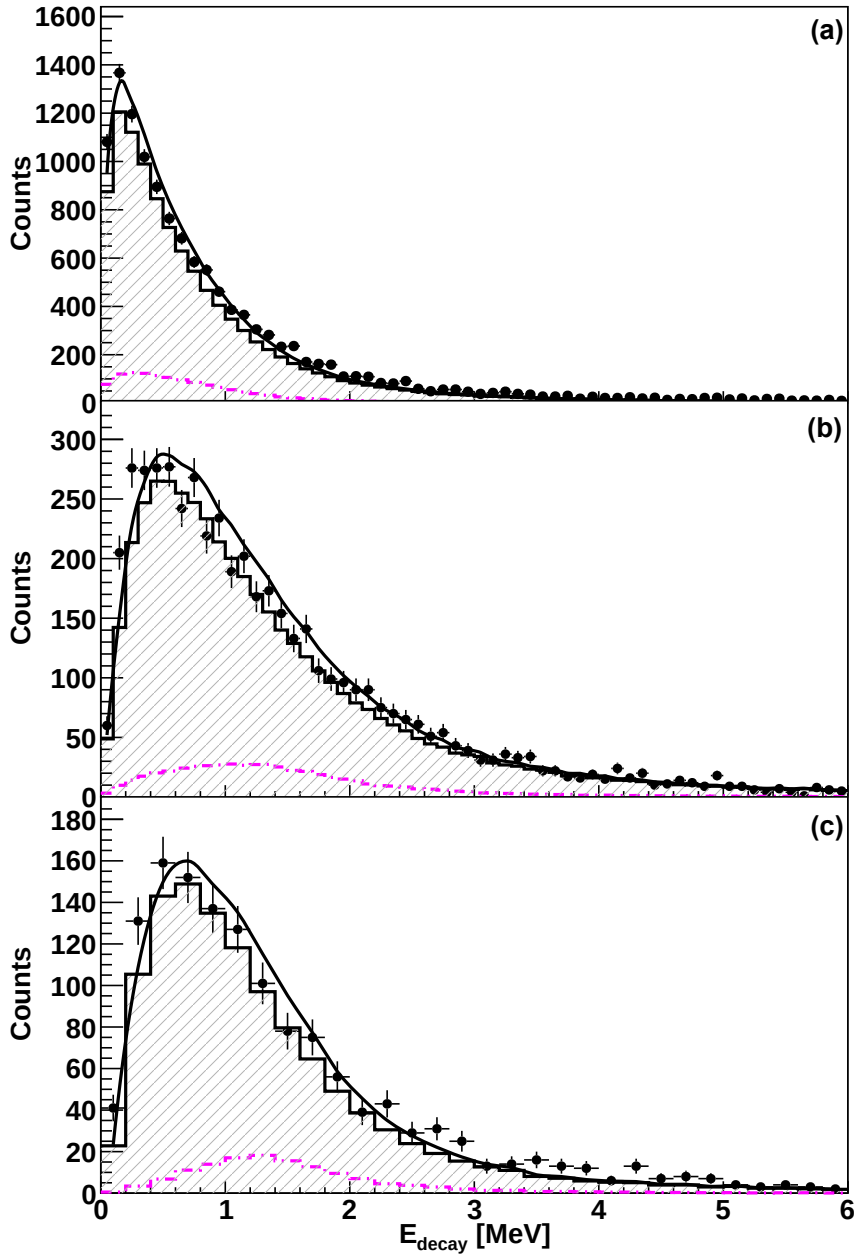

Figure 6.4: (a) Two-body decay energy spectrum. (b) Ungated three-body decay energy spectrum. (c) Decay energy spectrum gated on causality cuts. Data are presented as crosses and solid circles. The shaded area shows the simulation of the correlated background model. The purple dot-dash line represents the resonant state at 1.6 MeV. The resonant contribution is fixed at 10%.

Table 6.1: Summary of ^{10}He experiments with halo beams.

Reaction	Target	E_{beam}	$E_{g.s.}$	Reference
^{11}Li(-p)	^{2}H	61 MeV/u	1.2(3) MeV	[14]
^{11}Li(p,2p)	^{1}H	84 MeV/u	1.7(6) MeV	[15]
^{11}Li(-p)	^{1}H	280 MeV/u	1.54(10) MeV	[17]
^{14}Be(-2p2n)	^{2}H	59 MeV/u	1.60(25) MeV	[23]
^{2}H(^{11}Li,^{3}He)	^{2}H	50 MeV/u	1.4(3) MeV	[24]
^{11}Li(-p)	^{9}Be	44 MeV/u	N.A.	current

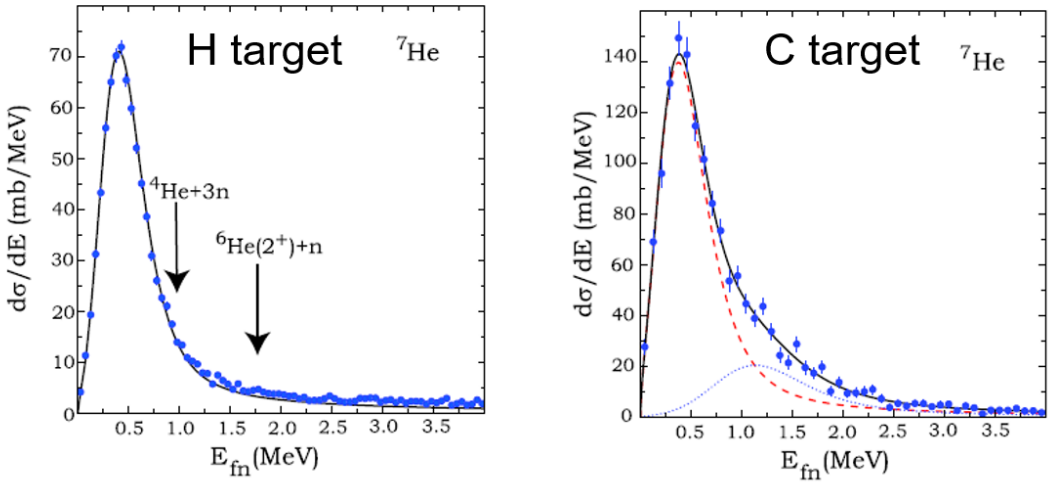

Figure 6.5: Decay energy spectra of ^{7}He from the H target (left) and the C target (right) from Ref. [78].

energies, which were closer to the current one. Those experiments also reported resonant states even without a correlated background, so this contradicts the timescale argument. Table 6.1 nevertheless shows one crucial difference and feature of the current experiment: it was the only experiment that used a heavy ion target.

Indeed target dependence has been observed between hydrogen and heavy ion targets used for the population of unbound nuclei. Aksyutina et al. [78] showed the target dependence of ^{7}He populated from the ^{8}He beams. The measured decay energy spectra are different for the H target and for C target, as shown in Fig. 6.5. The line shape of the well-known ^{7}He deviated

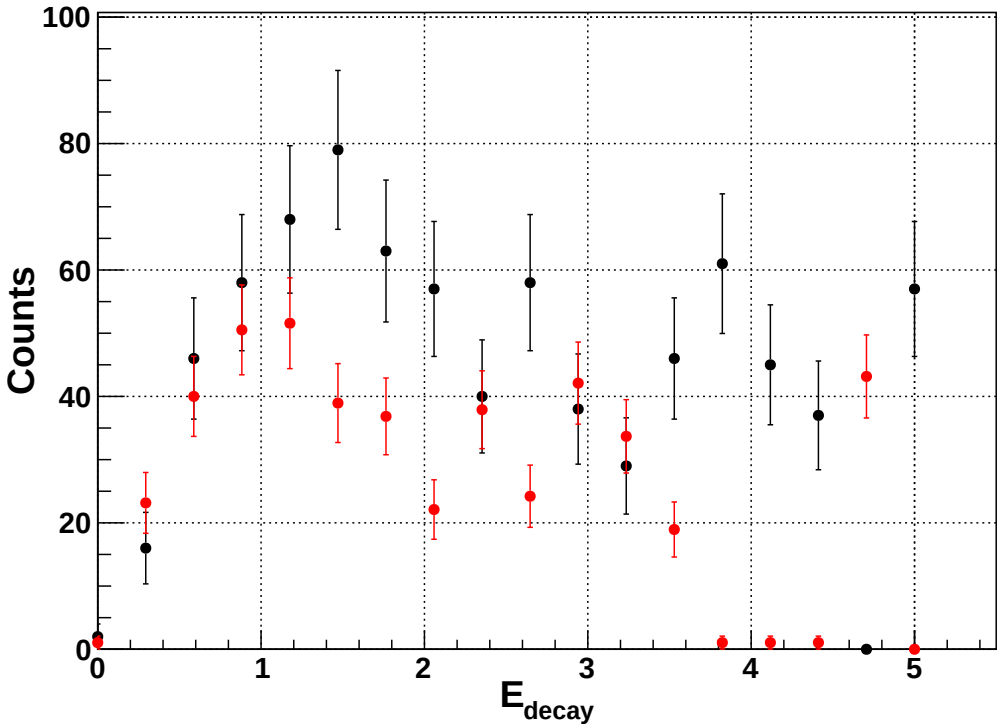

Figure 6.6: Decay energy spectra on the C target (red) and the D target (black) for the first observation in ^{10}He. The D target spectrum is digitized from Ref. [14]. The C target spectrum is deduced from the CD_2 and the D target spectra in Ref. [14], with estimated statistical error bars.

from the Breit-Wigner distribution when a carbon target was used at relativistic energy. The authors attributed this effect to target-dependent re-scattering, and the destruction of the carbon nucleus. The first observation of the resonance in ^{10}He also used two different targets: CD_2 and C [14]. The comparison of the ^{10}He spectra on the Deutron nucleus and on the C nucleus is shown in Fig. 6.6. It can be seen that the C target spectrum is shifted to lower energies compared to the D target spectrum, which agrees with the current experiment. Note ^{8}He is also a halo nucleus and the width of the ^{7}He ground state is 125 keV [77] which is smaller than ^{10}He roughly by a factor of 10, meaning the lifetime of ^{7}He is 10 times longer. Both of the two cases of target dependence might be related to timescales. For heavier targets, short lifetimes and smaller beam energies (which means longer contact time) result in a larger distortion in the measured decay energy spectra. However, it's not yet clear why there is target-dependence.

In principle, the correlated background corresponds to a 0^+ configuration of the ^{8}He + n + n three-body system. There are theoretical calculations predicting an s-wave 0^+ resonant state at low energies. Aoyama predicted a three-body s-wave 0^+ state at 50 keV using analytic continuation in the coupling constant method and complex scaling method [29, 30, 31]. He claimed that the state was not observed so far without indicating why. Fossez et al. made the first many-body prediction that the ^{10}He ground state is a double-halo 0^+ very close to the 2n threshold with almost pure s-wave valence neutrons [33]. It is understandable that such a state is hard to populate from a ^{11}Li beam since the inner halo does not exist in the ^{9}Li core. However, the very low-lying narrow 0^+ was still not observed from ^{3}H(^{8}He,p)^{10}He transfer experiments, even if the inner halo was provided by ^{8}He beam. Therefore, the existence of a very low-lying s-wave resonant state is questionable.

Alternatively, Grigorenko and Zhukov predicted a three-body virtual state might exist

in ^{10}He with s-wave valence neutrons if ^{11}Li beams were used [22]. They predicted that a three-body virtual state corresponds to a sharp increase in the decay line shape near zero decay energy. Their quantitative results also disagrees with the current observation.

Chapter 7

Summary and Outlook

In this work, ^{10}He was studied using a 44 MeV/u halo ^{11}Li beam and a 47 MeV/u non-halo ^{13}B beam at the NSCL. Neutrons were measured by MoNA-LISA; charged particles were measured by the Sweeper detectors; and the decay energies were reconstructed using invariant mass spectroscopy. Monte Carlo simulations were performed to compare theoretical models to experimental data. Energies of resonant states in ^{10}He could not be extracted from the ^{13}B beam due to low statistics and competition from the population of ^{9}He. The ^{11}Li beam data could be described with the correlated background model, implying the initial state has a significant influence on the measured spectra. Interpretations of decay energy spectra should be made with extra caution if the expected widths are greater than 1 MeV and halo beams are involved. In addition, an apparent target dependence was observed from the ^{11}Li beam.

Since resonant states are not resolved from the ^{13}B(-3p) reaction, the question of the ^{10}He ground state is not solved yet. Experiments using different reactions are encouraged, notably the ^{12}Be($-$2p) reaction and fragmentation with more balanced neutron and proton numbers to be removed. Most importantly, the ^{3}H(^{8}He,p)^{10}He transfer experiment [21] should be repeated with significantly more statistics. Different transfer experiments with better statistics and resolutions are also desired. On the theory side, complete reaction dynamical calculations including the structure of the beam and target nuclei will be necessary

to explain the different observations. To investigate the target dependence, ^{11}Li($-$p) experiments are suggested to be performed at 50 MeV/u to 250 MeV/u with 50 MeV/u intervals, on both Hydrogen and heavy ion targets.

APPENDIX

Appendix

Guide for TMVA with MoNA

.1 Introduction

This document provide a basic, step-by-step guide for using the TMVA (Toolkit for Multivariate Data Analysis) with MoNA. TMVA is a built-in component since ROOT version 5.11/06, providing machine learning environments. Sections for the TMVA setup and running simple examples are basically rephrasings of corresponding chapters of the more detailed official guide listed at the end. This document assumes a basic understanding of ROOT and st_mona simulations, but you don't have to know details about multivariate methods.

TMVA can be used for classification and regression, but this document only considers the classification of 2-neutron events. An event where the first two hits are due to two different neutrons is referred as a true two neutron event, or "Signal" for consistency with the official guide, while an event where the first two hits are from the same neutron is referred to as a scattered one neutron event or "Background". Simulated Signal trees and Background trees are provided separately for training and testing a specific classifier. The trained classifier can be used for evaluating against simulations and data at the evaluation phase, resulting classifier responses that can be used for determining the classes of events.

.2 TMVA Setup

.2.1 Build Your Local TMVA Against Your ROOT (optional)

.2.1.1 Downloading TMVA Source Code

Building a local TMVA against ROOT might be beneficial, especially for ROOT users with an older version of TMVA. If needed, the source code of the latest TMVA can be downloaded at

https://sourceforge.net/projects/tmva/files/ as a gzipped tar file(.tgz).

.2.1.2 Unzipping and Building the TMVA Source Code

Move the downloaded .tgz file to the directory where you want to install, and unzip it in that directory by typing

```
~> tar -xvzf YourFileName.tgz
```

on a Linux terminal.

You can then build the source code by typing the following commands.

```
~> cd tmva
~/tmva> make
~/tmva> cd test
~/tmva/test/> setup.sh
```

Note "tmva" used above is the name of the directory generated by unzipping. By default it could be something like "TMVA-v4.2.0". The command "make" typically takes about 10

minutes.

Once built, by default you run your TMVA macros at /tmva/test/ directory. More frequently, if you want to work with TMVA somewhere else, additionally you should type

```
~> cd YourWorkingDirectroy
~/YourWorkingDirectroy> cp ~/tmva/test/setup.sh
~/YourWorkingDirectroy> source setup.sh <Your installation path>
```

where $< Your\ installation\ path >$ is the absolute path to where you make TMVA. Note setup.sh should be sourced for EVERY new terminal session. Also, note the path to your working directory should NOT contain white spaces.

According to the official guide, sourcing the setup.sh file is sufficient on a Unix/Linux machine. However, if you run ROOT on a Mac, additional steps might be necessary, and you should read the official guide.

.3 Running the Simple Example

.3.1 Run the Macros

Before dealing with simulations and data, you can run examples for pedagogical purposes. A simple example of classification is /tmva/test/TMVAClassification.C. Copy it to your working directory, and it can be run at the working directory by typing

```
root -l YourWorkingDirectory/TMVAClassification.C
```

That macro automatically downloads a toy ROOT file containing 4 variables with signal

and background saved in different trees. The macro uses half of the events for training and another half for testing for about 10 classifiers. You can also run through a specific type of classifier, for example, boosted decision trees (BDTs), by typing:

```
root -l YourWorkingDirectory/TMVAClassification.C\(\"BDT\"\)
```

If the macro ran successfully, a GUI like Fig. .1 pops up in the end. If errors occur, try to re-source setup.sh file as instructed by the previous section.

.3.2 Outputs of Interests

Each item of the GUI can be clicked. (1a) displays all input variables used for training and it displays background and the signal separately, as shown in Fig. .2. (4b) displays classifier responses which are outputs used for identifying the signal, as shown in Fig. .3. (5a) displays signal efficiency, background efficiency, signal purity, and signal significance, as a function of classifier output, based on the test set, as shown in Fig. .4.

.4 Prepare Trees for Training & Testing Simulations

If only "original" variables (x, y, z, t and q of the two hits) are used for training & testing, a GEANT tree of st_mona can be used directly, and this section can be skipped.

You can use aliases as input variables without causing any errors, but the actual values fed in TMVA might not be the values calculated from the aliases. Therefore, if you would like to work with "tuned" variables (variables derived from the original variables that make more physical sense) such as scattering angles, distances between two hits or hypothetical velocities between two hits, a ROOT file containing those variables should be prepared in

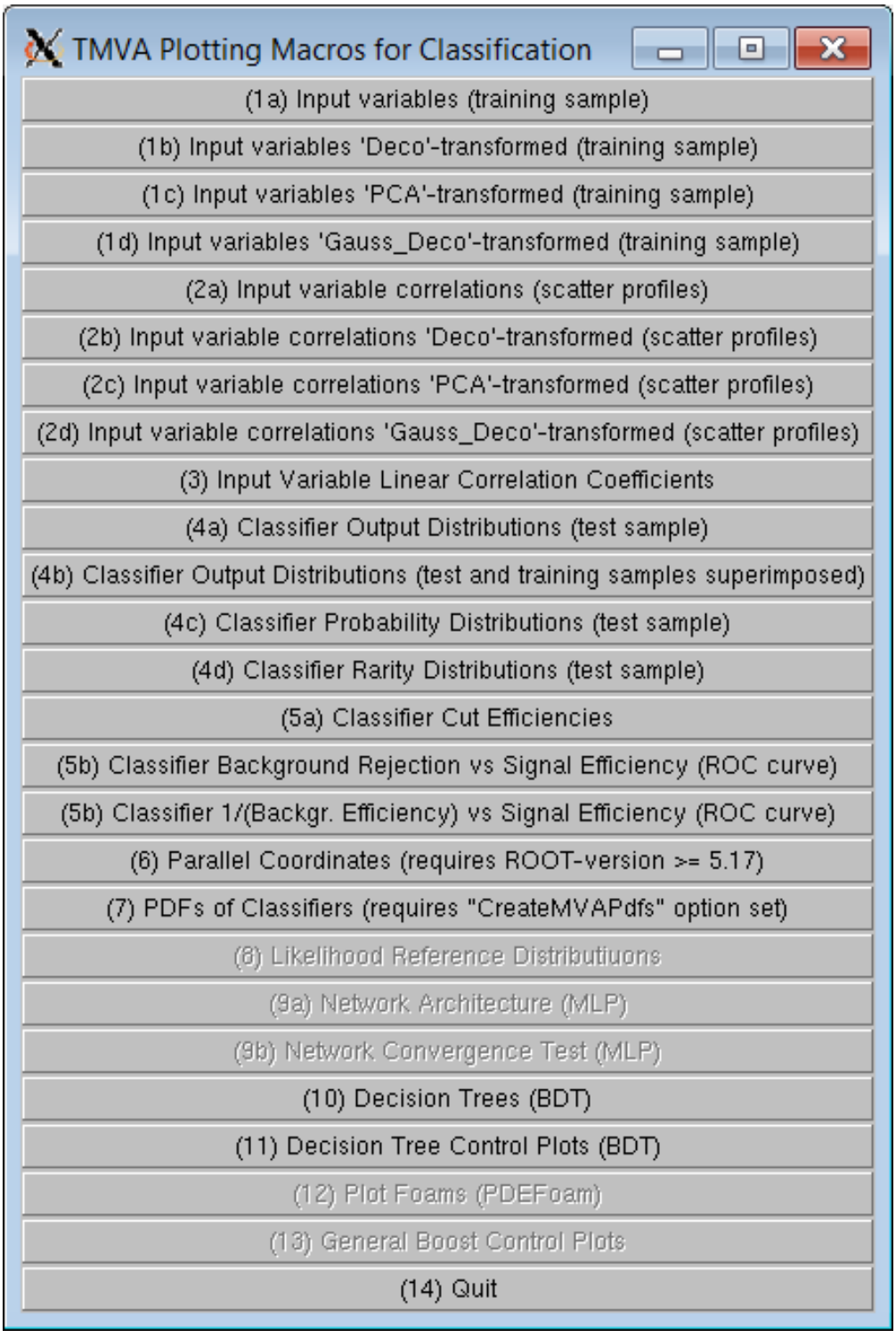

Figure .1: Screenshot of the TMVA GUI.

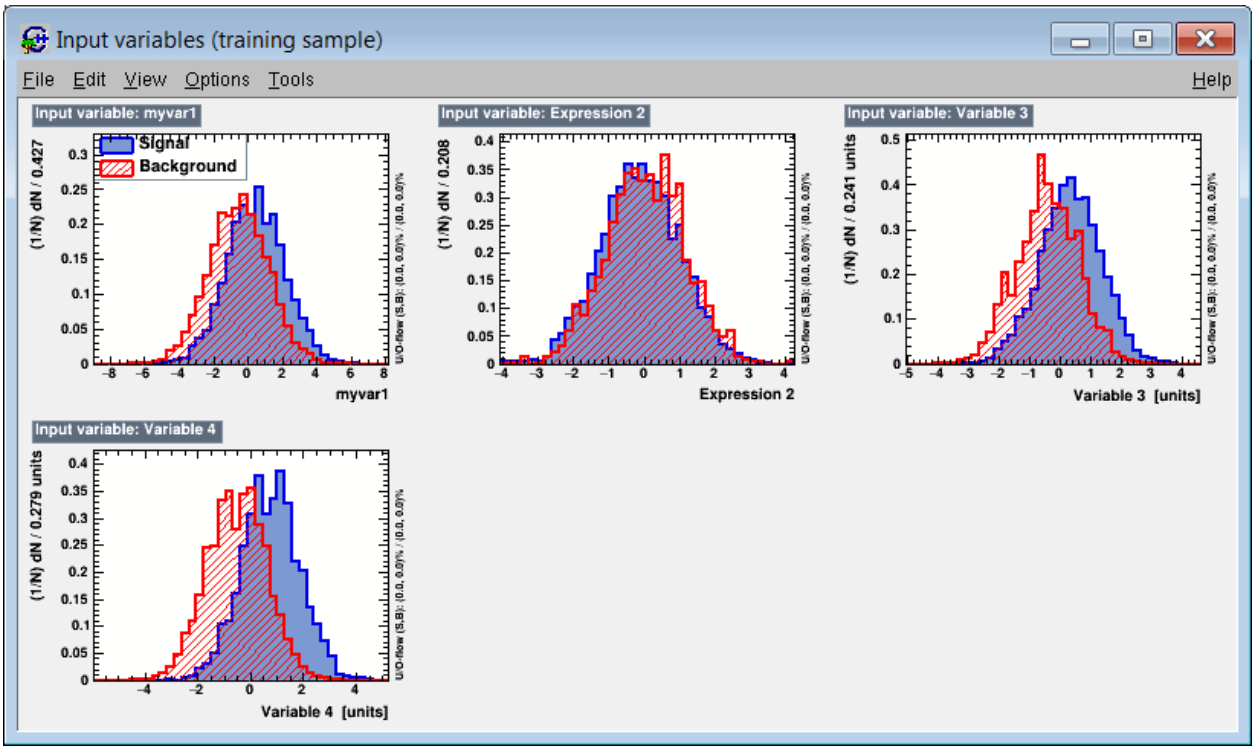

Figure .2: Screenshot of GUI (1a), input variables.

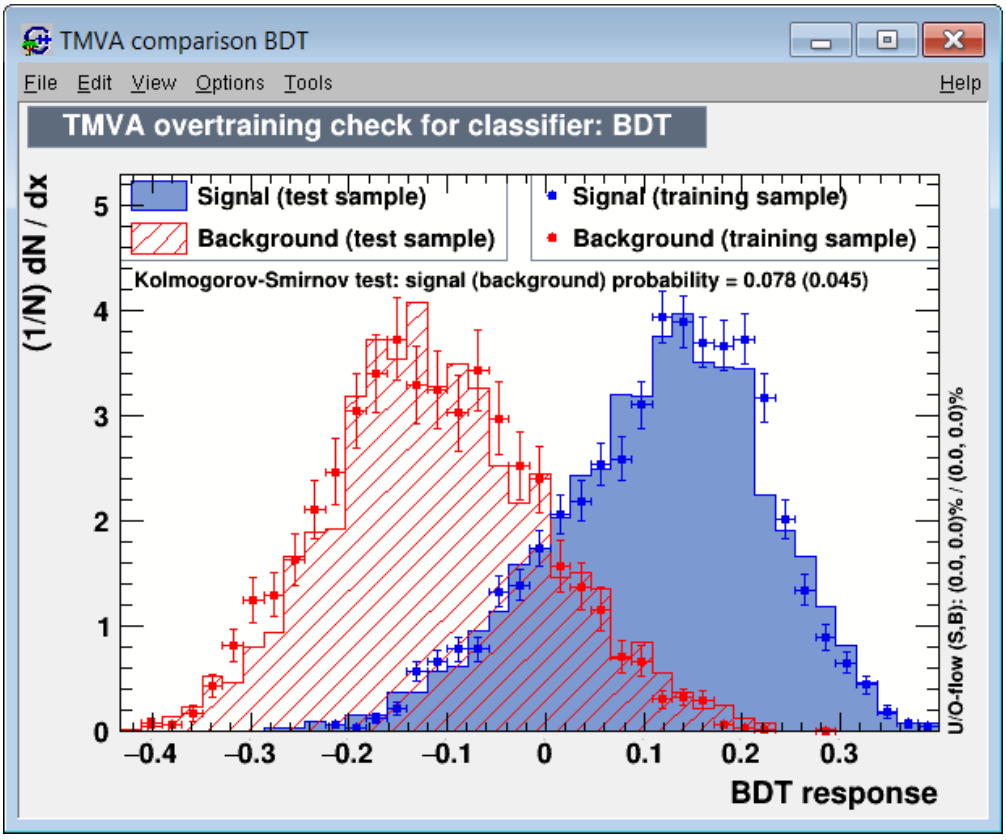

Figure .3: Screenshot of GUI (4b), classifier output.

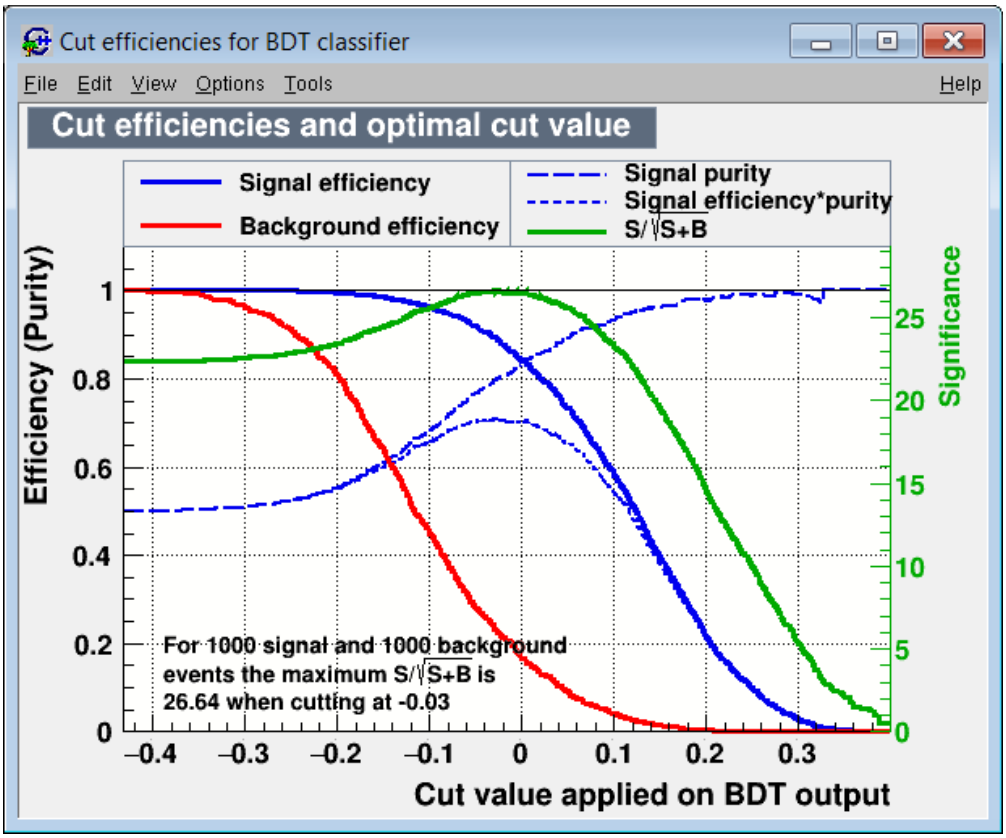

Figure .4: Screenshot of GUI (5a), classifier cut efficiencies.

advance.

An example macro for preparing such a file, called prepare_root_for_TMVAtraining.C , is provided with this document. You could simply use it by changing the input ROOT file path and output file path. In addition to x, y, z, t, and q of two hits of GEANT simulations, the sample macro also calculates the Lorentz factor, the scattering angle, the distance between two hits and the hypothetical velocity between two hits, and saves them to the output ROOT file.

The provided macro assumes the branches of neutron are beginning with "b13p". Different versions of st_moma might have different naming conventions, and the names of variables of this macro should be changed accordingly. More "tuned variables" can also be added but the details are beyond the scope of this document.

A file called "prepared_sim_for_training.root" generated by the above-mentioned macro is provided, and it can be directly used for testing the macro mentioned below.

.5 Training and Testing Against MoNA Simulations

This section focuses on how you can modify a macro called TMVAClassification2Neutron.C, provided with this document. A ROOT file directly from st_mona or prepared by the previous section will be used. In both cases, only two neutron simulations should be considered since TMVA must know what is Signal, and what is Background, while 1n simulations only provide Background.

.5.1 Change paths

Two paths need to be changed:

```
factory->AddVariable( "57.3*n0_n1_scat_angle","Scattering Angle","Deg", 'D' );
factory->AddVariable( "939.565560*(n0_gamma-1)", "KE of the first hit", "MeV", 'D' );
factory->AddVariable( "939.565560*(n1_gamma-1)", "KE of the second hit", "MeV", 'D' );
factory->AddVariable( "b13pg1light", "light deposit of the first hit", "MeVee", 'D' );
factory->AddVariable( "b13pg2light", "light deposit of the second hit", "MeVee", 'D' );
factory->AddVariable( "b13pg1z*100", "first hit z", "cm", 'D' );
factory->AddVariable( "b13pg1x*100", "first hit x", "cm", 'D' );
factory->AddVariable( "b13pg1y*100", "first hit y", "cm", 'D' );
factory->AddVariable( "b13pg2z*100", "second hit z", "cm", 'D' );
factory->AddVariable( "b13pg2x*100", "second hit x", "cm", 'D' );
factory->AddVariable( "b13pg2y*100", "second hit y", "cm", 'D' );
factory->AddVariable( "b13pg1t", "first hit t", "ns", 'D' );
factory->AddVariable( "b13pg2t", "second hit t", "ns", 'D' );
factory->AddVariable( "n0_n1_distance",        "n0n1 distance", "cm", 'D' );
factory->AddVariable( "n0_n1_distance/(b13pg2t-b13pg1t)",        "n0n1 velocity", "cm/ns", 'D' );
```

Figure .5: Lines of the macro for setting variables.

- change “YourOutput.root” to a name you want for saving results of training & testing
- change “PathToYourRootFile.root” to the actual path of the root file you want use for training & testing

.5.2 Change Variables

In the provided macro, line 192 to 206 are commands for setting variables, as shown in Fig. .5. Four items are listed within the parentheses. The first one is a variable to be added for training. Branches of the input tree should be used, and simple expressions are supported. The second is the name of the variable, which will appear in a GUI later. The remaining are the unit and the type of the variable, where ‘D’ means double-precision floating-point format.

More variables can be added similarly, and the existing one’s can be commented if you don’t want them to be part of training.

```
   TCut mycuts = "((b13pg1x == b13pn1g1x && b13pg2x == b13pn2g1x) || (b13pg1x == b13pn2g1x && b13pg2x == b13pn1
g1x))&&b13pg1light>0.91&&b13pg2light>0.91"; // for example: TCut mycuts = "abs(var1)<0.5 && abs(var2-0.5)<1";
   TCut mycutb = "((b13pg1x == b13pn1g1x && b13pg2x == b13pn2g1x) || (b13pg1x == b13pn2g1x && b13pg2x == b13pn1
g1x))!=1&&b13pg1light>0.91&&b13pg2light>0.91"; // for example: TCut mycutb = "abs(var1)<0.5";
```

Figure .6: Lines of the macro for cuts.

.5.3 Change Cuts

In the simple macro, signal and background are placed in separated trees. However, due to the nature of st_mona simulations, true 2 neutron events (Signal) and 1 neutron scattered twice events (Background) are mixed in the same tree.

Although it is possible to split simulated Signal and Background into different trees during the pre-training phase, for convenience one can set the same tree as both signal tree and background tree but with different cuts.

Fig. .6 shows the applied cuts from line 294 to line 295. An event is guaranteed to be signal if the first hit is the first neutron and the second hit is the second neutron or the first hit is the second neutron and the second hit is the first neutron. Otherwise, an event is background. b13pg1light and b13pg2light are required to be greater than the light threshold used for simulating the input file so that only events with more than 2 valid hits are used.

.5.4 Training & Testing Results

Running the macro you just modified is similar to running a simple example. Just enter:

```
root -l YourWorkingDirectory/TMVAClassification2Neutron.C
```

or

```
root -l YourWorkingDirectory/TMVAClassification2Neutron.C\(\"BDT\"\)
```

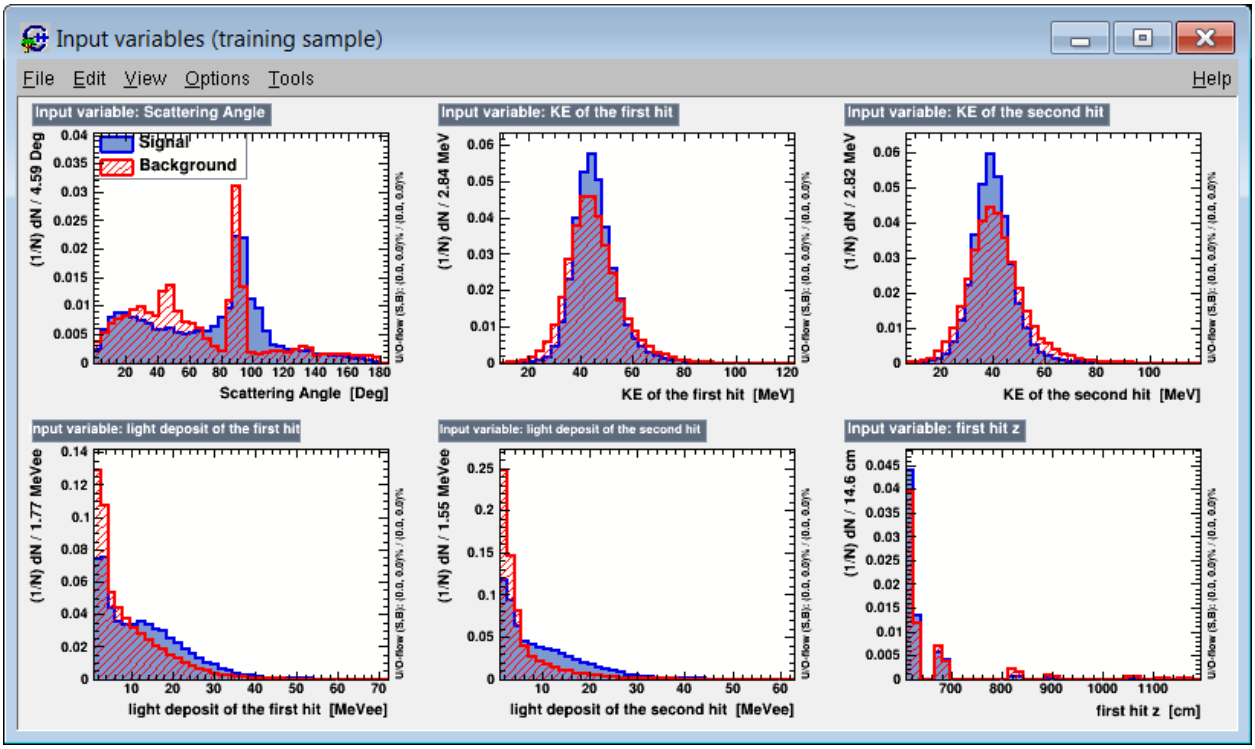

Figure .7: Screenshot of GUI (1a), input variables with st_mona.

if a specific classifier is desired.

The same GUI as Fig. .1 pops up after a successful execution. Typical training&testing plots are given below as Fig. .7, Fig. .8, and Fig. .9.

.6 Evaluating MoNA Data or Simulations

In the evaluation phase we get classifier responses for events we want to know their identity, according to information contained in those events. Weight files inside "weights" directory generated by the training procedure are used, so the working directory of the evaluating phase should be the same as the training and testing phase.

Again, since aliases do not work properly, files to be evaluated might have to be prepared in advance if any "tuned" variables are involved. Data, 1n simulations or 2n simulations need

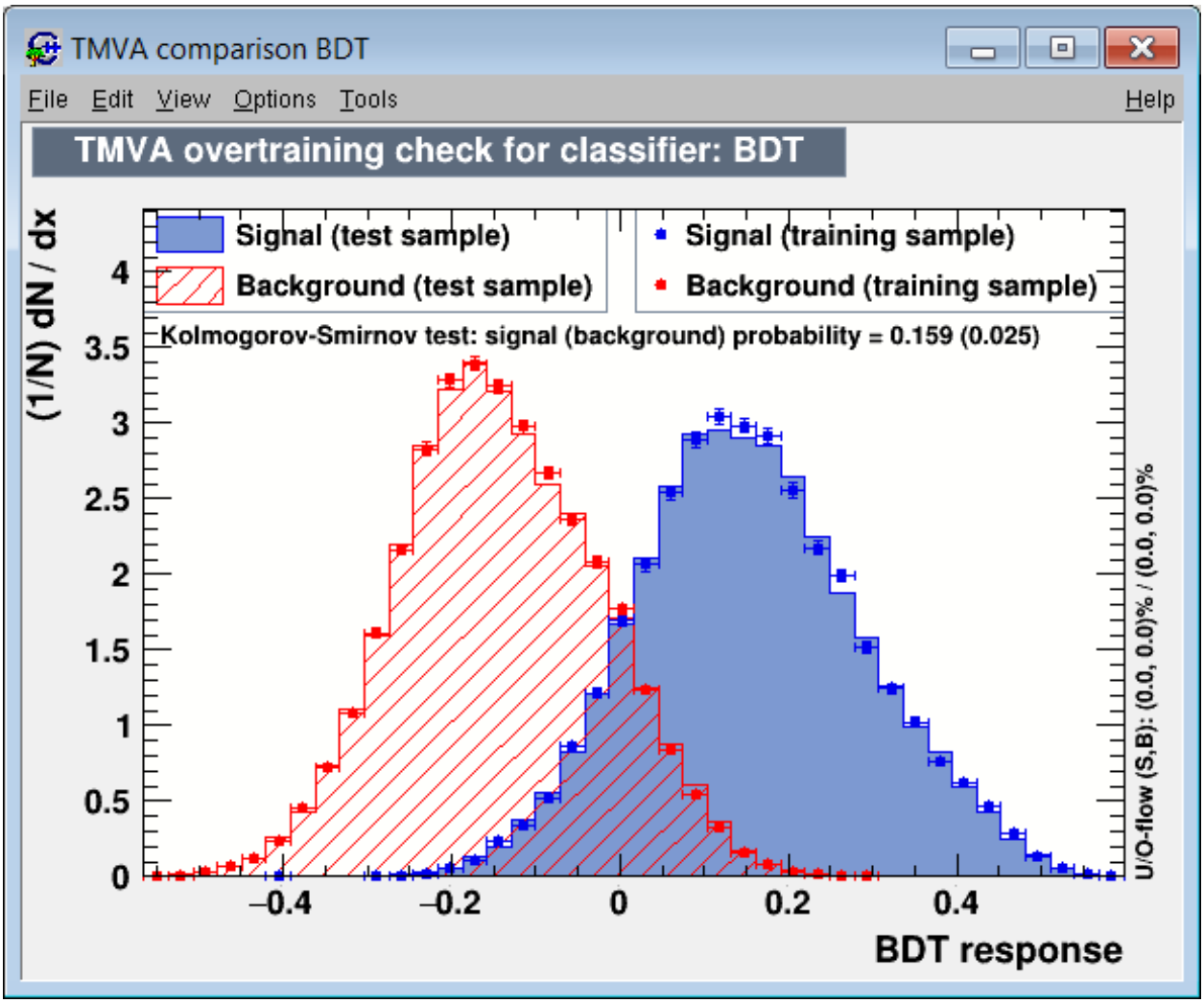

Figure .8: Screenshot of GUI (4b), classifier output with st_mona.

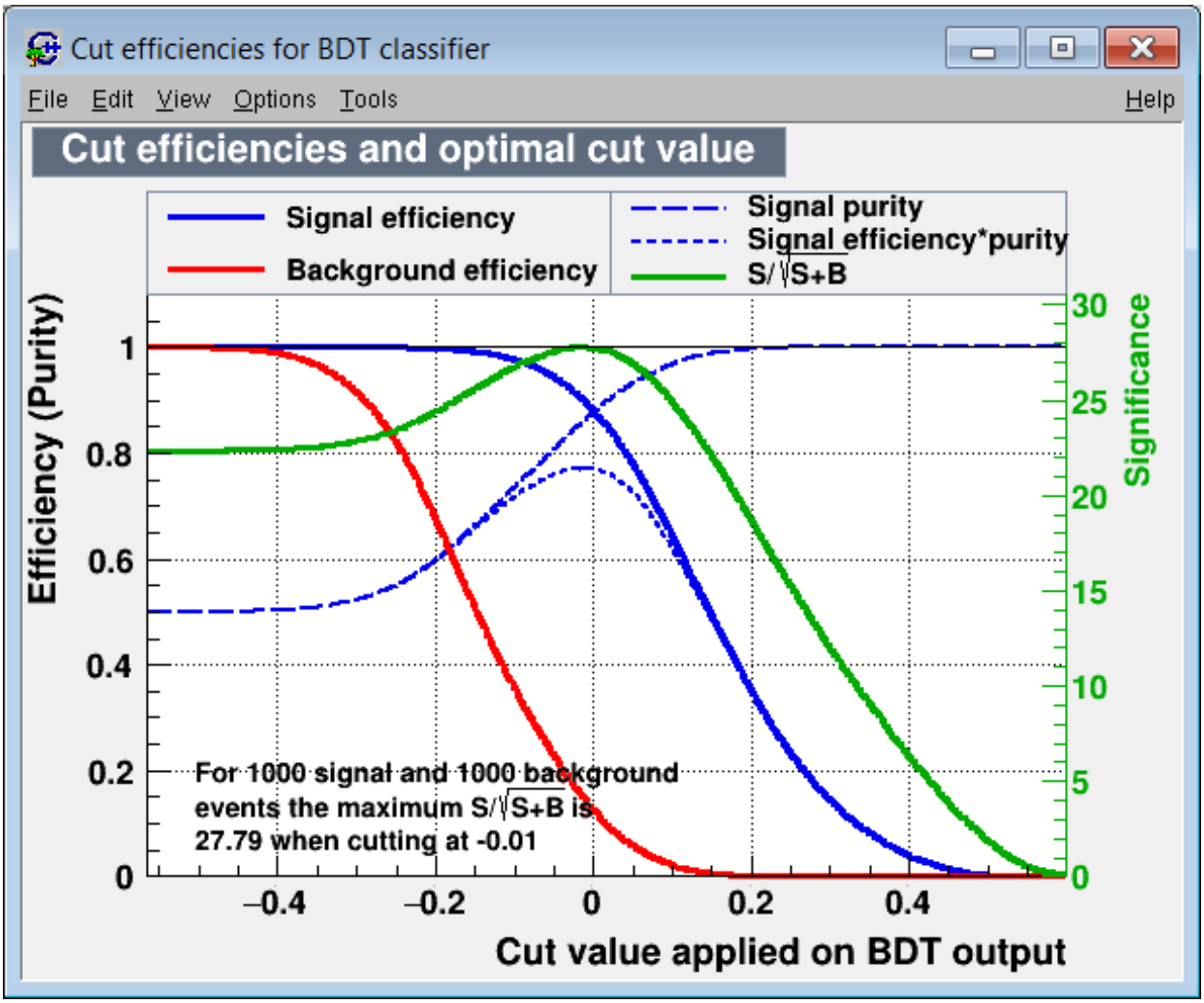

Figure .9: Screenshot of GUI (5a) classifier, cut efficiencies with st_mona.

to be prepared in slightly different ways, and changes might also be necessary due to the software version or the experimental setup. Therefore, one simple macro that can deal with all cases cannot be provided. Instead, this section mentions key concepts of the evaluating phase and shows how one can evaluate a provided ROOT file "data_to_be_evaluated.root" by using the provided macro "TMVAClassificationApplication2Neutron.C". Only the BDT method is used in that macro. If ROOT files with the same branches can be generated, the provided application macro can be used for evaluating them.

.6.1 Set the TMVA Reader

Fig. .10 shows line 143 to line 157 of the macro "TMVAClassificationApplication2Neutron.C". There are two arguments for each command. The first is the NAME of the variable, and should be exactly the same as the name used in the training phase (Fig. .5). The second argument is the corresponding variable. It should originate from the root file to be evaluated.

Note, the type given in the weight files is float so the variables used as the second argument should also be declared as float type variables.

.6.2 Getting Responses from a Classifier

To get a response of one entry, you should first assign the correct values of the entry into the variables used as the second argument in Fig. .10. For example, you should assign the scattering angle in degrees to n0_n1_scat_angle, and you should assign the kinetic energy of the first hit in MeV to n0_gamma. Those steps are accomplished by lines 267 to 280 and lines 306 to 320.

Once the assignment is finished, the classifier response can be reached by:

```
reader->AddVariable( "57.3*n0_n1_scat_angle",&n0_n1_scat_angle);
reader->AddVariable( "939.565560*(n0_gamma-1)",&n0_gamma );
reader->AddVariable( "939.565560*(n1_gamma-1)",&n1_gamma  );
reader->AddVariable( "b13pg1light",&b13pg1light  );
reader->AddVariable( "b13pg2light",&b13pg2light );
reader->AddVariable( "b13pg1z*100",&b13pg1z );
reader->AddVariable( "b13pg1x*100",&b13pg1x );
reader->AddVariable( "b13pg1y*100",&b13pg1y );
reader->AddVariable( "b13pg2z*100",&b13pg2z  );
reader->AddVariable( "b13pg2x*100",&b13pg2x  );
reader->AddVariable( "b13pg2y*100",&b13pg2y  );
reader->AddVariable( "b13pg1t", &b13pg1t );
reader->AddVariable( "b13pg2t", &b13pg2t );
reader->AddVariable( "n0_n1_distance", &n0_n1_distance);
reader->AddVariable( "n0_n1_distance/(b13pg2t-b13pg1t)", &n0_n1_v);
```

Figure .10: Lines of the macro for setting the TMVA reader.

```
bdt=reader->EvaluateMVA(``BDT method'')
```

as shown by line 333 in the application macro. Then the value of the response can be saved in a tree for future use.

.6.3 Use the Example for Data Classification

Copy "data_to_be_evaluated.root" and "TMVAClassificationApplication2Neutron.C" to your working directory.

Before using the example macro for the evaluating phase, you should run the example macro for the training & testing phase. Then at the same working directory, the evaluating macro can be run by typing

```
root -l TMVAClassificationApplication2Neutron.C\(\"BDT\"\)
```

where the ending is NOT optional.

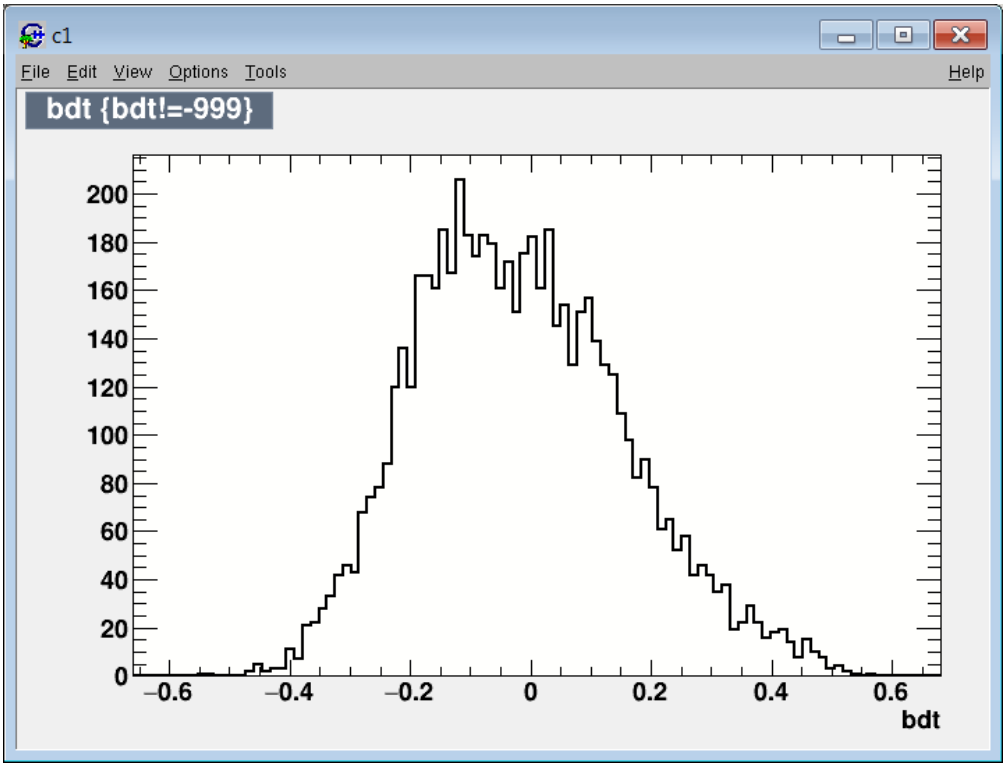

Figure .11: Typical BDT responses towards data. Gated on valid events.

Once finished, a ROOT file "TMVApp2nda.root" is generated in the working directory. The only leaf should be "bdt" and it is the responses of the BDT classifier trained from previous phases. Typical BDT responses are shown in Fig. .11. The tree in the file can be added as a friend to the original tree in your data file. Then a cut like "$bdt > 0$" can be used as a true 2n gate.

BIBLIOGRAPHY

BIBLIOGRAPHY

[1] A. Navin, D. W. Anthony, T. Aumann, T. Baumann, D. Bazin, Y. Blumenfeld, B. A. Brown, T. Glasmacher, P. G. Hansen, R. W. Ibbotson, P. A. Lofy, V. Maddalena, K. Miller, T. Nakamura, B. V. Pritychenko, B. M. Sherrill, E. Spears, M. Steiner, J. A. Tostevin, J. Yurkon, and A. Wagner. Direct evidence for the breakdown of the $N = 8$ shell closure in ^{12}Be. *Phys. Rev. Lett.*, 85:266–269, Jul 2000.

[2] G. Gori, F. Barranco, E. Vigezzi, and R. A. Broglia. Parity inversion and breakdown of shell closure in Be isotopes. *Phys. Rev. C*, 69:041302, Apr 2004.

[3] T. Nakamura, N. Kobayashi, Y. Kondo, Y. Satou, N. Aoi, H. Baba, S. Deguchi, N. Fukuda, J. Gibelin, N. Inabe, M. Ishihara, D. Kameda, Y. Kawada, T. Kubo, K. Kusaka, A. Mengoni, T. Motobayashi, T. Ohnishi, M. Ohtake, N. A. Orr, H. Otsu, T. Otsuka, A. Saito, H. Sakurai, S. Shimoura, T. Sumikama, H. Takeda, E. Takeshita, M. Takechi, S. Takeuchi, K. Tanaka, K. N. Tanaka, N. Tanaka, Y. Togano, Y. Utsuno, K. Yoneda, A. Yoshida, and K. Yoshida. Halo structure of the island of inversion nucleus ^{31}Ne. *Phys. Rev. Lett.*, 103:262501, Dec 2009.

[4] B. V. Pritychenko, T. Glasmacher, P. D. Cottle, R. W. Ibbotson, K. W. Kemper, L. A. Riley, A. Sakharuk, H. Scheit, M. Steiner, and V. Zelevinsky. Structure of the "island of inversion" nucleus ^{33}Mg. *Phys. Rev. C*, 65:061304, Jun 2002.

[5] I. Tanihata, H. Savajols, and R. Kanungo. Recent experimental progress in nuclear halo structure studies. *Progress in Particle and Nuclear Physics*, 68:215 – 313, 2013.

[6] A. M. Poskanzer, S. W. Cosper, Earl K. Hyde, and Joseph Cerny. New isotopes: ^{11}Li, ^{14}B, and ^{15}B. *Phys. Rev. Lett.*, 17:1271–1274, Dec 1966.

[7] S. L. Whetstone and T. D. Thomas. Light charged particles from spontaneous fission of ^{252}Cf. *Phys. Rev.*, 154:1174–1181, Feb 1967.

[8] S. W. Cosper, J. Cerny, and R. C. Gatti. Long-range particles of z = 1to4 emitted during the spontaneous fission of ^{252}Cf. *Phys. Rev.*, 154:1193–1206, Feb 1967.

[9] A.G. Artukh, V.V. Avdeichikov, G.F. Gridnev, V.L. Mikheev, V.V. Volkov, and J. Wilczyński. Evidence for particle instability of ^{10}He. *Nuclear Physics A*, 168(2):321 – 327, 1971.

[10] Beznogikh G.G., Zhidkov N.K., Kirillova L.F., Nikitin V.A., Nomokonov P.V., Avdeichikov V.V., Murin Yu.A., Oplavin V.S., Maisyukov V.D.and Maslennikov Yu.V.,

Shevchenko A.P., Buyak A., and Shavlovski M. Search for ^{10}He isotope in the fragmentation reaction of a ^{232}Th target nucleus. 30:323–327, 1979.

[11] Oganesyan Yu. Ts., Penionzhkevich Yu. E., Gierlik E., Kalpakchieva R., Pawlat T., Borcea C., Belozerov A. V., Kharitonov Yu. P., Tret'yakova S. P., Subbotin V. G., Luk'yanov S. M., Pronin N. V., and Bykov A. A. Experimental search for ^{10}He nuclei in heavy-ion-induced reactions. 36:129–132, 1982.

[12] T. Kobayashi, O. Yamakawa, K. Omata, K. Sugimoto, T. Shimoda, N. Takahashi, and I. Tanihata. Projectile fragmentation of the extremely neutron-rich nucleus ^{11}Li at 0.79 GeV/nucleon. *Phys. Rev. Lett.*, 60:2599–2602, Jun 1988.

[13] J. Stevenson, B. A. Brown, Y. Chen, J. Clayton, E. Kashy, D. Mikolas, J. Nolen, M. Samuel, B. Sherrill, J. S. Winfield, Z. Q. Xie, R. E. Julies, and W. A. Richter. Search for the exotic nucleus ^{10}He. *Phys. Rev. C*, 37:2220–2223, May 1988.

[14] A.A. Korsheninnikov, K. Yoshida, D.V. Aleksandrov, N. Aoi, Y. Doki, N. Inabe, M. Fujimaki, T. Kobayashi, H. Kumagai, C.-B. Moon, et al. Observation of ^{10}He. *Physics Letters B*, 326(1-2):31–36, 1994.

[15] T. Kobayashi, K. Yoshida, A. Ozawa, I. Tanihata, A. Korsheninnikov, E. Nikolski, and T. Nakamura. Quasifree nucleon-knockout reactions from neutron-rich nuclei by a proton target: p(^{6}He,pn)^{5}He, p(^{11}Li,pn)^{10}Li, p(^{6}He,2p)^{5}H, and p(^{11}Li,2p)^{10}He. *Nuclear Physics A*, 616(1):223 – 230, 1997.

[16] H.T. Johansson, Yu. Aksyutina, T. Aumann, K. Boretzky, M.J.G. Borge, A. Chatillon, L.V. Chulkov, D. Cortina-Gil, U. Datta Pramanik, H. Emling, C. Forssén, H.O.U. Fynbo, H. Geissel, G. Ickert, B. Jonson, R. Kulessa, C. Langer, M. Lantz, T. LeBleis, K. Mahata, M. Meister, G. Münzenberg, T. Nilsson, G. Nyman, R. Palit, S. Paschalis, W. Prokopowicz, R. Reifarth, A. Richter, K. Riisager, G. Schrieder, H. Simon, K. Sümmerer, O. Tengblad, H. Weick, and M.V. Zhukov. The unbound isotopes ^{9,10}He. *Nuclear Physics A*, 842(1):15 – 32, 2010.

[17] H.T. Johansson, Yu. Aksyutina, T. Aumann, K. Boretzky, M.J.G. Borge, A. Chatillon, L.V. Chulkov, D. Cortina-Gil, U. Datta Pramanik, H. Emling, C. Forssén, H.O.U. Fynbo, H. Geissel, G. Ickert, B. Jonson, R. Kulessa, C. Langer, M. Lantz, T. LeBleis, K. Mahata, M. Meister, G. Münzenberg, T. Nilsson, G. Nyman, R. Palit, S. Paschalis, W. Prokopowicz, R. Reifarth, A. Richter, K. Riisager, G. Schrieder, N.B. Shulgina, H. Simon, K. Sümmerer, O. Tengblad, H. Weick, and M.V. Zhukov. Three-body correlations in the decay of ^{10}He and ^{13}Li. *Nuclear Physics A*, 847(1):66 – 88, 2010.

[18] C. Forssén, B. Jonson, and M.V. Zhukov. A correlated background in invariant mass spectra of three-body systems. *Nuclear Physics A*, 673(1):143 – 156, 2000.

[19] A.N. Ostrowski, H.G. Bohlen, B. Gebauer, S.M. Grimes, R. Kalpakchieva, Th. Kirchner, T.N. Massey, W. Von Oertzen, Th. Stolla, M. Wilpert, et al. Spectroscopy of ^{10}He. *Physics Letters B*, 338(1):13–19, 1994.

[20] M.S. Golovkov, L.V. Grigorenko, G.M. Ter-Akopian, A.S. Fomichev, Yu.Ts. Oganessian, V.A. Gorshkov, S.A. Krupko, A.M. Rodin, S.I. Sidorchuk, R.S. Slepnev, S.V. Stepantsov, R. Wolski, D.Y. Pang, V. Chudoba, A.A. Korsheninnikov, E.A. Kuzmin, E.Yu. Nikolskii, B.G. Novatskii, D.N. Stepanov, P. Roussel-Chomaz, W. Mittig, A. Ninane, F. Hanappe, L. Stuttgé, A.A. Yukhimchuk, V.V. Perevozchikov, Yu.I. Vinogradov, S.K. Grishechkin, and S.V. Zlatoustovskiy. The ^{8}He and ^{10}He spectra studied in the reaction. *Physics Letters B*, 672(1):22 – 29, 2009.

[21] S. I. Sidorchuk, A. A. Bezbakh, V. Chudoba, I. A. Egorova, A. S. Fomichev, M. S. Golovkov, A. V. Gorshkov, V. A. Gorshkov, L. V. Grigorenko, P. Jalůvková, G. Kaminski, S. A. Krupko, E. A. Kuzmin, E. Yu. Nikolskii, Yu. Ts. Oganessian, Yu. L. Parfenova, P. G. Sharov, R. S. Slepnev, S. V. Stepantsov, G. M. Ter-Akopian, R. Wolski, A. A. Yukhimchuk, S. V. Filchagin, A. A. Kirdyashkin, I. P. Maksimkin, and O. P. Vikhlyantsev. Structure of ^{10}He low-lying states uncovered by correlations. *Phys. Rev. Lett.*, 108:202502, May 2012.

[22] L. V. Grigorenko and M. V. Zhukov. Problems with the interpretation of the ^{10}He ground state. *Phys. Rev. C*, 77:034611, Mar 2008.

[23] Z. Kohley, J. Snyder, T. Baumann, G. Christian, P. A. DeYoung, J. E. Finck, R. A. Haring-Kaye, M. Jones, E. Lunderberg, B. Luther, S. Mosby, A. Simon, J. K. Smith, A. Spyrou, S. L. Stephenson, and M. Thoennessen. Unresolved question of the ^{10}He ground state resonance. *Phys. Rev. Lett.*, 109:232501, Dec 2012.

[24] A. Matta, D. Beaumel, H. Otsu, V. Lapoux, N. K. Timofeyuk, N. Aoi, M. Assié, H. Baba, S. Boissinot, R. J. Chen, F. Delaunay, N. de Sereville, S. Franchoo, P. Gangnant, J. Gibelin, F. Hammache, Ch. Houarner, N. Imai, N. Kobayashi, T. Kubo, Y. Kondo, Y. Kawada, L. H. Khiem, M. Kurata-Nishimura, E. A. Kuzmin, J. Lee, J. F. Libin, T. Motobayashi, T. Nakamura, L. Nalpas, E. Yu. Nikolskii, A. Obertelli, E. C. Pollacco, E. Rindel, Ph. Rosier, F. Saillant, T. Sako, H. Sakurai, A. M. Sánchez-Benítez, J-A. Scarpaci, I. Stefan, D. Suzuki, K. Takahashi, M. Takechi, S. Takeuchi, H. Wang, R. Wolski, and K. Yoneda. New findings on structure and production of ^{10}He from ^{11}Li with the (d,^{3}He) reaction. *Phys. Rev. C*, 92:041302, Oct 2015.

[25] A.A. Korsheninnikov, B.V. Danilin, and M.V. Zhukov. Possible existence of ^{10}He as narrow three-body resonance. *Nuclear Physics A*, 559(2):208 – 220, 1993.

[26] K. Katō, S. Aoyama, S. Mukai, and K. Ikeda. Binding and excitation mechanisms of ^{6}He, ^{10}He and ^{11}Li. *Nuclear Physics A*, 588(1):c29 – c34, 1995. Proceedings of the Fifth International Symposium on Physics of Unstable Nuclei.

[27] S. Aoyama, K. Katō, and K. Ikeda. Resonances in ^{9}He and ^{10}He. *Phys. Rev. C*, 55:2379–2384, May 1997.

[28] S. Aoyama, K. Katō, and K. Ikeda. Three-Body Cluster Resonances in ^{11}Li and ^{10}He. *Progress of Theoretical Physics Supplement*, 146:540–542, 03 2002.

[29] S. Aoyama. Theoretical prediction for the ground state of ^{10}He with the method of analytic continuation in the coupling constant. *Phys. Rev. Lett.*, 89:052501, Jul 2002.

[30] S. Aoyama. Analyses of three-body s-wave resonances with analytic continuation in the coupling constant. *Modern Physics Letters A*, 18(02n06):422–425, 2003.

[31] S. Aoyama. Where is the ground state of ^{10}He? *Nuclear Physics A*, 722:C474 – C478, 2003.

[32] H. Kamada, M. Yamaguchi, and E. Uzu. Core-excitation three-cluster model description of ^{8}He and ^{10}He. *Phys. Rev. C*, 88:014005, Jul 2013.

[33] K. Fossez, J. Rotureau, and W. Nazarewicz. Energy spectrum of neutron-rich helium isotopes: Complex made simple. *Phys. Rev. C*, 98:061302, Dec 2018.

[34] H. T. Fortune. Structure of ^{10}He and the reaction ^{8}He(t,p). *Phys. Rev. C*, 88:034328, Sep 2013.

[35] H. T. Fortune. Relative population of 0^+ states in ^{10}He in various reactions. *Phys. Rev. C*, 88:054623, Nov 2013.

[36] H. T. Fortune. Constraints on energies of ^{10}He(0^+) and ^{9}He$(1/2^+)$. *Phys. Rev. C*, 91:034306, Mar 2015.

[37] H. T. Fortune. Solution for energies and mixing of two 0^+ states in ^{10}He. *Chinese Physics Letters*, 33(9):092101, sep 2016.

[38] M. D. Jones, Z. Kohley, T. Baumann, G. Christian, P. A. DeYoung, J. E. Finck, N. Frank, R. A. Haring-Kaye, A. N. Kuchera, B. Luther, S. Mosby, J. K. Smith, J. Snyder, A. Spyrou, S. L. Stephenson, and M. Thoennessen. Further insights into the reaction ^{14}Be$(CH_2, X)^{10}$He. *Phys. Rev. C*, 91:044312, Apr 2015.

[39] P. G. Sharov, I. A. Egorova, and L. V. Grigorenko. Anomalous population of ^{10}He states in reactions with ^{11}Li. *Phys. Rev. C*, 90:024610, Aug 2014.

[40] F. James. MonteCarlo phase space. *CERN Yellow Report No. 68-15*, 1968.

[41] G. Breit and E. Wigner. Capture of slow neutrons. *Phys. Rev.*, 49:519–531, Apr 1936.

[42] I. J. Thompson and F. M. Nune. *Nuclear Reactions for Astrophysics: Principles, Calculation and Applications of Low-Energy Reactions*. Cambridge University Press, The Edinburgh Building, Cambridge CB2 8RU, UK, 2009.

[43] A. M. Lane and R. G. Thomas. R-matrix theory of nuclear reactions. *Rev. Mod. Phys.*, 30:257–353, Apr 1958.

[44] J. Raynal and J. Revai. Transformation coefficients in the hyperspherical approach to the three-body problem. *Il Nuovo Cimento A (1965-1970)*, 68(4):612–622, Aug 1970.

[45] H. Simon, M. Meister, T. Aumann, M.J.G. Borge, L.V. Chulkov, U. Datta Pramanik, Th.W. Elze, H. Emling, C. Forssén, H. Geissel, M. Hellström, B. Jonson, J.V. Kratz, R. Kulessa, Y. Leifels, K. Markenroth, G. Münzenberg, F. Nickel, T. Nilsson, G. Nyman, A. Richter, K. Riisager, C. Scheidenberger, G. Schrieder, O. Tengblad, and M.V. Zhukov. Systematic investigation of the drip-line nuclei ^{11}Li and ^{14}Be and their unbound subsystems ^{10}Li and ^{13}Be. *Nuclear Physics A*, 791(3):267 – 302, 2007.

[46] M.V. Zhukov, B.V. Danilin, D.V. Fedorov, J.M. Bang, I.J. Thompson, and J.S. Vaagen. Bound state properties of borromean halo nuclei: ^{6}He and ^{11}Li. *Physics Reports*, 231(4):151 – 199, 1993.

[47] I.S. Gradshteyn and I.M. Ryzhik. *Table of Integrals, Series, and Products*. Academic Press, San Diego, 1980.

[48] M. Birch, B. Singh, I. Dillmann, D. Abriola, T.D. Johnson, E.A. McCutchan, and A.A. Sonzogni. Evaluation of beta-delayed neutron emission probabilities and half-lives for Z = 2-28. *Nuclear Data Sheets*, 128:131 – 184, 2015.

[49] I. Tanihata. Radioactive beam facilities and their physics program. *Nuclear Physics A*, 553:361 – 372, 1993.

[50] F. Marti, P. Miller, D. Poe, M. Steiner, J. Stetson, and X. Y. Wu. Commissioning of the coupled cyclotron system at NSCL. *AIP Conference Proceedings*, 600(1):64–68, 2001.

[51] D.J. Morrissey, B.M. Sherrill, M. Steiner, A. Stolz, and I. Wiedenhoever. Commissioning the A1900 projectile fragment separator. *Nuclear Instruments and Methods in Physics Research Section B: Beam Interactions with Materials and Atoms*, 204:90 – 96, 2003. 14th International Conference on Electromagnetic Isotope Separators and Techniques Related to their Applications.

[52] M. D. Bird, Steven J. Kenney, J. Toth, H. W Weijers, J. C. DeKamp, M. Thoennessen, and A. F. Zeller. System testing and installation of the NHMFL/NSCL sweeper magnet. *IEEE transactions on applied superconductivity*, 15(2):1252–1254, 2005.

[53] B. Luther, T. Baumann, M. Thoennessen, J. Brown, P. DeYoung, J. Finck, J. Hinnefeld, R. Howes, K. Kemper, P. Pancella, G. Peaslee, W. Rogers, and S. Tabor. MoNA|TheModularNeutronArray. *Nuclear Instruments and Methods in Physics Research Section A: Accelerators, Spectrometers, Detectors and Associated Equipment*, 505(1–2):33 – 35, 2003. Proceedings of the tenth Symposium on Radiation Measurements and Applications.

[54] T. Baumann, J. Boike, J. Brown, M. Bullinger, J.P. Bychoswki, S. Clark, K. Daum, P.A. DeYoung, J.V. Evans, J. Finck, N. Frank, A. Grant, J. Hinnefeld, G.W. Hitt, R.H. Howes, B. Isselhardt, K.W. Kemper, J. Longacre, Y. Lu, B. Luther, S.T. Marley, D. McCollum, E. McDonald, U. Onwuemene, P.V. Pancella, G.F. Peaslee, W.A. Peters, M. Rajabali, J. Robertson, W.F. Rogers, S.L. Tabor, M. Thoennessen, E. Tryggestad, R.E. Turner, P.J. VanWylen, and N. Walker. Construction of a modular large-area neutron detector for the NSCL. *Nuclear Instruments and Methods in Physics Research Section A: Accelerators, Spectrometers, Detectors and Associated Equipment*, 543(2–3):517 – 527, 2005.

[55] S.-G. Crystals. "bc-400, bc-404, bc-408, bc-412, bc-416 premium plastic scintillators". Technical report, 2005.

[56] M. Jones. *Spectroscopy of Neutron Unbound States in* ^{24}O *and* ^{23}N. PhD thsis, Michigan State University, 2015.

[57] J. Smith. *Unbound States in the Lightest Island of Inversion: Neutron Decay Measurements of* ^{11}Li*,* ^{10}Li*, and* ^{12}Be. PhD thsis, Michigan State University, 2014.

[58] N. Frank. *Spectroscopy of Neutron Unbound States in Neutron Rich Oxygen Isotopes.* PhD thsis, Michigan State University, 2006.

[59] W. Peters. *Study of Neutron Unbound States Using the* ModularNeutronArray(MoNA). PhD thsis, Michigan State University, 2007.

[60] G. Christian. *Spectroscopy of Neutron-Unbound Fluorine.* PhD thsis, Michigan State University, 2011.

[61] G. F. Knoll. *Radiation Detection and Measurement.* Wiley, 4 edition, 8 2010.

[62] O. Tarasov, D. Bazin, M. Lewitowicz, and O. Sorlin. The code LISE: a new version for "windows". *Nuclear Physics A*, 701(1):661 – 665, 2002. 5th International Conference on Radioactive Nuclear Beams.

[63] E. Lunderberg, P. A. DeYoung, Z. Kohley, H. Attanayake, T. Baumann, D. Bazin, G. Christian, D. Divaratne, S. M. Grimes, A. Haagsma, J. E. Finck, N. Frank, B. Luther, S. Mosby, T. Nagi, G. F. Peaslee, A. Schiller, J. Snyder, A. Spyrou, M. J. Strongman,

and M. Thoennessen. Evidence for the ground-state resonance of ^{26}O. *Phys. Rev. Lett.*, 108:142503, Apr 2012.

[64] A. Spyrou, Z. Kohley, T. Baumann, D. Bazin, B. A. Brown, G. Christian, P. A. DeYoung, J. E. Finck, N. Frank, E. Lunderberg, S. Mosby, W. A. Peters, A. Schiller, J. K. Smith, J. Snyder, M. J. Strongman, M. Thoennessen, and A. Volya. First observation of ground state dineutron decay: ^{16}Be. *Phys. Rev. Lett.*, 108:102501, Mar 2012.

[65] T. Nakamura, A. M. Vinodkumar, T. Sugimoto, N. Aoi, H. Baba, D. Bazin, N. Fukuda, T. Gomi, H. Hasegawa, N. Imai, M. Ishihara, T. Kobayashi, Y. Kondo, T. Kubo, M. Miura, T. Motobayashi, H. Otsu, A. Saito, H. Sakurai, S. Shimoura, K. Watanabe, Y. X. Watanabe, T. Yakushiji, Y. Yanagisawa, and K. Yoneda. Observation of strong low-lying $e1$ strength in the two-neutron halo nucleus ^{11}Li. *Phys. Rev. Lett.*, 96:252502, Jun 2006.

[66] Z. Kohley, E. Lunderberg, P.A. DeYoung, B.T. Roeder, T. Baumann, G. Christian, S. Mosby, J.K. Smith, J. Snyder, A. Spyrou, and M. Thoennessen. Modeling interactions of intermediate-energy neutrons in a plastic scintillator array with Geant4. *Nuclear Instruments and Methods in Physics Research Section A: Accelerators, Spectrometers, Detectors and Associated Equipment*, 682:59 – 65, 2012.

[67] P. Speckmayer, A. Höcker, J. Stelzer, and H. Voss. The toolkit for multivariate data analysis, TMVA 4. *Journal of Physics: Conference Series*, 219(3):032057, April 2010.

[68] R. Brun and F. Rademakers. ROOT — an object oriented data analysis framework. *Nuclear Instruments and Methods in Physics Research Section A: Accelerators, Spectrometers, Detectors and Associated Equipment*, 389(1):81 – 86, 1997.

[69] N. Frank, A. Schiller, D. Bazin, W.A. Peters, and M. Thoennessen. Reconstruction of nuclear charged fragment trajectories from a large-gap sweeper magnet. *Nuclear Instruments and Methods in Physics Research Section A: Accelerators, Spectrometers, Detectors and Associated Equipment*, 580(3):1478 – 1484, 2007.

[70] Wave Metrics. IGOR PRO.

[71] A.S. Goldhaber. Statistical models of fragmentation processes. *Physics Letters B*, 53(4):306 – 308, 1974.

[72] K. Van Bibber, D. L. Hendrie, D. K. Scott, H. H. Weiman, L. S. Schroeder, J. V. Geaga, S. A. Cessin, R. Treuhaft, Y. J. Grossiord, J. O. Rasmussen, and C. Y. Wong. Evidence for orbital dispersion in the fragmentation of ^{16}O at 90 and 120 mev/nucleon. *Phys. Rev. Lett.*, 43:840–844, Sep 1979.

[73] S. Agostinelli, J. Allison, K. Amako, J. Apostolakis, H. Araujo, P. Arce, M. Asai, D. Axen, S. Banerjee, G. Barrand, F. Behner, L. Bellagamba, J. Boudreau, L. Broglia,

A. Brunengo, H. Burkhardt, S. Chauvie, J. Chuma, R. Chytracek, G. Cooperman, G. Cosmo, P. Degtyarenko, A. Dell'Acqua, G. Depaola, D. Dietrich, R. Enami, A. Feliciello, C. Ferguson, H. Fesefeldt, G. Folger, F. Foppiano, A. Forti, S. Garelli, S. Giani, R. Giannitrapani, D. Gibin, J.J. Gómez Cadenas, I. González, G. Gracia Abril, G. Greeniaus, W. Greiner, V. Grichine, A. Grossheim, S. Guatelli, P. Gumplinger, R. Hamatsu, K. Hashimoto, H. Hasui, A. Heikkinen, A. Howard, V. Ivanchenko, A. Johnson, F.W. Jones, J. Kallenbach, N. Kanaya, M. Kawabata, Y. Kawabata, M. Kawaguti, S. Kelner, P. Kent, A. Kimura, T. Kodama, R. Kokoulin, M. Kossov, H. Kurashige, E. Lamanna, T. Lampén, V. Lara, V. Lefebure, F. Lei, M. Liendl, W. Lockman, F. Longo, S. Magni, M. Maire, E. Medernach, K. Minamimoto, P. Mora de Freitas, Y. Morita, K. Murakami, M. Nagamatu, R. Nartallo, P. Nieminen, T. Nishimura, K. Ohtsubo, M. Okamura, S. O'Neale, Y. Oohata, K. Paech, J. Perl, A. Pfeiffer, M.G. Pia, F. Ranjard, A. Rybin, S. Sadilov, E. Di Salvo, G. Santin, T. Sasaki, N. Savvas, Y. Sawada, S. Scherer, S. Sei, V. Sirotenko, D. Smith, N. Starkov, H. Stoecker, J. Sulkimo, M. Takahata, S. Tanaka, E. Tcherniaev, E. Safai Tehrani, M. Tropeano, P. Truscott, H. Uno, L. Urban, P. Urban, M. Verderi, A. Walkden, W. Wander, H. Weber, J.P. Wellisch, T. Wenaus, D.C. Williams, D. Wright, T. Yamada, H. Yoshida, and D. Zschiesche. Geant4—a simulation toolkit. *Nuclear Instruments and Methods in Physics Research Section A: Accelerators, Spectrometers, Detectors and Associated Equipment*, 506(3):250 – 303, 2003.

[74] J. Allison, K. Amako, J. Apostolakis, H. Araujo, P. Arce Dubois, M. Asai, G. Barrand, R. Capra, S. Chauvie, R. Chytracek, G. A. P. Cirrone, G. Cooperman, G. Cosmo, G. Cuttone, G. G. Daquino, M. Donszelmann, M. Dressel, G. Folger, F. Foppiano, J. Generowicz, V. Grichine, S. Guatelli, P. Gumplinger, A. Heikkinen, I. Hrivnacova, A. Howard, S. Incerti, V. Ivanchenko, T. Johnson, F. Jones, T. Koi, R. Kokoulin, M. Kossov, H. Kurashige, V. Lara, S. Larsson, F. Lei, O. Link, F. Longo, M. Maire, A. Mantero, B. Mascialino, I. McLaren, P. Mendez Lorenzo, K. Minamimoto, K. Murakami, P. Nieminen, L. Pandola, S. Parlati, L. Peralta, J. Perl, A. Pfeiffer, M. G. Pia, A. Ribon, P. Rodrigues, G. Russo, S. Sadilov, G. Santin, T. Sasaki, D. Smith, N. Starkov, S. Tanaka, E. Tcherniaev, B. Tome, A. Trindade, P. Truscott, L. Urban, M. Verderi, A. Walkden, J. P. Wellisch, D. C. Williams, D. Wright, and H. Yoshida. Geant4 developments and applications. *IEEE Transactions on Nuclear Science*, 53(1):270–278, Feb 2006.

[75] B. Roeder. Development and validation of neutron detection simulations for EURISOL. *EURISOL Design Study, Report:[10-25-2008-006-In-beamvalidations. pdf, pp 31-44]*, 2008.

[76] J. B. Birks. Scintillations from Organic Crystals: Specific Fluorescence and Relative Response to Different Radiations. *Proc. Phys. Soc.*, A64:874–877, 1951.

[77] M. Wang, G. Audi, A. H. Wapstra, F. G. Kondev, M. MacCormick, X. Xu, and B. Pfeiffer. The AME2012 atomic mass evaluation (II). tables, graphs and references. *Chin.Phys.C*, 36:1603, 2012.

[78] Yu. Aksyutina, H.T. Johansson, T. Aumann, K. Boretzky, M.J.G. Borge, A. Chatillon, L.V. Chulkov, D. Cortina-Gil, U. Datta Pramanik, H. Emling, C. Forssén, H.O.U. Fynbo, H. Geissel, G. Ickert, B. Jonson, R. Kulessa, C. Langer, M. Lantz, T. LeBleis, A.O. Lindahl, K. Mahata, M. Meister, G. Münzenberg, T. Nilsson, G. Nyman, R. Palit, S. Paschalis, W. Prokopowicz, R. Reifarth, A. Richter, K. Riisager, G. Schrieder, H. Simon, K. Sümmerer, O. Tengblad, H. Weick, and M.V. Zhukov. Properties of the ^{7}He ground state from ^{8}He neutron knockout. *Physics Letters B*, 679(3):191 – 196, 2009.